Modelling the Spectral Energy Distribution and Polarisation of Blazars

HM Schutte

orcid.org 0000-0002-1769-5617

Dissertation submitted in partial fulfilment of the requirements for the degree *Master of Science in Astrophysical Science* at the North-West University

Supervisor: Prof M Boettcher

Graduation May 2019

22799133

Abstract

The optical emission from most blazars is dominated by the polarised synchrotron radiation of relativistic electrons in the jet. However, the thermal radiation from the accretion disc and host galaxy also contributes towards the high and low frequency ends of the optical spectrum. As the accretion disc and host galaxy emissions are expected to be unpolarised, they may manifest as a decrease of the degree of polarisation towards the high- and low frequency ends of the optical spectrum, respectively. This motivates a target of opportunity (ToO) programme for spectropolarimetry observations of gamma-ray blazars with the Southern African Large Telescope (SALT). A model is constructed that combines modelling of the spectral energy distribution (SED) and of the degree of optical polarisation to constrain the accretion disc contributions in the spectra of blazars.

This dissertation presents a simultaneous SED and polarisation model fit to the Flat Spectrum Radio Quasar (FSRQ) 4C+01.02 in its flare and quiescent states. With this model, the electron distribution energies γ_1, γ_b and γ_c, electron spectral indices, ordering of the magnetic field of the jet, accretion disc luminosity and the mass of the black hole $\sim 4.0 \times 10^8$ $M_\odot$, are constrained.

Keywords: active galaxies - blazars, polarisation - optical, spectropolarimetry

Contents

Acronyms and Abbreviations

AGN Active Galactic Nuclei

BH Black Hole

BLR Broad Line Region

EC External Compton

EBL Abs. Extragalactic Background Light Absorption

ECD External Compton (Disc)

EIC External Inverse Compton (BLR)

EM electromagnetic

Fermi-LAT Fermi Large Area Telescope

FSRQ Flat Spectrum Radio Quasars

GPE Gravitational Potential Energy

HBL High-frequency peaked BL Lac objects

LAT Large Area Telescope

LBL Low-frequency peaked BL Lac objects

LCO Las Cumbres Observatory

LOS Line of Sight

NLR Narrow Line Region

RSS Robert Stobie Spectrograph

SAAO South African Astronomical Observatory

SALT Southern African Large Telescope

SED Spectral Energy Distribution

SMBH Super Massive Black Holes

SS Shakura Sunyaev

SSC Synchrotron Self-Compton

Swift Neil Gehrels Swift Observatory

ToO Target of Opportunity

UFS University of the Freestate

UV Ultraviolet

Chapter 1

Introduction

1.1 Active Galactic Nuclei

This chapter describes the characteristics of Active Galactic Nuclei (AGN). AGN are observed to have very high luminosities, broad non-thermal emission, strong and broad emission lines or weak and sometimes absent emission lines, relativistic jets and display variability over various time scales over all wavelengths. AGN will be described by the processes that happen in the vicinity of their Super Massive Black Holes (SMBH), their accretion discs and their relativistic jets. The different types of AGN will briefly be distinguished between, where-after a discussion follows on the different types of blazars, namely: BL Lac objects and Flat Spectrum Radio Quasars (FSRQ). Section 2 of this introduction chapter gives the theory of synchrotron radiation, accretion disc radiation and polarisation. In section 3 the subject of this dissertation is introduced with related work that has previously been done, where-after a problem statement and research goal follows. An outline of the rest of this dissertation is given at the end of this chapter.

1.1.1 What are Active Galactic Nuclei?

The main components of an AGN (Figure 1.1) are: the accretion disc, the SMBH, jets flowing out from the middle of the disc, the Narrow Line Region (NLR), the Broad Line Region (BLR), a dust torus and there may be a corona. The corona is a hot and diluted gas around a thin accretion disc (Netzer, 2013). It is uncertain what the exact geometry of the accretion disc is, but it might be a thick or a thin disc, as illustrated in Figure 1.2.

AGN have the following features that distinguish them from other astronomical sources:

1. **High Luminosity**
   Active galaxies, that is galaxies hosting an AGN, are more luminous than normal galaxies (galaxies such as the Milky Way). AGN have luminosities ranging from $\sim 10^{42}$ erg/s to $\sim 10^{48}$ erg/s (Hartle, 2003). AGN can therefore be up to 10 000 times brighter than all the stars within a typical galaxy that has a luminosity of $\sim 10^{44}$ erg/s. There is no precise lower luminosity limit because even the Black Hole (BH) of our Galaxy shows some characteristics of being an active galaxy. Therefore, there is not a clear distinction between active and normal galaxies.

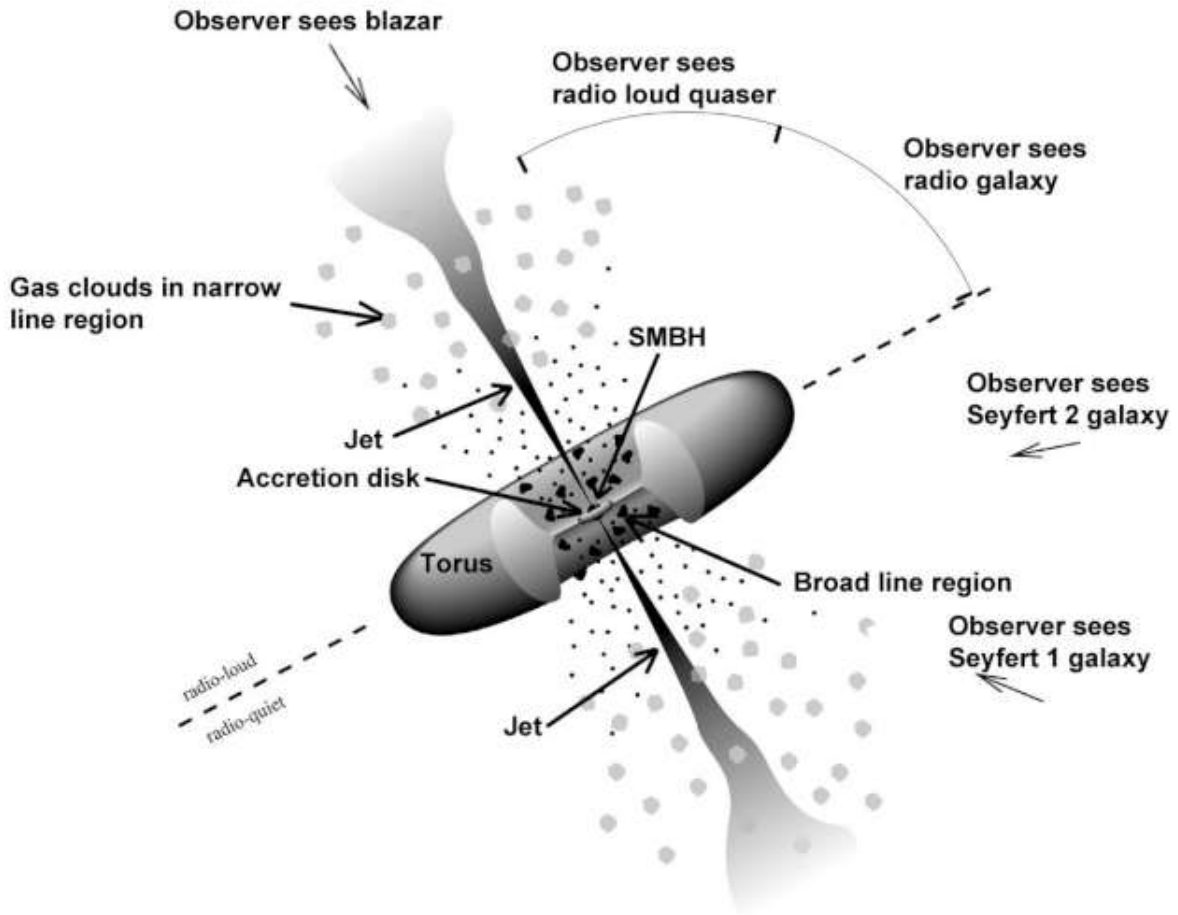

Figure 1.1: A schematic drawing of an AGN. The central SMBH is surrounded by an accretion disc, which is in turn surrounded by a dust torus. Broad emission lines originate in the cold gas clouds of interstellar material orbiting the disc. Narrow lines originate in the clouds that are much farther away from the SMBH. Jets of relativistic particles can extend to distances greater than the diameter of the host galaxy. The different categories of AGN depend on the observation location. This figure was taken from Urry and Padovani (1995).

2. **Broad Non-thermal Emission**
   For normal galaxies the spectrum of radiation is the total spectra of all the stars, dust clouds and Hydrogen gas. Stars have an approximate black body spectrum (Hartle, 2003) with absorption lines. AGN have spectra that include the radio, infrared-submillimeter, optical (where the host galaxy can be approximated as a black body spectrum), Ultraviolet (UV), X-ray and gamma-ray bands. This is illustrated in a Spectral Energy Distribution (SED), see Figure 1.3. This figure shows the Leptonic and Lepto-Hadronic models of the SED, that will be further described in section 1.2.3.

3. **Strong and Broad Emission Lines**
   AGN can have strong, weak and sometimes absent emission lines. Figure 1.4 illustrates the emission lines of an AGN.

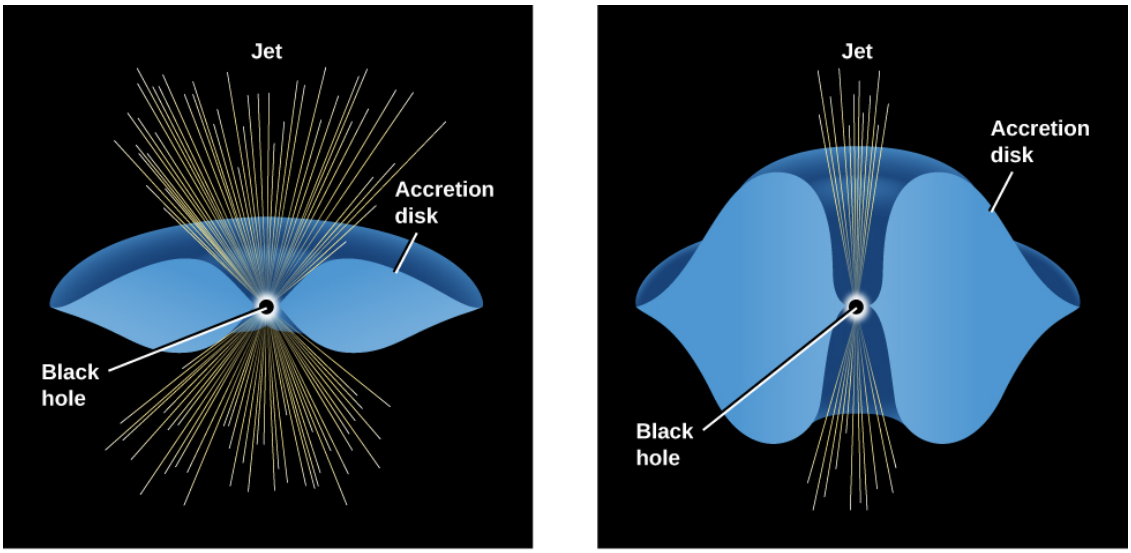

Figure 1.2: A simple schematic to describe an active galaxy (the accretion disc is cut in half to reveal the SMBH). (a) illustrates a thin accretion disc and (b) illustrates a thick accretion disc (*Supermassive Black Holes: What Quasars really are*, n.d.). These discs create funnels wherein radiation pressure or Poynting flux is released so that the gas moves as narrow relativistic jets away from and perpendicular to the accretion disc. This figure was taken from *Supermassive Black Holes: What Quasars really are* (n.d.).

Narrow emission lines and absorption lines can also be observed (see Figure 1.5). When the accretion disc drives outflows, the matter coming towards us will be blue-shifted and absorption lines exhibit blue-shifted features (Netzer, 2013).

4. **Radio Jets**
   All radio galaxies have two lobes or jets that are perpendicular to the accretion disc (Böttcher et al., 2012). In radio galaxies, jets are observed to extend to far greater distances than the size of the galaxy itself (Hartle, 2003).

5. **Variability**
   The luminosity of normal galaxies does not fluctuate much compared to the luminosity of active galaxies which are variable, changing by a factor of 2 or more.

   The variability is illustrated by Figures 1.6 and 1.7, and may be due to the time dependence of matter that falls in towards the SMBH. Variability proceeds over different periods for each frequency band and sometimes correlations occur between them. The emission lines of AGN are also variable.

It is possible that every galaxy has a BH at its centre. This means that normal galaxies will become active galaxies when their BHs have enough matter surrounding them. Our Milky Way, for example, has a dormant BH Sagittarius A*, but it is possible that our galaxy was an AGN once (Brandt and Alexander, 2015; Franceschini et al., 1999; Marconi et al., 2004). There have been observations of galaxies without a BH at their centre (Burke-Spolaor et al., 2017).

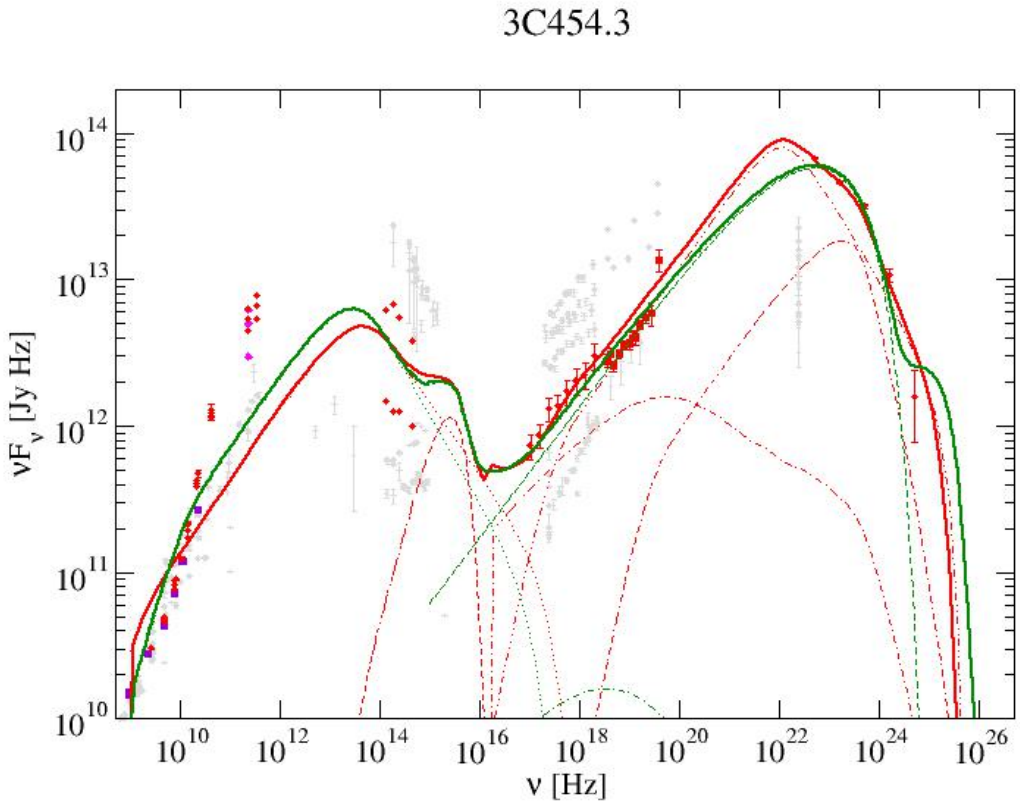

Figure 1.3: The broad band spectrum of 3C454.3. A description of the model components follows in section 1.2.3. The Leptonic model (red) with its components; dotted: synchrotron, dashed: accretion disc, dot-dashed: SSC, dot-dash-dashed: EC (disc) and dot-dot-dash: EC (BLR). The Hadronic model (green) with its components; dotted: electron-synchrotron, dashed: accretion disc, dot-dashed: SSC and dot-dot-dashed: proton-synchrotron. This figure was taken from Böttcher et al. (2013).

1.1.1.1 The Central Engine

The central engine refers to the "engine" in the core of the galaxy that streams out relativistic jets. AGN have a SMBH (with a mass range of $\sim 10^6 - 10^9$ $M_\odot$) in the centre of its host galaxy (Böttcher et al., 2012; Hartle, 2003). The size of the BH is characterized by the Schwarzschild radius. The Schwarzschild radius R_s is calculated by $R_s = 2M_{BH}G/c^2$, where M_{BH} is the mass of the BH, G is the gravitational constant and c is the speed of light. Around a non-rotating BH there is a sphere area with radius R_s, called the *event horizon*. The escape speed of a particle on the event horizon is the speed of light. Light emitted by matter passing through the event horizon will be increasingly redshifted towards infinity. Once photons or matter move past the event horizon, they cannot escape. The conditions within a BH are not yet well understood.

For a non-rotating BH, there is not a stable circular orbit close to the event horizon due to the spacetime curvature. The closest stable circular orbit is at a distance $R = 3R_s$

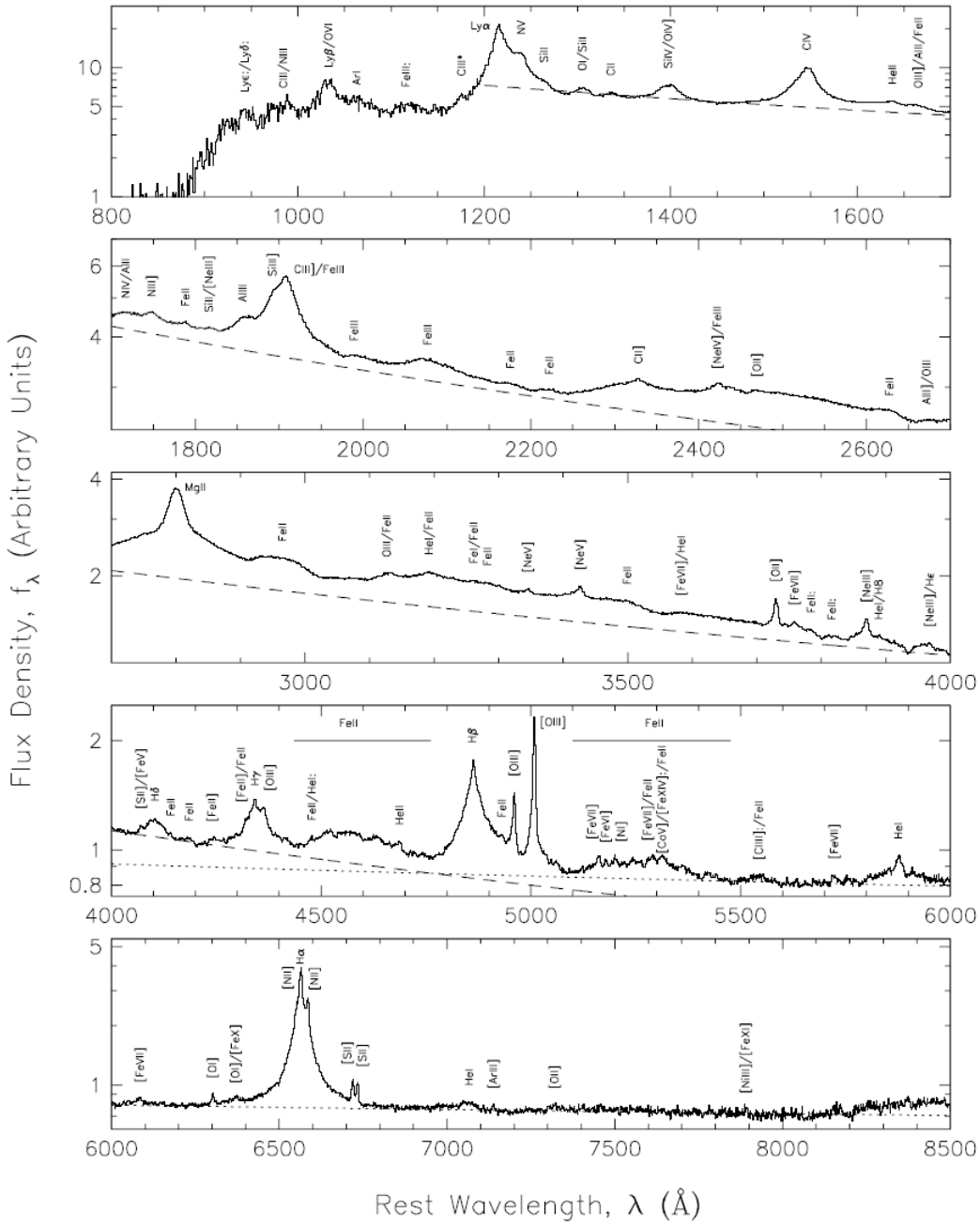

Figure 1.4: Plot of the emission lines of a composite quasar with the lines labelled by ion. Plot taken from Vanden Berk et al. (2001).

(Hartle, 2003). For a rotating BH the innermost stable orbit will increase when the BH rotates retrograde (in opposite direction) to the accretion disc and decrease if it rotates prograde (in the same direction) to the accretion disc.

1.1.1.2 The Accretion disc

Initially, the accreting matter does not fall straight into the BH, since it has angular momentum. This has the effect that the orbiting matter forms an accretion disc around the

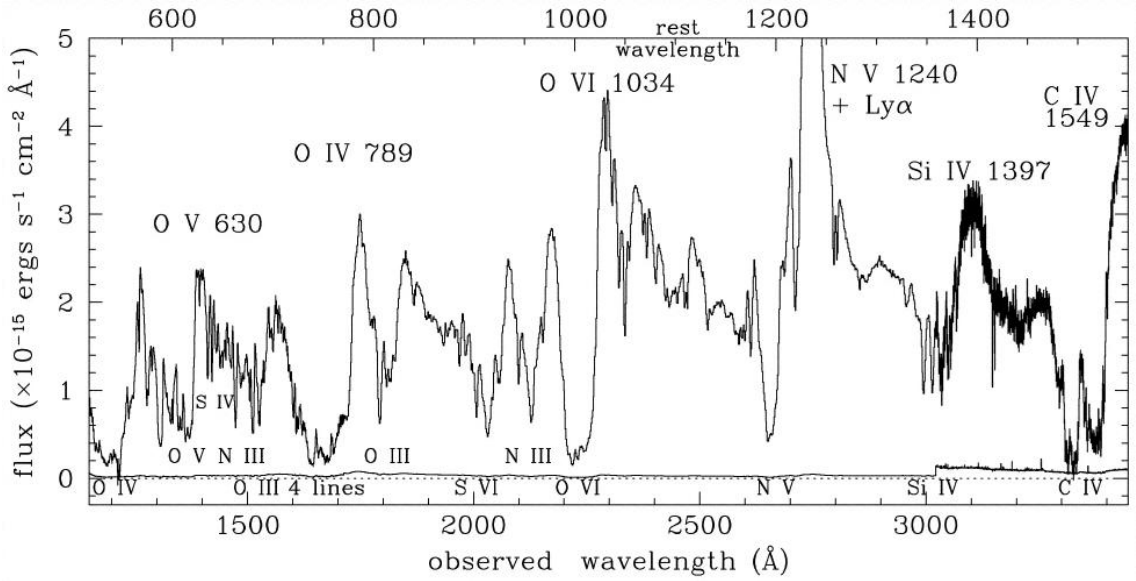

Figure 1.5: Space Telescope Imaging Spectrograph (STIS) observations of PG 0946+301. The plot shows the flux in the observed frame. The bottom labels indicate the ions at their corrosponding absorption lines, while the broad emission lines are indicated with the top ion labels. The solid line above the dotted zero-flux line, is the noise spectrum. This plot and its explanation was taken from Arav et al. (2001).

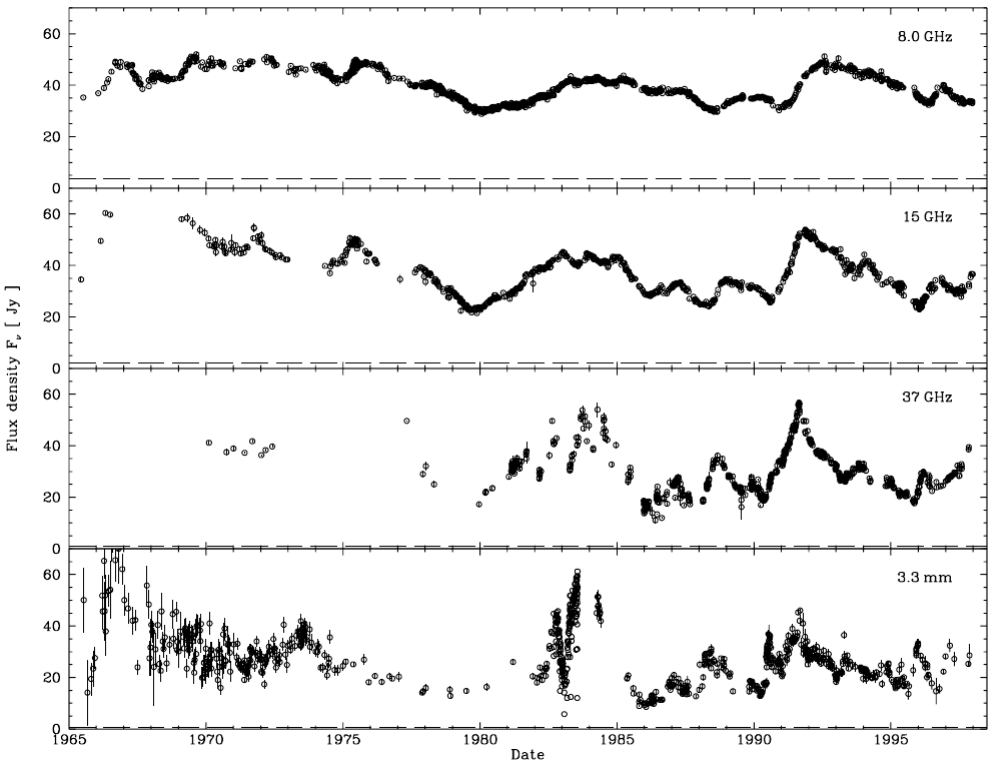

Figure 1.6: Light curves showing the variability of 3C273 in the radio to millimetre bands. This plot was taken from Türler et al. (1999).

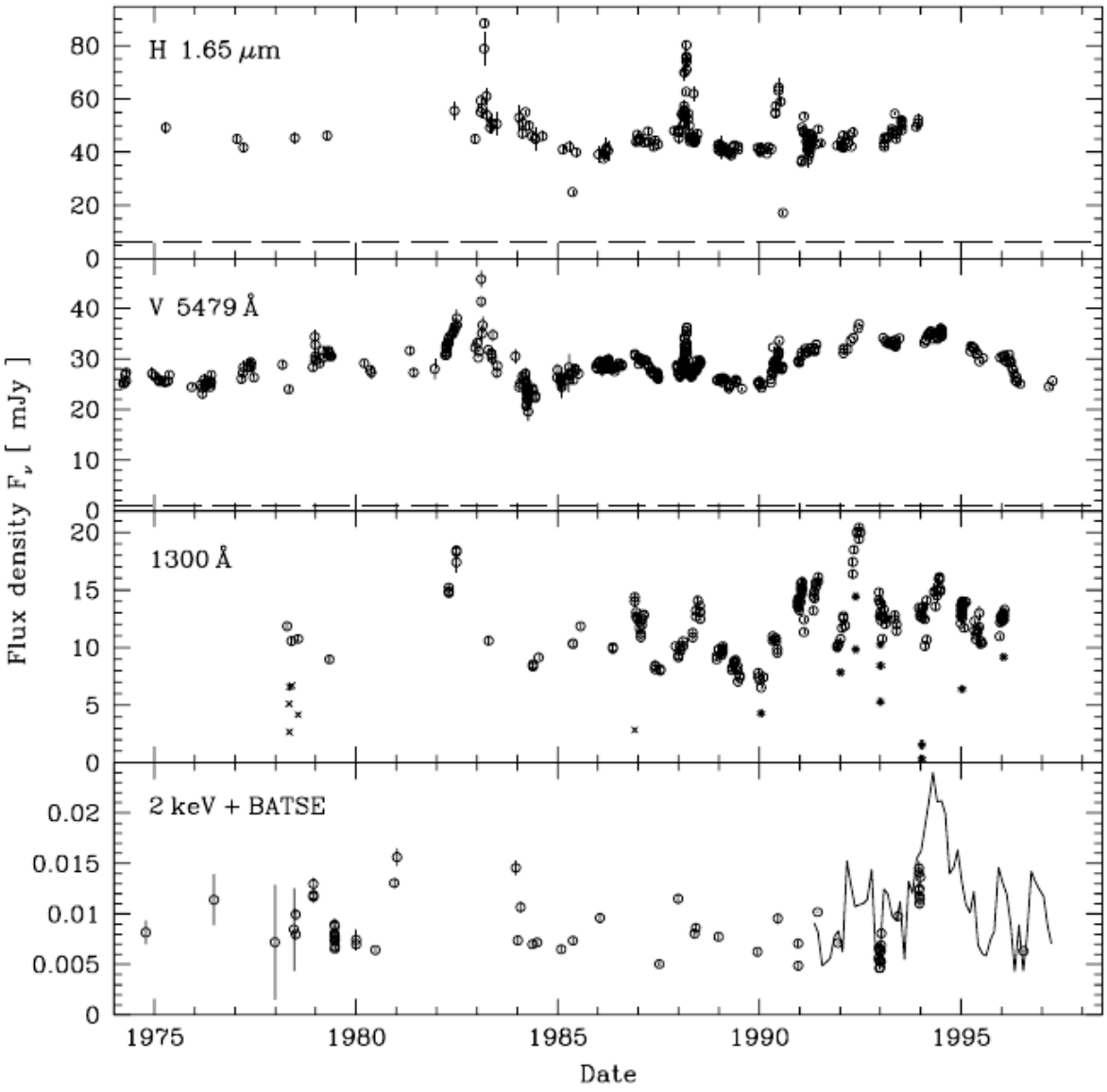

Figure 1.7: Light curves showing the variability of 3C273 in the infrared to X-ray bands. This plot was taken from Türler et al. (1999).

BH (Hartle, 2003). As the BH attracts matter towards it, the matter in orbits closer to it will move faster than that further away from it. This inner, faster moving gas interacts with the matter that is further away from the BH. The friction then heats-up the gas to extreme temperatures. Interactions between the particles and the disc cause the matter to lose energy and angular momentum, so that they orbit (in nearly circular orbits) closer and closer to the BH, until they reach the innermost stable orbit where they will fall straight into the BH. As the material in the accretion disc spirals onto the BH, the Gravitational Potential Energy (GPE) they lose is emitted as UV, optical and infra-red radiation.

The magnetic fields can form from the ionized plasma and currents in the disc or be frozen into the BH. The rotating accretion disc gives rise to a helical magnetic field. This is because the magnetic fields are twisted by the rotating disc.

Furthermore, the gravity of the BH keeps on pulling matter to spiral towards it, giving a further increasing temperature and thereby causing the matter here to be at extreme pressures. This extreme pressure of gas, cannot be released in the direction of the converging accretion disc, so that some of the pressure is released perpendicular to the accretion disc, into the corona. The outflow of energy and momentum from the BH sometimes results in relativistic jets that are seen in some types of AGN (Böttcher et al., 2012).

1.1.1.3 Broad and Narrow Line Region

Clouds of cold interstellar matter orbit the SMBH above the accretion disc in the BLR and the NLR (Böttcher et al., 2012). The BLR is closer to the BH and the lower density clouds in the NLR are further out (Figure 1.1). Broad and narrow emission lines are emitted due to the gas undergoing photo-excitation and photo-ionisation. The emission lines from these regions have different widths, because the regions have different electron densities.

When blazars are observed, the core emission can outshine the host galaxy and the BLR (Beckmann and Shrader, 2012). In these circumstances it becomes impossible to estimate the mass of the BH by using the width of the lines that come from the host galaxy. Another way in which observations of the disc and BLR can be obscured, is when the optically thick torus (Figure 1.1) is viewed edge-on. In these circumstances, the NLR can still be seen, for instance, light can escape from beyond obscuring material when photons collide with electrons so that they are scattered and can move along our Line of Sight (LOS). This scattered light is linearly polarised. There are, however, AGN that do not show polarised light from the BLR when the accretion rate is not high enough. There is also the possibility that the central engine is not powerful enough to illuminate the BLR which could explain why BL Lacs do not show emission lines.

1.1.1.4 Relativistic Jets

Jets are formed in the vicinity of the BH, where a dense gas of particles is released perpendicular to the accretion disc, accelerated and spiralled along the helical magnetic fields, to emit synchrotron radiation (Böttcher et al., 2012). The particles can sometimes be accelerated to relativistic speeds by shocks or magnetic reconnection in the jet. When these particles move at relativistic speeds and with the proper orientation, they can appear to move at

superluminal speeds. Superluminal motion is when the relativistic knots (see Figure 1.8) of radio loud AGN appear to move faster than the speed of light (Beckmann and Shrader, 2012; Böttcher et al., 2012). However, it is only the apparent velocity we observe that appears to be greater than the speed of light, because the time is shortened by light-travel-time effects.

Jets transport energy, momentum and angular momentum over distances that range

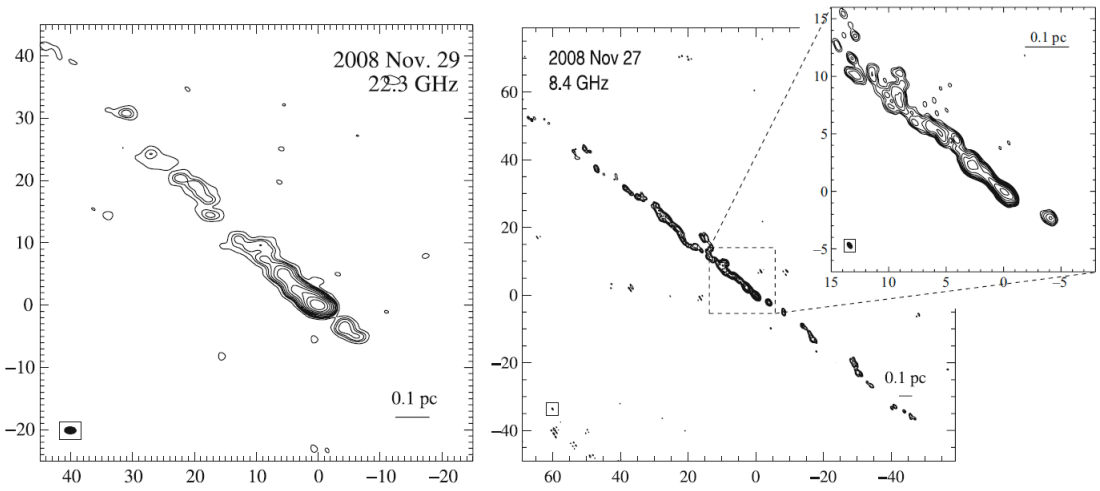

Figure 1.8: The inner jet of Centaurus A is shown to have knot structures resolved into separate components. These VLBI images were taken from Mueller et al. (2011).

from the radius $R_S = 10^{-4} M_{BH}/(10^9\ \mathrm{M}_\odot)$ pc to radio hot spots, hot spot complexes and lobes that can be a megaparsec or more away (Figure 1.9) (Böttcher et al., 2012). Hot spots are very bright regions within radio lobes. The jets stream out until they reach these regions where there is gas to interact with. Superluminal knots are formed by shock waves that propagate along the jet (Marscher, 2006).

It is not certain how jets form and accelerate and what collimates them to remote locations (Böttcher et al., 2012; Gómez et al., 2016). It is possible that the jet is being powered by, not only the BH, but also the accretion disc. The connection between the central engine and the relativistic jet is still not firmly established. There should be a connection between the magnetic state of the jet and the accretion state of the inner disc (Marscher, 2006).

1.1.2 Different Types of AGN

AGN have been sorted into various classes since their discovery. A few observational attributes that can be used to classify them include: the SED that can tell us about the possible power mechanisms in different energy bands, the emission line properties, the host galaxy, how active the source is and the accretion rate (Netzer, 2013). The BH spin, accretion rate, host galaxy properties and the gas content and metallicity in the nuclear region can also classify different types of AGN. Lastly, different types of AGN can be distinguished between by their intensity, radio loudness, evidence for obscuration and variability. Table 1.1 shows how different types of AGN can be classified according to their properties.

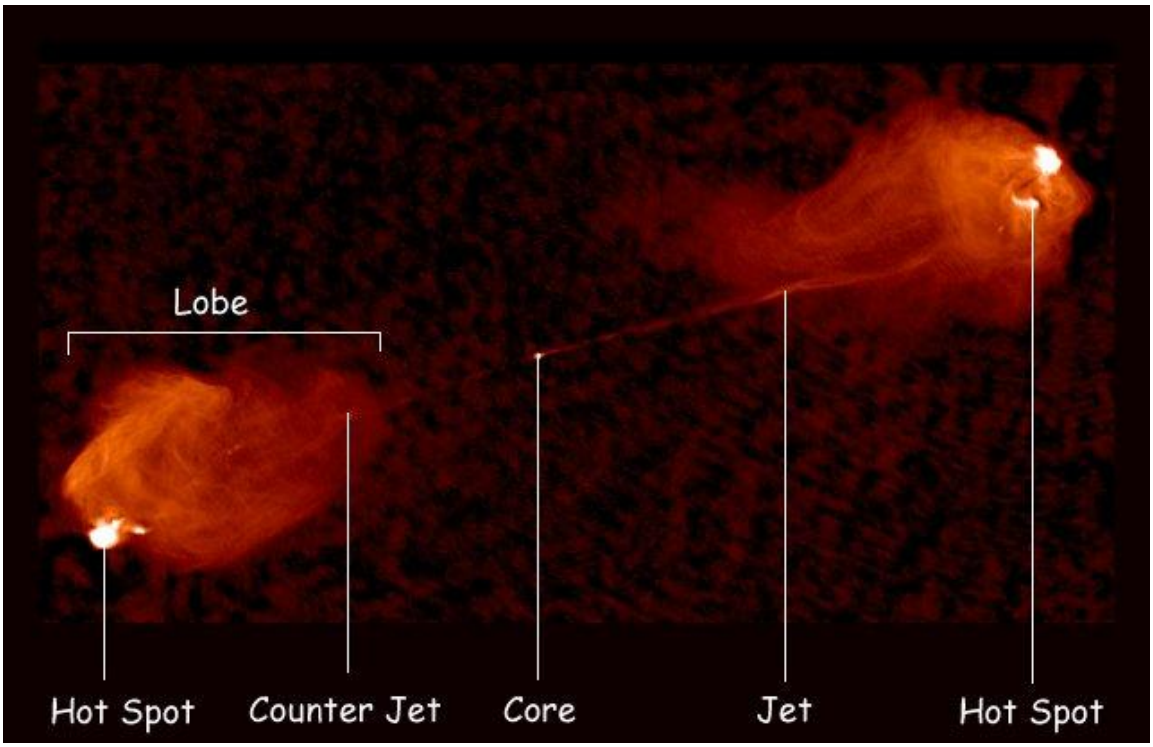

Figure 1.9: Cygnus A is an AGN at redshift $z = 0.06$ (Carilli and Barthel, 1996). The jet moves through the intergalactic medium which slows down matter (Böttcher et al., 2012). But the jets move at greater speeds than the interstellar medium so that shocks are formed at the ends of the jets. Within these shocks there are high luminosity regions called *hot spots*. The hot spot and the wake of the jet is referred to as the *radio lobe*. The radio lobes can change form due to the intergalactic medium slowing matter down, the movement of its active galaxy or due to changes within the jet. This figure is taken from NRAO/AUI.

AGN can be divided into groups according to the angle at which they are observed from (Figure 1.1). If the AGN is observed from the side with both radio lobes and jets visible, it can be identified as a radio galaxy. The radio galaxy Cygnus A is shown in Figure 1.9. In this figure narrow jets extending from the SMBH are visible. With decreasing angle between the jet and the LOS, the AGN is observed as a narrow line radio galaxy, broad line radio galaxy and a radio loud quasar. The local universe has $\sim 10\%$ radio loud (QSRs) and $\sim 90\%$ radio quiet quasars (QSOs) (Beckmann and Shrader, 2012). When the jet is closely aligned to the LOS, the AGN is a blazar. Blazars are divided into two types, namely quasars and BL Lacs. These are further described in the next subsection.

Seyfert Galaxies are radio quiet AGN with weak jet emission. There are two types of Seyfert Galaxies (Figure 1.1): Seyfert 1 and Seyfert 2 galaxies are differentiated from each other by their optical-UV spectra (Netzer, 2013). Seyfert 1 galaxies have strong and broad emission lines of $(2 \times 10^8$ to $10^9)$ cm $\cdot$ s^{-1} due to Doppler broadening, while Seyfert 2 galaxies have emission lines with a maximum width of $\sim 1.2 \times 10^8$ cm $\cdot$ s^{-1}. These differences are

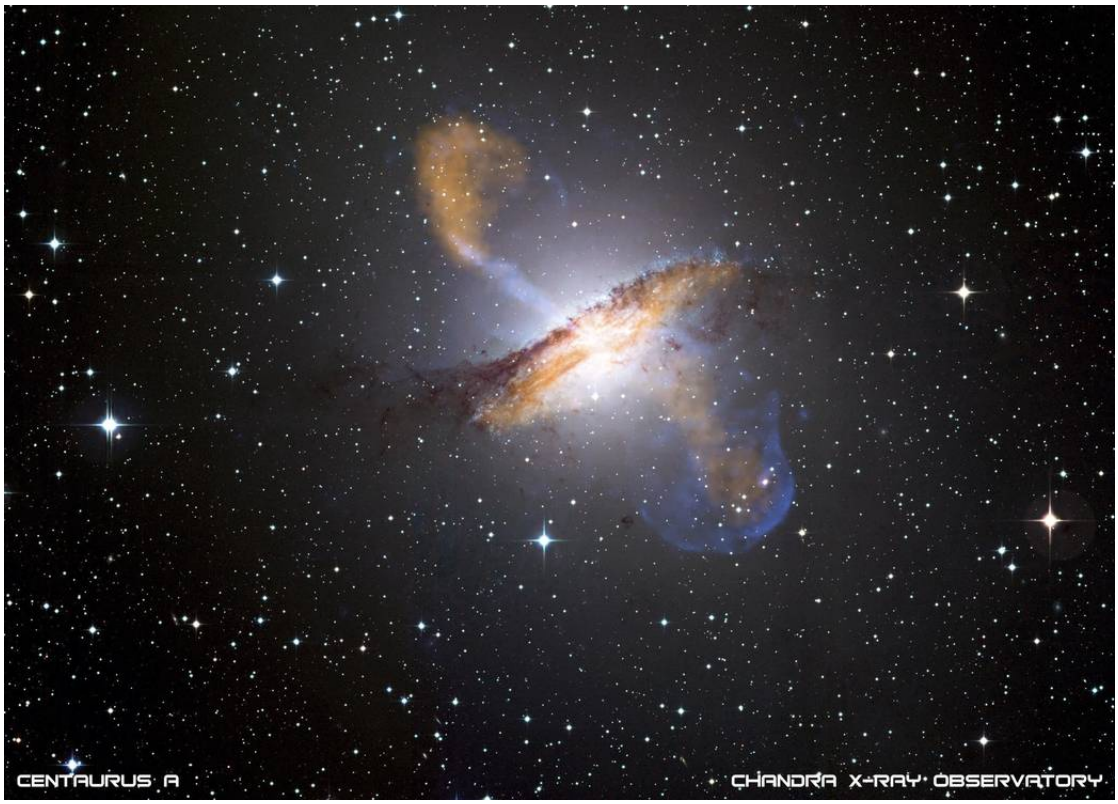

Figure 1.10: An overlay of different images across the EM (electromagnetic) spectrum illustrating the AGN Centaurus A. "Submillimeter data (coloured orange) are from the Atacama Pathfinder Experiment (APEX) telescope in Chile and X-ray data (coloured blue) are from the Chandra X-ray Observatory. Visible light data from the Wide Field Imager on the Max-Planck/ESO 2.2 m telescope, also located in Chile, shows the dust lane in the galaxy" (*A Black Hole Overflows From Galaxy Centaurus A*, 2009). Foreground stars are also shown. "The X-ray jet in the upper left extends for about 13 000 light years away from the BH. The APEX data shows that material in the jet is traveling at about half the speed of light. Image credit: X-ray: NASA/CXC/CfA/R.Kraft et al.; Submillimeter: MPIfR/ESO/APEX/A.Weiss et al.; Optical: ESO/WFI" (*A Black Hole Overflows From Galaxy Centaurus A*, 2009).

accounted for by different viewing angles that have different obscuration along the line of sight.

1.1.3 Blazars

Blazars are a subclass of radio loud AGN that are jet dominated. They are the most violent of the AGN types, have rapid variability, a high polarisation (in optical and radio frequencies), radio core-dominance and apparent superluminal speeds (Liu, 2009). Some objects show a lack of strong optical emission lines. The jet material has a relativistic velocity $v_{jet} = \beta c$ with $\beta \approx 1$. Blazars emit nonthermal-dominated radiation in the radio to gamma-ray spectrum.

	Quasars	**BL Lac Objects**	**Seyfert Galaxies**	**Radio Galaxies**
Galaxy type	Spiral and elliptical	Elliptical	Spiral	Giant elliptical
Appearance	Compact, Blue	Bright, Starlike	Compact Bright Nucleus	Elliptical
Maximum luminosity	$100 - 1000\times$ Milky Way	$10000\times$ Milky Way	Comparable to bright spirals	Strong Radio
Emission spectrum	Broad and Narrow	Very weak	Broad and Narrow	Rare, broad and narrow
Absorption lines	Yes	None	Yes (Crenshaw et al., 1999)	Yes
Variability	Days to weeks	Hours	Days to weeks	Days
Emits radio	Yes	Yes	Weak	Yes
Redshifts	$z > 0.5$	$z \sim 0.1$	$z \sim 0.05$	$z < 0.05$
Jets	Some	Possible	Some	Often

Table 1.1: Summary of the different types of AGN. This table was adapted from *Cosmology - Galaxies* (2004-2013).

The Different Types of Blazars: BL Lac Objects and Flat Spectrum Radio Quasars

BL Lac objects are the beamed counterparts of low-luminosity radio galaxies, whereas FSRQs are the beamed counterparts of high luminosity radio galaxies (Liu, 2009). FSRQs show higher radio polarisation than BL Lacs (Beckmann and Shrader, 2012). The leading difference between these can be seen in their emission lines: FSRQs have broad and strong emission lines whereas BL Lac objects have weak or in some instances absent emission lines.

In Figure 1.3, the sum of the components towards low frequencies is referred to as the low-frequency component and the sum of the components within X-ray through gamma-ray regimes is referred to as the high-frequency component. Fossati et al. (1998) divided blazars into three categories: FSRQs, Low-frequency peaked BL Lac objects (LBL) and High-frequency peaked BL Lac objects (HBL), thereby dividing the BL Lac objects into two sub-types. Blazars are divided according to the frequency at which the synchrotron component peaks (Böttcher, 2010). If the source exhibits a low-synchrotron peak (i.e. the peak is in the infrared region where $\nu \leq 10^{14}$ Hz), then the AGN is identified as a FSRQ or a LBL. If the source exhibits an intermediate-synchrotron-peak at $10^{14} < \nu \leq 10^{15}$ Hz, then the AGN can be identified as a LBL or intermediate BL Lac object. A high-synchrotron peak at 10^{15} Hz $< \nu$, can identify the AGN as a HBL.

1.2 Radiation and Polarisation Processes in Blazars

This section will describe the theory behind the different components that contribute to the SED and polarisation within the optical/UV regime. A short description is given on how the high-energy radiation components can be modelled. An illustration of the SED of a blazar was given in Figure 1.3. It shows that there are two main SED components: the first component is the sum of the synchrotron radiation from the relativistic electrons in the jet (non-thermal radio through to UV emission or X-ray emission) and the accretion disc (thermal optical through UV); and the second component (in X-ray through gamma-ray) can be modelled with Leptonic or Hadronic models (Böttcher et al., 2013). These models yield Compton scattering components in the high-energy (X-ray through gamma-ray) regime. In this regime, the Hadronic model also includes proton-synchrotron and pair-synchrotron components.

1.2.1 Introduction to Radiation

1.2.1.1 Non-Thermal Radiation

A distribution of electrons emits synchrotron radiation in the low-frequency component and leads to Compton scattering in the high-frequency components. For FSRQs, synchrotron radiation is emitted in the radio through UV energy band.

The electron distribution in the emission region can often be described by a broken power law with an exponential cut-off, which is given as

$$N_e(\gamma) = n_0 \begin{cases} (\frac{\gamma}{\gamma_b})^{-p_1} e^{-\gamma_b/\gamma_c} & \text{for } \gamma_{min} \leq \gamma \leq \gamma_b \\ (\frac{\gamma}{\gamma_b})^{-p_2} e^{-\gamma/\gamma_c} & \text{for } \gamma_b \leq \gamma_{max}, \end{cases} \tag{1.1}$$

where $N(\gamma)$ is the number of electrons per unit volume in the interval $[\gamma, \gamma + d\gamma]$, with γ the Lorentz-factor (energies), γ_b is the break energy and γ_c is the cut-off energy. When considering only synchrotron radiation, only the total number of electrons n_0 is constrained. The factor n_0, also serves as a normalisation factor. The density can be determined when Synchrotron Self-Compton (SSC) radiation is also taken into account. The electron distribution spectral index is p_1 for the first part of the power law (in the range $\gamma_{min} \leq \gamma \leq \gamma_b$), and p_2 for the second part of the power law (in the range $\gamma_b \leq \gamma_{max}$). The spectral index p values typically range from 2 to 3, but they can also be smaller or larger. The synchrotron spectrum and Compton spectrum have a spectral index that can be written in terms of p as

$$\alpha = \frac{p-1}{2}. \tag{1.2}$$

The frequencies where gradients change in the synchrotron spectrum correlate with the Lorentz factor energies where gradients change in the electron distribution. These characteristic frequencies are the minimum frequency $\nu_{min} = \nu_0 \gamma_{min}^2$, the break frequency $\nu_b = \nu_0 \gamma_b^2$ and the cool-off frequency $\nu_c = \nu_0 \gamma_c^2$. Here, $\nu_0 = 4.2 \times 10^6 \cdot B$ Hz, with B the magnetic field in units of Gauss [G].

The low-frequency radiation component is dominated by nonthermal synchrotron radiation and the thermal contributions are often from the accretion disc, host galaxy and dust

torus. The host galaxy and dust torus will not be discussed, as it is not important in the model which is focussed on fitting optical/UV spectropolarimetry to constrain the accretion disc component and thereby the BH mass.

1.2.1.2 Redshift and Doppler Shift

For distant objects there is a cosmological redshift due to the expansion of the universe where the space between Earth and the object is expanding. This implies that the light emitted from a source will have a wavelength that is stretched out so that we receive lower frequencies than the frequencies that the source emitted at an earlier time in its rest frame. The redshift of radiation is given by

$$z = \frac{\nu_{em} - \nu_{obs}}{\nu_{obs}} \tag{1.3}$$

where the emission frequency in the rest frame ν_{em} is redshifted to an observed frequency ν_{obs}.

But the emission regions of blazars also move toward us so that we observe their Doppler shifted wavelengths. We observe their light with shorter wavelengths than what has been emitted in the object's rest frame. The observed frequency can then be calculated as (Böttcher et al., 2012),

$$\nu_{obs} = \delta \cdot \nu_{em} \tag{1.4}$$

where the Doppler factor $\delta = 1/\Gamma(1 - \beta\cos\theta)$, with Lorentz factor $\Gamma = 1/\sqrt{1-\beta^2}$.

Synchrotron emission is Doppler-shifted and redshifted. The accretion disc and emission lines (in the BLR) are not Doppler-shifted since these are stationary, but they are redshifted.

1.2.2 Low-Frequency Radiation Components

1.2.2.1 Accretion disc and Corona Radiation

AGN can have geometrically thick or thin accretion discs that are optically thin or thick depending on their surface densities, to what level their gas is ionized and their mass accretion rates (Netzer, 2013). The accretion disc produces radiation in the optical-UV regime. The corona produces the radiation in the X-ray regime (Figure 1.11). The accretion disc is too cool to produce radiation at X-ray energies.

It is assumed that the viscosity within an accretion disc is necessary so that the angular momentum in the disc can move outwards while matter can move inwards losing some of their GPE, producing high luminosities (Netzer, 2013).

A number of models are suggested to describe the creation of the hot corona above the accretion disc. One of the possible models, assumes a hot optically thin corona above an optically thick accretion disc (Netzer, 2013; Witt et al., 1997). In this case, the energy dissipation and temperature rise of the accretion disc causes the outer layers of the disc to expand so that the corona is created. Here, the temperature depends on the accretion power of the disc. Another possible model considered for "real" (not optically thick, physically thin) discs, is that magnetic fields are threaded through the fast rotating accretion disc (Figure 1.12) and these magnetic fields can drive energy from the disc to the corona wherein

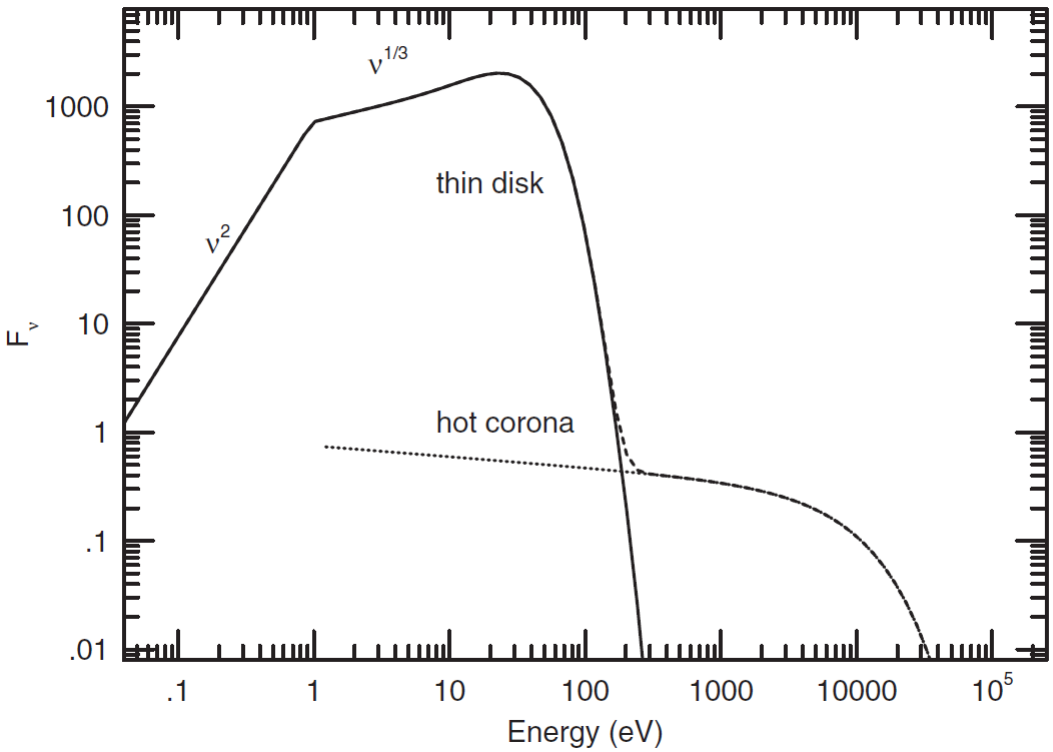

Figure 1.11: A schematic of the spectrum of the accretion disc with an optically thin corona. This figure is taken from Netzer (2013).

these particles Compton-upscatter accretion disc radiation so that the photons are boosted to X-ray energies.

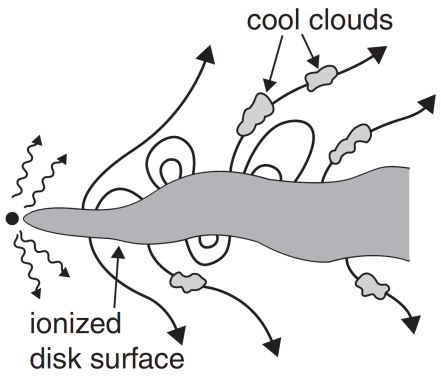

Figure 1.12: Schematic of magnetic field lines threaded through an accretion disc with a non-uniform geometry. Cool clouds are transfered along the magnetic fields. This figure is taken from Netzer (2013).

In this dissertation the accretion disc is modelled using the Shakura Sunyaev (SS) model. The Eddington luminosity is introduced in the next subsection. Thereafter, a description is given on what opacity and optical thickness is. The spectrum for a thin accretion disc is

described by using a SS accretion disc model (Shakura and Sunyaev, 1973).

1.2.2.1.1 The Eddington Limit

The Eddington luminosity is the maximum luminosity that a source can have when there is a balance between the inward gravitation forces and the outward radiation forces. The Eddington luminosity limit is defined as

$$L_{Edd} = \frac{4\pi c G M_{BH}}{\kappa}, \tag{1.5}$$

with the opacity κ (also called the absorption coefficient) the cross sectional area per unit mass [$\mathrm{cm}^2 \cdot \mathrm{g}^{-1}$]. Thomson scattering is the process in which photons are scattered by electrons without there being a change in the photon energy (Rybicki and Lightman, 1979). When considering high-energy accretion scenarios an approximation is made that the accreting matter is mostly ionized hydrogen, so that the opacity is due to Thomson scattering, since the electrons will be distributed very densely for a highly ionized gas. Although the cross section will mostly be dependent on the electrons that experience the radiation pressure, the mass will be that of the protons as the electrons are electro-statically coupled to the protons so that the protons will move with the electrons, implying that

$$\kappa = \frac{\sigma_T}{m_p} \tag{1.6}$$

where σ_T is the Thomson cross-section and m_p is the mass of the protons.

The optical depth (also called the optical thickness of a source) is defined as (Carroll and Ostlie, 2014),

$$\tau = \int_0^z \kappa \rho(r_\tau) dr_\tau, \tag{1.7}$$

where $\rho(r_\tau)$ (in units of $\mathrm{g} \cdot \mathrm{cm}^{-3}$) is the mass density of the particles that travelled over a distance r_τ. The optical depth can therefore tell us 'how transparent' the disc is.

For a limited accretion rate $\dot{M}$ at which mass can be accreted around a BH, the disc luminosity L_d can be parametrised as (Carroll and Ostlie, 2014),

$$L_d = \epsilon \dot{M} c^2. \tag{1.8}$$

where ϵ is the efficiency of converting potential energy into radiation and it is defined as a fraction of the rest-mass energy and depends on the BH spin. For a non-rotating BH ϵ is constant. If ϵ is zero, matter will fall in radially over the event horizon into the BH taking all of its energy along with it, meaning none of it is radiated. But in real circumstances the matter that is accreting onto the BH has angular momentum so that an accretion disc is formed. The accretion rate of the disc can be defined as

$$\dot{M} = 2\pi R v_r \sum = constant \tag{1.9}$$

with the radial in-spiral velocity of disc material v_r, the surface density $\sum = \int_0^H \rho(r_\tau) dr_\tau \approx \langle \rho(r_\tau) \rangle H$ and $\rho(r_\tau)$ the gas density at disc thickness H. The direct dependence between the accretion rate and opacity can be seen from equation (1.7) and equation (1.9).

The Eddington accretion rate $\dot{M}_{Edd}$ is where the disc luminosity is equal to the Eddington luminosity so that it follows from equations (1.5) and (1.8) that

$$\frac{4\pi c G M_{BH}}{\kappa} = \epsilon \dot{M}_{Edd} c^2 \tag{1.10}$$

$$\Rightarrow \quad \dot{M}_{Edd} = \frac{4\pi G M_{BH} m_p}{\epsilon c \sigma_T}. \tag{1.11}$$

1.2.2.1.2 Thin Accretion disc Spectrum

The following calculations are done by assuming geometrically thin, optically thick (opaque) accretion discs. FSRQs have very high accretion rates which results in them having optically thick accretion discs (Cao, 2018; Netzer, 2013). A description of the temperature profile and emission as a function of radius will now be given.

The local disc spectrum is assumed to be in the form of black body radiation, with every annulus between R and $R + RdR$ of the accretion disc radiating as a black body. The emissivity per unit area can be parametrised as (Netzer, 2013),

$$Q(R) = \sigma T(R)^4 \tag{1.12}$$

with σ the Stefan Boltzman constant and $T(R)$ the temperature of the disc at radius R. This temperature is dependent on the BH mass M_{BH} and the accretion rate $\dot{M}$, as

$$T(R) = \left[\frac{3 G M_{BH} \dot{M}}{8\pi\sigma R^3} \right]^{1/4} \left(1 - \sqrt{\frac{R_{in}}{R}} \right)^{1/4}, \tag{1.13}$$

where R_{in} is the inner disc radius. This can be rewritten as(Carroll and Ostlie, 2014),

$$T(R) = T_0 \left(\frac{R_{in}}{R} \right)^{3/4} \left(1 - \sqrt{\frac{R_{in}}{R}} \right)^{1/4}, \tag{1.14}$$

with

$$T_0 = \left(\frac{3 G M_{BH} \dot{M}}{8\pi\sigma R_{in}^3} \right)^{1/4}. \tag{1.15}$$

Differentiating equation (1.14) to R and setting the result equal to zero gives the radius where the maximum disc temperature occurs for a SS accretion disc model. The calculation for this is shown in more detail in Appendix A. The important thing to keep in mind is that

$T_0 \propto R^{-3/4}$. The maximum disc temperature is found to be at a radius of $R = 49/36 \cdot R_{in}$ and by substituting this into equation (1.14), the maximum temperature is found as

$$T_{max} = \frac{6\sqrt{6}}{7^{7/4}} \cdot T_0 \tag{1.16}$$

$$T_{max} = \frac{6\sqrt{6}}{7^{7/4}} \left(\frac{3GM_{BH}\dot{M_{Edd}}}{8\pi\sigma(3R_s)^3} \right)^{1/4} \tag{1.17}$$

$$T_{max} \sim 10^5 \text{ K} \tag{1.18}$$

for $M_{BH} \sim 10^9$ $M_\odot$.

The radiation spectrum for a SS accretion disc model will now be described by calculating the expression for the luminosity L_ν at a frequency ν (Shakura and Sunyaev, 1973). Again, each annulus of the accretion disc is treated as a black body spectrum. For a black body spectrum the intensity is given by the Planck function:

$$I_\nu(R) = B_\nu(T(R)) = \frac{2h\nu^3}{c^2} \left(e^{h\nu/(kT(R))} - 1 \right)^{-1}, \tag{1.19}$$

where $T(R)$ is the temperature defined in equation (1.13). The intensity at a frequency ν is defined as the amount of energy through an area element dA in time dt given by (Böttcher et al., 2012) as

$$I_\nu = \frac{d^4E}{dAdtd\nu d\Omega}, \tag{1.20}$$

which is measured in $\text{erg} \cdot \text{cm}^{-2} \cdot \text{s}^{-1} \cdot \text{Hz}^{-1} \cdot \text{sr}^{-1}$ and the luminosity at a frequency ν is given by

$$L_\nu = \frac{d^2E}{dtd\nu}. \tag{1.21}$$

From equations (1.20) and (1.21) it follows that $dL_\nu/(\int \cos\theta d\Omega) = \int I_\nu dA$, where the $\cos\theta$ factor is included because black bodies are Lambertian radiators. This means that the intensity has the same value in every direction that it is emitted. But, the intensity that we observe is multiplied by the cosine of the angle between the direction of observation and the surface normal of the source. The luminosity is calculated by integrating the black body flux over the surface area on the one side of the disc (Shakura and Sunyaev, 1973),

$$\frac{dL_\nu}{\int \cos\theta d\Omega} = \int_{R_{in}}^{R_{max}} B_\nu(T(R)) 2\pi R dR \tag{1.22}$$

$$dL_\nu = \int_{R_{in}}^{R_{max}} B_\nu(T(R)) 2\pi R dR \int \cos\theta d\Omega \tag{1.23}$$

$$dL_\nu = \int_{R_{in}}^{R_{max}} B_\nu(T(R)) 2\pi R dR \int_0^{2\pi} d\phi \int_0^{\pi/2} \cos\theta \sin\theta. \tag{1.24}$$

where the solid angle $d\Omega = \sin\theta d\theta d\phi$. For the spectrum from both sides of the disc, the luminosity is

$$L_\nu = 2 \int_{R_{in}}^{R_{max}} B_\nu(T(R)) 2\pi R dR \int_0^{2\pi} d\phi \int_0^{\pi/2} \cos\theta \sin\theta \tag{1.25}$$

$$L_\nu = 4\pi \int_{R_{in}}^{R_{max}} B_\nu(T(R)) R dR \cdot 2\pi \left[\frac{\sin^2\theta}{2}\right]_0^{\pi/2} \tag{1.26}$$

$$L_\nu = 4\pi^2 \int_{R_{in}}^{R_{max}} B_\nu(T(R)) R dR \tag{1.27}$$

$$L_\nu = \frac{8\pi^2 h\nu^3}{c^2} \int_{R_{in}}^{R_{max}} \left(e^{h\nu/(kT(R))} - 1\right)^{-1} R dR. \tag{1.28}$$

The corresponding flux is

$$F_\nu^d = \frac{L_\nu^d}{4\pi d_L^2} \tag{1.29}$$

$$F_\nu^d = \frac{2\pi h\nu^3}{\pi c^2 d_L^2} \int_{R_{in}}^{R_{max}} \left(e^{h\nu/(kT(R))} - 1\right)^{-1} R dR, \tag{1.30}$$

where d_L is the disc luminosity distance.

The expected spectrum for an accretion disc is shown in Figure 1.11 where the accretion disc is visible in the optical/UV band. The corona will not be considered in our model since it does not give a significant flux contribution. The accretion disc spectrum in Figure 1.11 will now be described from left to right.

Different regions within the disc emit different temperatures at different frequencies. The first part of the spectrum follows a black body spectrum $F_\nu \propto \nu^2$ (Netzer, 2013). The spectrum then shows a break at the frequency $\nu_{out} \sim 2.8 \cdot kT(R_{out})/h$, where the outer disc radius is R_{out}. The next break at frequency ν_{in} corresponds to the inner radius R_{in} of the disc where the temperature will be at a maximum. The maximum temperature of the disc is given by equation (1.18) and at maximum disc luminosity for $M_{BH} = 10^9$ $M_\odot$ it is emitted at the frequency $\nu_{in} = 2.8 \cdot kT_{max}/h \sim 4.6 \times 10^{15}$ Hz, with $T_{max} \propto \dot{l}^{1/4} M_{BH}^{-1/4}$ with $\dot{l} = \dot{M}_{BH}/\dot{M}_{Edd} = L_d/L_{Edd}$. In the frequency range ν_{out}, the spectrum follows as $F_\nu \propto \nu^{1/3}$. For frequencies larger than ν_{in} the spectrum decreases exponentially as $L_\nu \propto e^{-h\nu/(kT_{max})}$.

1.2.2.2 Emission Lines from the Broad Line Region

The prominent emission lines in the optical spectrum of quasars are redshift dependent (Frank et al., 2002). When the source has a low redshift, the hydrogen Balmer lines will dominate. At high redshifts the C, Mg, and Lyα hydrogen lines that are in the UV regime in the co-moving frame are redshifted into the optical regime in the observers frame. Emission line peaks in spectra can for our purposes be assumed to be in the form of a Gaussian:

$$G(\nu, \mu, \sigma) = b \cdot e^{-\frac{(\nu-\mu)^2}{2(\sigma^2)}} \tag{1.31}$$

where b is the height of the emission line, μ is the frequency at which the peak is emitted and σ is the standard deviation, that is the width of the emission line.

1.2.2.3 Synchrotron Radiation

This section will first describe the geometry of the power emission of a gyrating particle and thereafter three different ways are given in which the synchrotron radiation can be calculated.

A description of a typical synchrotron spectrum is given.

Relativistic particles gyrate around a magnetic field (Figure 1.13, left). In the electron's rest frame, the angular distribution of its emitted power has a doughnut shape (Figure 1.13, middle) (Rybicki and Lightman, 1979). The magnetic field accelerates electrons and this accelerated motion causes them to lose energy which is carried away by photons. The radiation is beamed in the direction in which the electron is moving (Longair, 2011). For non-relativistic particles the radiation is called *cyclotron radiation* and for the relativistic particles, it is called *synchrotron radiation* (Rybicki and Lightman, 1979). The angular distribution of cyclotron radiation has a characteristic doughnut shape, while the angular distribution of synchrotron radiation has a characteristic shape where the lobe in the direction of the motion of the particle extends farther out than the backward lobe (illustrated in the middle and right of Figure 1.13, respectively).

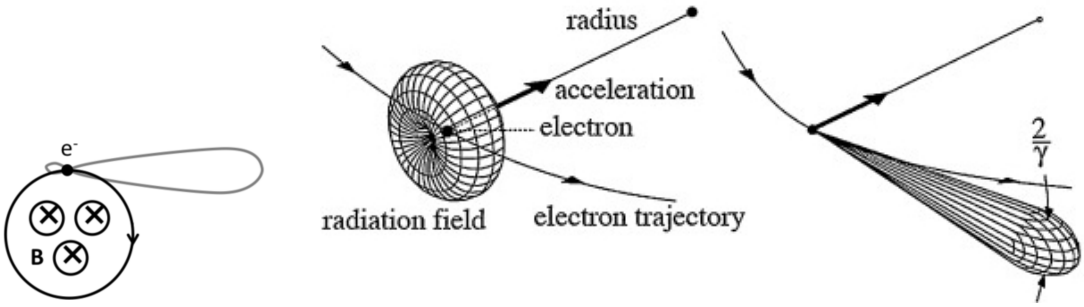

Figure 1.13: **Left:** The magnetic field is shown to be into the page with the orbit of the electron around it. The area within the grey lines illustrates the radiation of the electron. **Middle:** Angular distribution of cyclotron radiation in a characteristic doughnut shape. **Right:** Angular distribution of synchrotron radiation in an extended forward lobe. The left illustration is taken from *Spectral Properties of Synchrotron Radiation* (2010). The middle and right illustrations are taken from Eberhardt (2015).

The extended forward lobe is due to relativistic beaming and Doppler shift. The forward lobe has emission in the angle $2/\gamma$, with the half angle $\theta = 1/\gamma$ and contains much more power than the backward lobe As the electron gyrates along the magnetic field, an observer will see this beam of radiation for a short time (see Figure 1.14). The observer can see radiation from cone 1 when the velocity of the particle is at an angle $1/\gamma$ to the LOS and will continue seeing radiation until the velocity is again at this angle at the other side of the observer's LOS at cone 2 (Rybicki and Lightman, 1979). There is a triangle for which the angle of the orbit $\Delta\theta$ constitutes the one angle and the other two angles are equal to $\pi/2 - 1/\gamma$, so that $\Delta\theta = 2/\gamma$. The duration of emission is $\Delta t_{em} = \Delta\theta/\omega_g$ where $\omega_g = Bq/(\gamma m_e c)$ is the gyration frequency with B the magnetic field, q the electron charge and m_e the mass of the electron. The time that the radiation takes to travel from 1 to 2 is $\Delta t_{travel} = \beta \cdot \Delta\theta/\omega_g$ so that the time within which the radiation is observed is

$$\Delta t_{obs} = \Delta t_{em} - \Delta t_{travel} = \frac{2}{\omega_g \gamma}(1 - \beta). \tag{1.32}$$

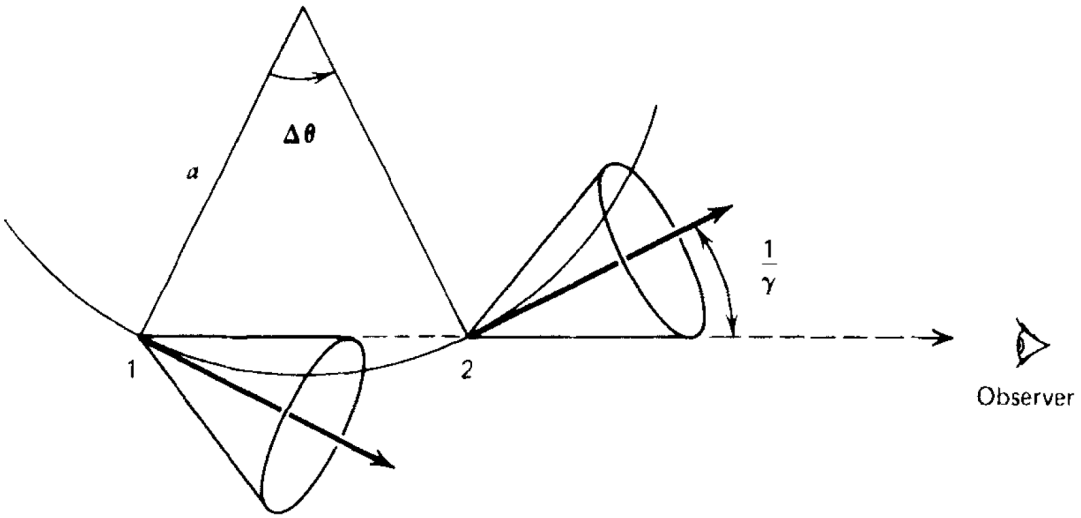

Figure 1.14: Power emitted within beams at different times at point 1 and point 2, during the gyration of the beam with half-angle $\theta = 1/\gamma$. The labels a and $\Delta\theta$ are used to indicate the radius of the orbit and the angle between point 1 and 2, respectively. This figure is taken from Rybicki and Lightman (1979).

Since $1-\beta = (1-\beta^2)/(1+\beta) = 1/(\gamma^2(1+\beta)) \approx 1/(2\gamma^2)$, it follows that $\Delta t_{obs} = 1/(\omega_g\gamma^3) = m_e c/(Bq\gamma^2)$ so that the observed synchrotron frequency has the dependence

$$\nu_{obs}^{sy} = \frac{1}{\Delta t_{obs}} \propto B\gamma^2. \tag{1.33}$$

1.2.2.3.1 Radiative Power Output

Böttcher et al. (2012) describes three possible functions to calculate synchrotron radiation. These functions are compared to each other in Figure 1.15. The third function is used within our model.

1. For a particle with energy $E = \gamma mc^2$ moving at a pitch angle η to a magnetic field B, the synchrotron radiative power is given by Rybicki and Lightman (1979) as

$$P_\nu^{sy}(\gamma;\eta) = \frac{\sqrt{3}q^3 B}{mc^2}\sin\eta\ F(x) \tag{1.34}$$

where $x = \nu/\nu_\eta$ with $\nu_\eta = \gamma^2 3qB\sin\eta/(4\pi mc)$ and

$$F(x) = x\int_x^\infty K_{5/3}(\xi)d\xi, \tag{1.35}$$

where $K_{5/3}$ is the modified Bessel function of order 5/3. The function $F(x)$ is shown in Figure 1.16, having the asymptotes

$$F(x) \propto \begin{cases} x^{1/3} & \text{for } x \ll 1 \\ x^{1/2}e^{-x} & \text{for } x \gg 1. \end{cases} \tag{1.36}$$

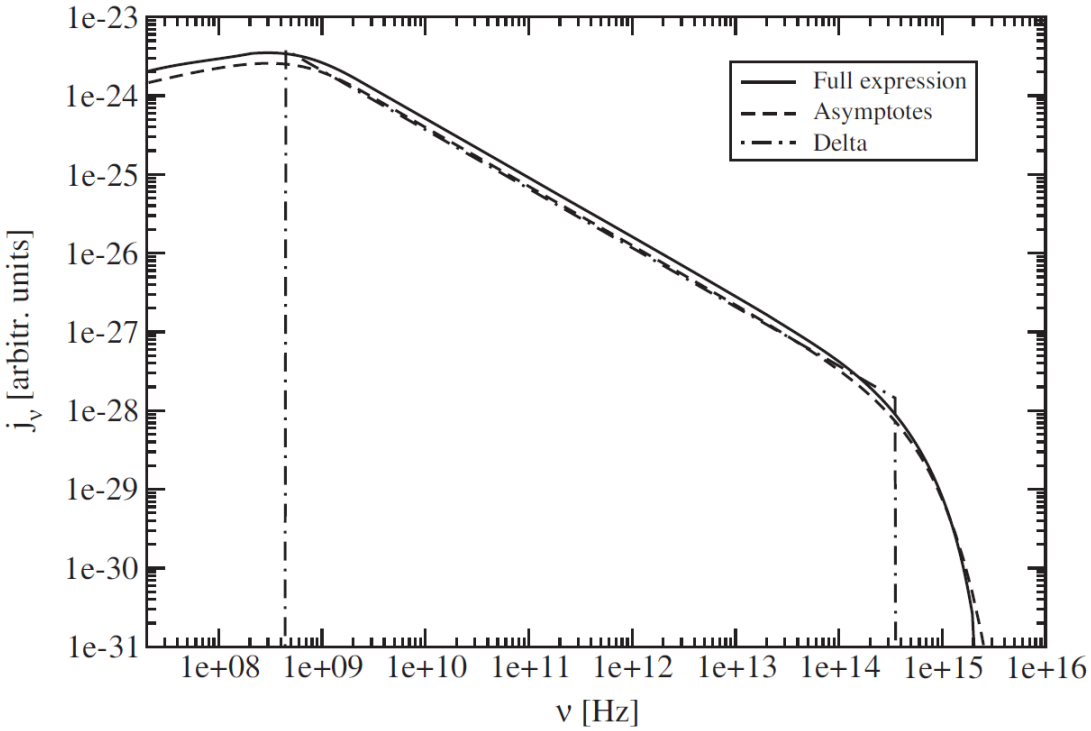

Figure 1.15: This figure shows the synchrotron spectrum using the full function, δ-function approximation and the $\nu^{1/3}e^{\nu/\nu_{cr}}$ approximation for a pure power law relativistic electron distribution with index $p = 2.5$ and energy cut-offs $\gamma_1 = 10$ and $\gamma_2 = 10^4$. This is for a magnetic field $B = 1$ G. This graph is taken from Böttcher et al. (2012)

For a collection of particles with isotropic pitch angle distributions the angle-averaged synchrotron radiation is given by

$$P_\nu^{sy}(\gamma) = \frac{1}{4\pi}\int_{4\pi} P_\nu^{sy}(\gamma;\eta)d\Omega. \tag{1.37}$$

The full expression is evaluated by Crusius and Schlickeiser (1986) and found as

$$P_\nu^{sy}(\gamma) = \frac{\sqrt{3}\pi q^3 B}{2mc^2} xCS(x), \tag{1.38}$$

where $CS(x)$ is a function of Whittaker functions

$$CS(x) = W_{0,\,4/3}(x)\,W_{0,\,1/3}(x) - W_{1/2,\,5/6}(x)\,W_{-1/2,\,5/6}(x), \tag{1.39}$$

and $x = \nu/\nu_{cr}$, with the critical frequency

$$\nu_{cr} = \frac{3qB}{4\pi mc}\gamma^2 = 4.2\times 10^6 B_G \gamma^2 Z\frac{m_e}{m}\text{Hz}. \tag{1.40}$$

The $xCS(x)$ function can be seen in Figure 1.16 to have a dependence on $x^{1/3}$ for low frequencies and an exponential cut-off at high frequencies, similar to the $F(x)$ function (Böttcher et al., 2012). The peak occurs around ν_{cr}. It can be time-consuming to use the full equation to calculate the synchrotron flux.

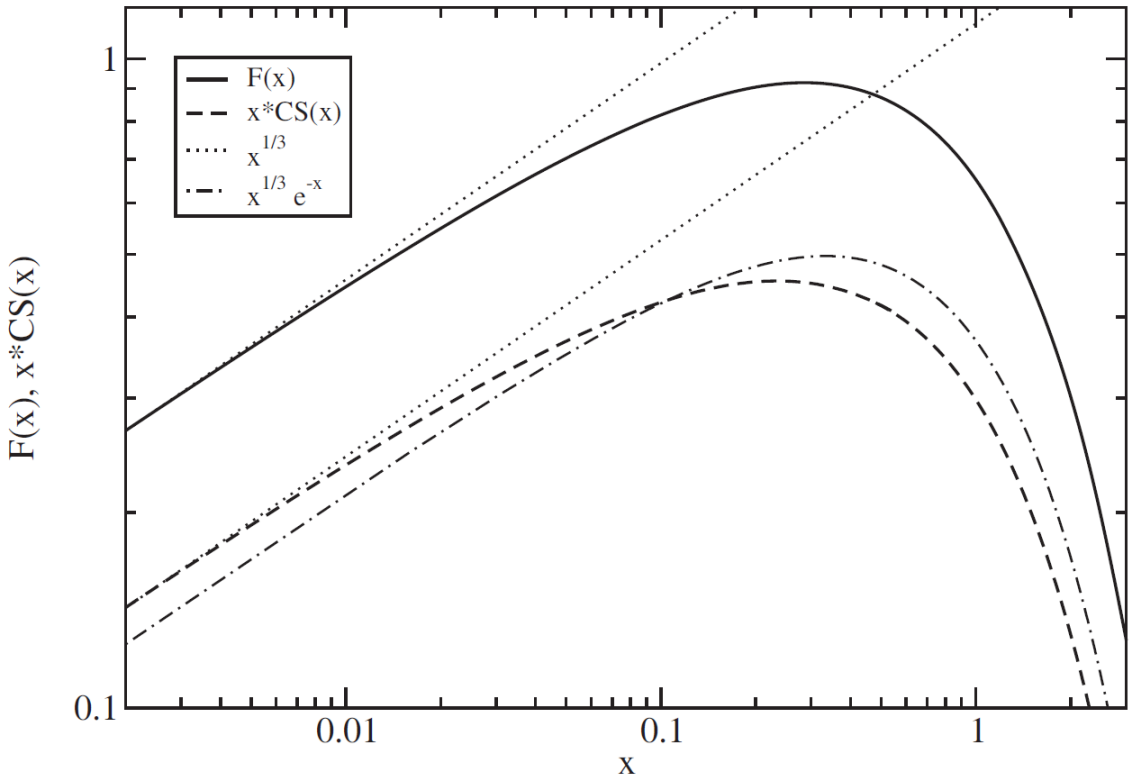

Figure 1.16: The synchrotron power for a single particle as described by $F(x)$ and $x*CS(x)$ is graphed as a function of $x = \omega/\omega_c$. On this graph, $x^{1/3}$ describes the low frequency asymptote. A $x^{1/3}e^{-x}$ approximation can be seen. This figure is taken from Böttcher et al. (2012).

2. For practical applications, the δ-function approximation can be used, which is given by Böttcher et al. (2012) as

$$P_\nu^{sy,\,\delta}(\gamma) = \frac{32\pi c}{9}\left(\frac{q^2}{mc^2}\right)^2 u_B\beta^2\gamma^2\delta(\nu-\nu_{cr}). \tag{1.41}$$

This δ-function represents the synchrotron emissivity when the photon output is at a maximum for electron energies γ at ν_{cr} (equation 1.40). This allows for an electron distribution with a power law profile and a spectral index p, which reproduces the synchrotron photon power law index $\alpha_{sy} = (p-1)/2$ (equation 1.2). In Figure 1.15 it can be seen that the approximation agrees fairly well where the function follows a power law, but not at the lower and higher energy cut-offs $\nu_c = \nu_0\gamma_{1,2}^2$.

3. In Figure 1.16 it can be seen that $x^{1/3}e^{-x}$ approximates the full expression $xCS(x)$ rather well. The $\nu^{1/3}e^{-\nu/\nu_{cr}}$ approximation can be found by normalizing the total emitted power so that it entails a multiplication of this asymptotic behaviour:

The total emitted power as derived by Rybicki and Lightman (1979) is

$$P_{tot}^{sy}(\gamma) = \frac{4}{3}u_B c\sigma_T\beta^2\gamma^2. \tag{1.42}$$

Knowing that the gamma function has the form $\Gamma(z) = \int_0^\infty x^{z-1}e^{-x}dx$, it follows by substituting in $x = \nu/\nu_{cr}$ that

$$\Gamma\left(\frac{4}{3}\right) = \nu_{cr}^{-4/3}\int_0^\infty \nu^{1/3}e^{-\nu/\nu_{cr}}d\nu, \tag{1.43}$$

$$1 = \frac{1}{\Gamma\left(\frac{4}{3}\right)}\cdot\nu_{cr}^{-4/3}\int_0^\infty \nu^{1/3}e^{-\nu/\nu_{cr}}d\nu. \tag{1.44}$$

With this the total emitted power can be normalized as

$$P_{tot}^{sy}(\gamma) = \frac{4}{3}u_B c\sigma_T\beta^2\gamma^2\cdot\frac{1}{\Gamma(\frac{4}{3})\nu_{cr}^{4/3}}\int_0^\infty \nu^{1/3}e^{-\nu/\nu_{cr}}d\nu. \tag{1.45}$$

Solving for the radiative power output $P_\nu^{sy}(\gamma)$ at a frequency ν

$$\int_0^\infty P_\nu^{sy}(\gamma)d\nu = P_{tot}^{sy}(\gamma) \tag{1.46}$$

$$P_\nu^{sy}(\gamma) = \frac{4}{3}u_B c\sigma_T\beta^2\gamma^2\cdot\frac{1}{\Gamma(\frac{4}{3})\nu_{cr}^{4/3}}\nu^{1/3}e^{-\nu/\nu_{cr}}. \tag{1.47}$$

The Thomson cross section

$$\sigma_T = \frac{8\pi r_e^2}{3} \tag{1.48}$$

$$\sigma_T = \frac{8\pi}{3}\left(\frac{q^2}{m_e c^2}\right)^2, \tag{1.49}$$

where $r_e = q^2/(m_e c^2)$ is the classical electron radius.
Substituting the Thompson cross section in equation (1.47), it follows that

$$P_\nu^{sy}(\gamma) = \frac{4}{3}u_B c\left[\frac{8\pi}{3}\left(\frac{q^2}{m_e c^2}\right)^2\right]\beta^2\gamma^2\cdot\frac{1}{\Gamma(\frac{4}{3})\nu_{cr}^{4/3}}\nu^{1/3}e^{-\nu/\nu_{cr}} \tag{1.50}$$

$$P_\nu^{sy}(\gamma) = \frac{32\pi c}{9\Gamma(\frac{4}{3})}\left(\frac{q^2}{m_e c^2}\right)^2 u_B\beta^2\gamma^2\cdot\frac{\nu^{1/3}}{\nu_{cr}^{4/3}}e^{-\nu/\nu_{cr}}. \tag{1.51}$$

1.2.2.3.2 The Synchrotron Spectrum

The luminosity spectrum of a source is defined as

$$L_\nu(\gamma) = \int P_\nu(\gamma)N(\gamma)d\gamma. \tag{1.52}$$

Using the asymptotic approximation in equation (1.51), the synchrotron luminosity at frequency ν can be calculated as

$$L_\nu^{sy}(\gamma) = \frac{32c\nu^{1/3}}{9\Gamma(\frac{4}{3})}\left(\frac{q^2}{mc^2}\right)^2\frac{B^2}{8\pi}\int_{\gamma_1}^{\gamma_2}\beta^2\gamma^2(\nu_0\gamma^2)^{-4/3}e^{-\nu/(\nu_0\gamma^2)}N_e(\gamma)d\gamma. \tag{1.53}$$

The flux of the source at a frequency ν can be calculated as

$$F_\nu^{sy} = \frac{L_\nu^{sy}}{4\pi d^2} \tag{1.54}$$

$$F_\nu^{sy} = \frac{1}{4\pi d^2} \cdot \frac{32c\nu^{1/3}}{9\Gamma(\frac{4}{3})} \left(\frac{q^2}{mc^2}\right)^2 \frac{B^2}{8\pi} \int_{\gamma_1}^{\gamma_2} \beta^2\gamma^2(\nu_0\gamma^2)^{-4/3} e^{-\nu/(\nu_0\gamma^2)} N_e(\gamma) d\gamma. \tag{1.55}$$

By substituting the electron distribution equation (1.1) into equation (1.55), it can be seen in our case (for a broken power law and exponential cut-off electron distribution) that the flux should follow as

$$F_\nu^{sy}(\gamma) \propto \begin{cases} \nu^{1/3} & \text{for } \nu \leq \nu_{min} \\ \nu^{-(\frac{p_1-1}{2})} = \nu^{-\alpha_1} & \text{for } \nu_{min} \leq \nu \leq \nu_b \\ \nu^{-(\frac{p_2-1}{2})} \cdot e^{-\nu/\nu_c} = \nu^{-\alpha_2} \cdot e^{-\nu/\nu_c} & \text{for } \nu_b \leq \nu \leq \nu_c \end{cases} . \tag{1.56}$$

1.2.3 High-Frequency Radiation Models for Blazars

The high-frequency radiation in the UV through gamma-ray is calculated by taking into account the contributions from SSC emission and External Compton (EC) emission. When photons are scattered by relativistic electrons, the process is called *Inverse Compton scattering*. The electrons are then in two processes; first they emit photons in a synchrotron radiation process and then they receive or emit energy from photons in a Compton scattering process and thereby they are said to be in a *Synchrotron Self-Compton* (SSC) process. When the seed photons are produced outside of the jet, the Compton scattering emission is called EC emission (*Radiative Processes in High Energy Astrophysics*, 2013).

There are two different models that can describe the high frequency emission from AGN, namely the Leptonic and Hadronic models. The difference between the Leptonic and the Hadronic models is the particles that produce their radiation in their high-frequency components (Cerruti et al., 2017). The Leptonic model has an electron distribution in its emission region (blob). In the Hadronic model the emission region contains a distribution of relativistic electrons and protons. In the Hadronic model it is the protons that lose energy through processes such as photo-pion production and pair production to emit gamma-rays (Mastichiadis, 1996). The Leptonic and Hadronic models are described separately in the following paragraphs.

1.2.3.1 Leptonic SED-model

In Leptonic models the radiation in the EM spectrum is dominated by leptons (electrons, with the possibility of positrons) (Böttcher et al., 2013). The possible protons that are in the emission region are not accelerated to high enough energies to contribute to the radiation output (Böttcher et al., 2012; Böttcher et al., 2013). However, the proton energy should still be included in total energy considerations. This is because momentum carried by the jet can sometimes be dominated by the more massive protons. The electrons cause synchrotron radiation at low frequencies, that can Compton scatter low-energy photons to high-energy radiation. The SED of this model (Figures 1.3 and 1.21) has a low-frequency component

that is the sum of the electron-synchrotron and (thermal) accretion disc radiation. Its high-frequency component is the sum of the SSC radiation and the EC scattering radiation from the disc and the BLR (Zhang and Böttcher, 2013).

1.2.3.2 Hadronic SED-model

The low-frequency component of the Hadronic model is the sum of the electron-synchrotron and accretion disc radiation. In the high-frequency component the radiation in the X-ray and gamma-ray bands is due to proton-proton interactions or photo-pion interactions ($p + \gamma \rightarrow \pi^0 + p$ or $p + \gamma \rightarrow n + \pi^+$) which produce particle cascades ($\pi^0 \rightarrow \gamma$-ray+γ-ray or $n \rightarrow e^- + \bar{\nu}_e + p$ and $\pi^+ \rightarrow \mu^+ + \nu_\mu$ where $\mu^+ \rightarrow e^+ + \bar{\nu}_\mu + \nu_e$ or for π^- decay $\mu^- \rightarrow e^- + \nu_\mu + \bar{\nu}_e$). These cascades produce gamma-rays and provide the necessary particles for photon-photon production, synchrotron radiation of relativistic protons and synchrotron radiation from secondary electron-positron pairs (when γ-ray+$\gamma \rightarrow e^- + e^+$) (Böttcher et al., 2012; Cerruti et al., 2017; Katz and Spiering, 2012; Mastichiadis, 1996; Zhang and Böttcher, 2013). These particle processes are illustrated in Figure 1.17. Protons will always undergo synchrotron radiation, but if they have high enough energies they can undergo photo-pion production to produce EM cascades (Böttcher, 2007; Böttcher et al., 2013). The different radiation components of the Hadronic model are illustrated in the SEDs of Figures 1.3 and 1.21.

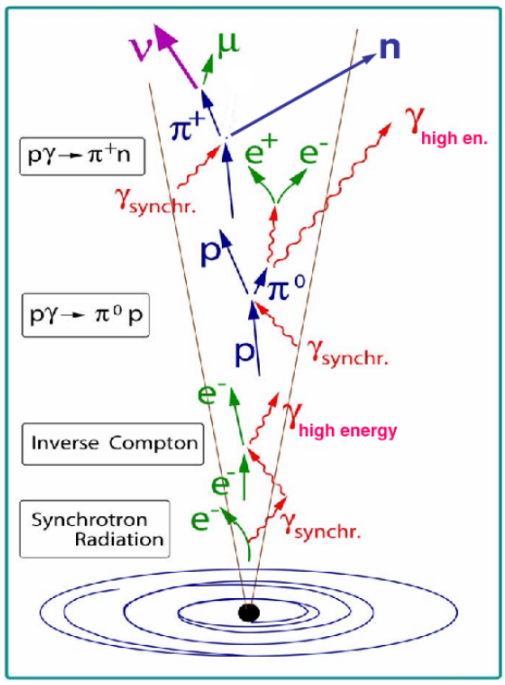

Figure 1.17: Schematic of particle processes of the Hadronic model. At the top of the figure it is shown that a neutron can escape the magnetic field and decay outside of the jet to provide the cosmic rays detected on Earth (Katz and Spiering, 2012). This figure is taken from Katz and Spiering (2012).

1.2.4 Polarisation

Polarisation is described on a very basic level and then a specific explanation for synchrotron polarisation is given. A short description is given on the polarisation for the high-energy models.

The polarisation of an electromagnetic wave is defined by the direction of its oscillating electric field vector. The wave equation for an electric field **E** can be calculated with Maxwell's equations (Griffiths, D. J., 2013). Faraday's law is given by

$$\nabla \times \boldsymbol{E} = \frac{\partial \boldsymbol{B}}{\partial t}. \tag{1.57}$$

Taking the curl of Faraday's law yields

$$\begin{aligned} \nabla \times (\nabla \times \boldsymbol{E}) &= -\frac{\partial}{\partial t}(\nabla \times \boldsymbol{B}) & (1.58)\\ \nabla(\nabla \cdot \boldsymbol{E}) - \nabla^2 \boldsymbol{E} &= -\frac{\partial}{\partial t}(\mu_0 \boldsymbol{J} + \mu_0 \epsilon_0 \frac{\partial}{\partial t}\boldsymbol{E}) & (1.59)\\ \nabla^2 \boldsymbol{E} &= \mu_0 \epsilon_0 \frac{\partial^2}{\partial t^2}\boldsymbol{E} + \mu_0 \frac{\partial}{\partial t}\boldsymbol{J} + \nabla(\frac{\rho}{\epsilon_0}) & (1.60) \end{aligned}$$

where $\boldsymbol{J}$ is the current density, ρ is the charge density, $\nabla \times (\nabla \times \boldsymbol{E}) = \nabla(\nabla \cdot \boldsymbol{E}) - \nabla^2 \boldsymbol{E}$ is a vector identity, $\nabla \times \boldsymbol{B} = \mu_0 \boldsymbol{J} + \mu_0 \epsilon_0 \cdot \partial \boldsymbol{E}/\partial t$ is Ampére's law with Maxwell's correction and Gauss's law $\nabla \cdot \boldsymbol{E} = \rho/\epsilon$. This is in the form of the inhomogeneous wave equation $\nabla^2 \varphi = \partial^2 \varphi/(c^2 \partial t^2) + A$, with $c = 1/\sqrt{\mu_0 \epsilon_0}$. For a homogeneous wave equation that is far away from the source where $\rho = 0$ and $\boldsymbol{J} = 0$,

$$\nabla^2 \boldsymbol{E} = \mu_0 \epsilon_0 \frac{\partial^2 \boldsymbol{E}}{\partial t^2}. \tag{1.61}$$

The homogeneous wave equation for the magnetic field $\nabla^2 \boldsymbol{B} = \mu_0 \epsilon_0 \cdot \partial^2 \boldsymbol{B}/\partial t^2$ can also be calculated with Maxwell's equations. The solutions of the wave equations are given as

$$\begin{aligned} \boldsymbol{E}(\boldsymbol{r}, t) &= E_0 \cdot \cos(\boldsymbol{k} \cdot \boldsymbol{r} - \omega t + \delta)\hat{\boldsymbol{n}} & (1.62)\\ \boldsymbol{B}(\boldsymbol{r}, t) &= B_0 \cdot \cos(\boldsymbol{k} \cdot \boldsymbol{r} - \omega t + \delta)(\hat{\boldsymbol{k}} \times \hat{\boldsymbol{n}}) & (1.63) \end{aligned}$$

where E_0 and B_0 are the amplitudes of the E and B wave equations, $\boldsymbol{k}$ is the wave vector and $\hat{\boldsymbol{n}}$ the direction of polarisation in the direction of $\boldsymbol{E}$. For these transverse waves $\hat{\boldsymbol{n}} \cdot \hat{\boldsymbol{k}} = 0$, with $\boldsymbol{E}$ and $\boldsymbol{B}$ perpendicular to each other in the relationship $\boldsymbol{B} = (\hat{\boldsymbol{k}} \times \boldsymbol{E})/c$.

The light we receive can be circularly polarised, linearly polarised or elliptically polarised. Figure 1.18 shows the electron's velocity vector described by a velocity cone, as it gyrates along the magnetic field. The acceleration $\boldsymbol{a}$ of the electron will be in the direction of $\boldsymbol{v} \times \boldsymbol{B}$ (Longair, 2011). Linear polarisation will be observed when our LOS is perpendicular to the magnetic field. If our LOS is parallel to the magnetic field, the electric field oscillation in the beam of the electron will be seen to move in a circle as the electron orbits around the magnetic field. This is called circular polarisation (Figure 1.19) and can be in both rotation

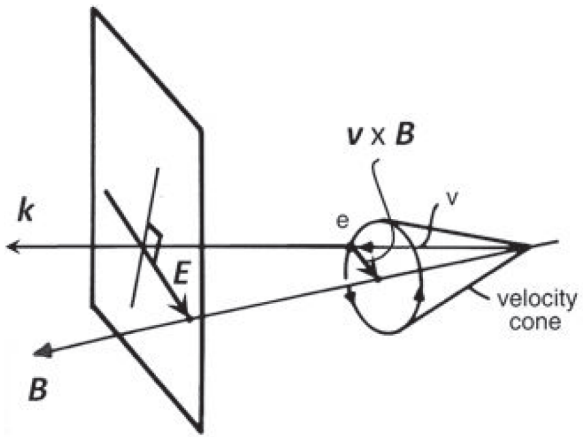

Figure 1.18: Geometry of synchrotron polarisation. This figure was taken from Longair (2011).

directions, that is left- or right handed, depending on whether the magnetic field is pointing in our direction or away from us. If the gyration of the electron is viewed with our LOS at an inclination angle to the magnetic field, elliptical polarisation is seen. Elliptical polarisation can also be left- or right handed depending from which side it is observed. For elliptical polarisation the electric field vector will trace out an ellipse in the x-y plane (Figure 1.19). The amplitudes of the wave in the x and y direction $E_x \neq E_y$. The x and y components are in a different phase δ, so that for a wave moving in the z-direction

$$\boldsymbol{E_x} = E_x \sin(kz - \omega t + \delta)\boldsymbol{x} \tag{1.64}$$

$$\boldsymbol{E_y} = E_y \sin(kz - \omega t)\boldsymbol{y} \tag{1.65}$$

for $\boldsymbol{E} = \boldsymbol{E_x} + \boldsymbol{E_y}$.

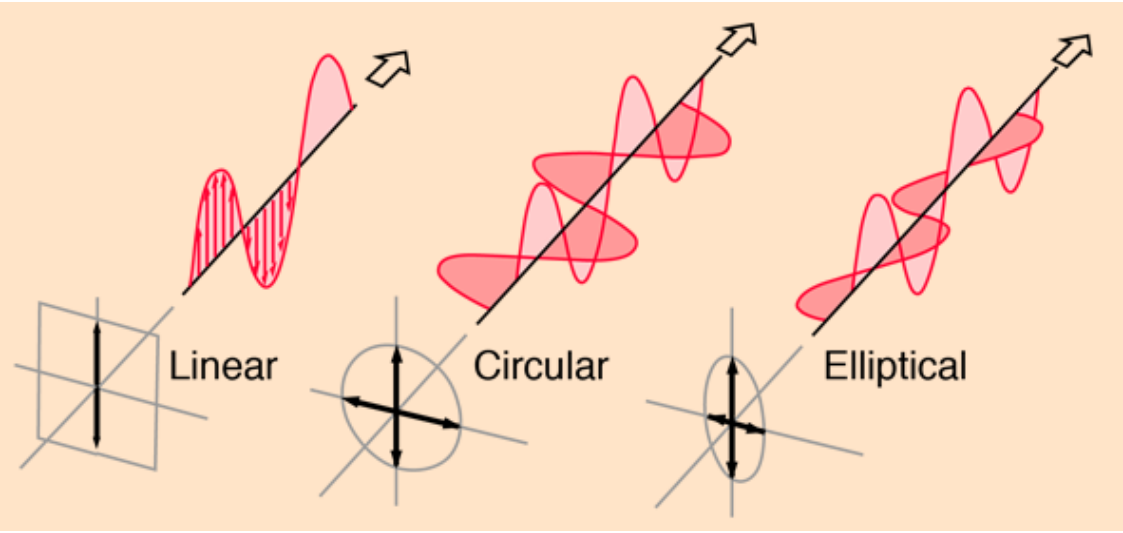

Figure 1.19: The classification of polarisation. This figure is taken form Nave (n.d.).

EM radiation can be composed out of components that are polarised and unpolarised. Po-

larimetry is the measurement of the polarisation of EM waves. The degree of polarisation tells us how much of the EM radiation is polarised. Observing 0% polarisation implies that the EM radiation is completely unpolarised, whereas 100% polarisation will mean that the radiation is completely polarised.

1.2.4.1 Synchrotron polarisation

Synchrotron emission has the attribute of being strongly polarised. A single relativistic electron (or other charged particle) produces elliptically polarised radiation (Rybicki and Lightman, 1979), as illustrated in Figure 1.19. For synchrotron polarisation the emission of not

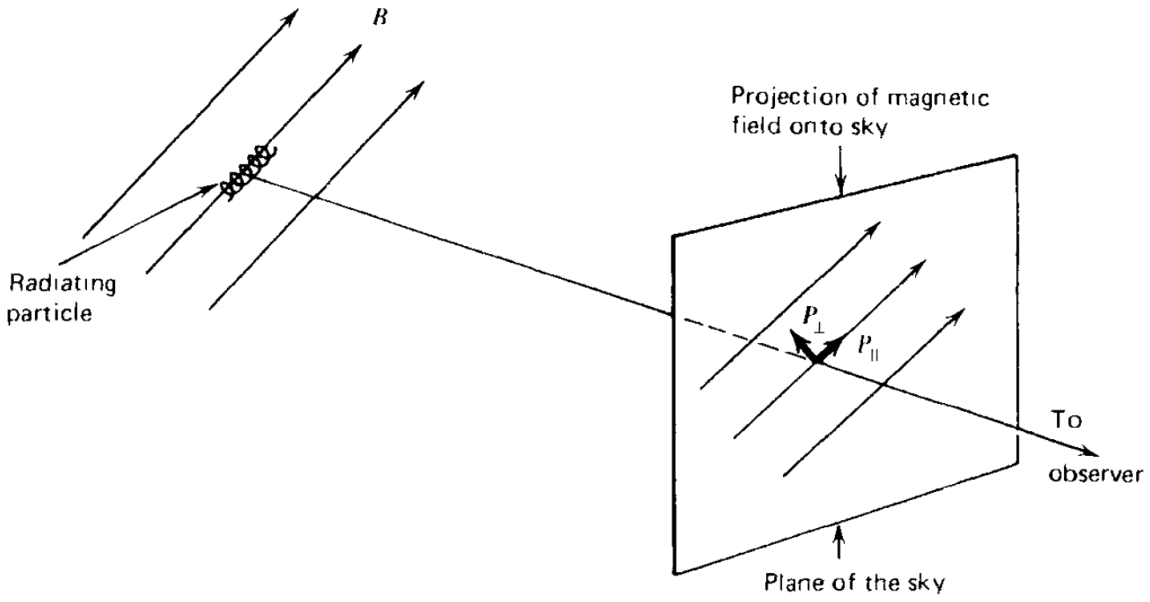

Figure 1.20: The power components $P_{\omega,\perp}$ and $P_{\omega,\parallel}$ with their electric field vectors perpendicular and parallel to the projection of the magnetic field on the plane of the sky. This figure is taken from Rybicki and Lightman (1979).

just one particle but a distribution of particles that are at different pitch angles to the magnetic field should be considered. Some electrons are observed to have radiation that is left hand polarised and some electrons are observed to have radiation that is right hand polarised at the same time. These can cancel each other out so that the overall radiation is mostly linearly polarised. Synchrotron radiation is then said to be partially linearly polarised and can be completely described by the power components $P_{\omega,\perp}$ and $P_{\omega,\parallel}$ (as illustrated in Figure 1.20), at a certain frequency. For a single particle, Rybicki and Lightman (1979) derived these powers at angular frequency $\omega = 2\pi\nu$ and found them as

$$P_{\omega,\perp} = \frac{\sqrt{3}q^3 B \sin\eta}{4\pi mc^2}[F(x) + G(x)], \tag{1.66}$$

$$P_{\omega,\parallel} = \frac{\sqrt{3}q^3 B \sin\eta}{4\pi mc^2}[F(x) - G(x)], \tag{1.67}$$

where $x = \omega/\omega_c$, $F(x)$ is defined in equation (1.35) and

$$G(x(\gamma)) = x(\gamma)K_{2/3}(x(\gamma)) \tag{1.68}$$

with $K_{2/3}$ the modified Bessel function of second kind of order 2/3.

For particles at a single energy γ the degree of linear polarisation is given as

$$\Pi_{\omega}^{sy} = F_B \cdot \frac{P_{\omega,\perp} - P_{\omega,\parallel}}{P_{\omega,\perp} + P_{\omega,\parallel}} = F_B \cdot \frac{G(x)}{F(x)}, \tag{1.69}$$

where F_B (unitless) indicates how well the magnetic field is ordered. For a distribution of electrons the synchrotron polarisation is calculated as

$$\Pi_{\omega}^{sy} = F_B \cdot \frac{\langle G(x) \rangle}{\langle F(x) \rangle}, \tag{1.70}$$

with

$$\langle G(x) \rangle = \int N_e(\gamma) G(x(\gamma)) d\gamma = \int N_e(\gamma) x(\gamma) K_{2/3}(x(\gamma)) d\gamma \tag{1.71}$$

$$\langle F(x) \rangle = \int N_e(\gamma) F(x(\gamma)) d\gamma = \int N_e(\gamma) x(\gamma) \int_{x(\gamma)}^{\infty} K_{5/3}(x(\xi)) d\xi d\gamma \tag{1.72}$$

by substitution of equation (1.68) and equation (1.35).

The maximum degree of polarisation for a power law distribution of electrons is given by Rybicki and Lightman (1979) as

$$\Pi_{max,\, powerlaw}^{sy} = F_B \cdot \frac{p+1}{p+\frac{7}{3}} = F_B \cdot \frac{\alpha_{sy}+1}{\alpha_{sy}+\frac{5}{3}}. \tag{1.73}$$

For a broken power law, two maximum polarisations can be calculated as will be shown in a plot in the next chapter.

The total polarisation Π_{ν} is calculated by knowing that the degree of linear polarisation will be a fraction of the total emission contributed by all the components. Since the accretion disc and emission lines are unpolarised, the total polarization will only be a fraction of the synchrotron polarization, giving

$$\Pi_{\nu} = \frac{\Pi_{\nu}^{sy} \cdot F_{\nu}^{sy}}{F_{\nu}^{sy} + F_{\nu}^{d} + F_{\nu}^{line}} \tag{1.74}$$

where F_{ν}^{line} is the flux of the lines.

1.2.4.2 High-Frequency Component Polarisation

Zhang and Böttcher (2013) developed a code to model the SSC polarisation. Their code includes the Leptonic and Hadronic models and is fitted to the observations from blazars.

The high-frequency component in the Leptonic model is from SSC and EC processes. Only the SSC polarisation is calculated, since the EC emission is expected to be unpolarised. For the Hadronic model the polarisation is calculated from the synchrotron emission from primary electrons and protons, the synchrotron emission from secondary electron-positron pairs produced in cascade processes and the SSC emission from primary electrons.

For the FSRQs, 3C279 and PKS 0528+134 (Figure 1.21), it is found that the Leptonic model produces a lower degree of polarisation compared to the Hadronic model. It is suggested that in order to distinguish between the Leptonic and Hadronic models, optical polarimetry should be included with X-ray and gamma-ray polarimetry, to constrain the ordering of the magnetic field.

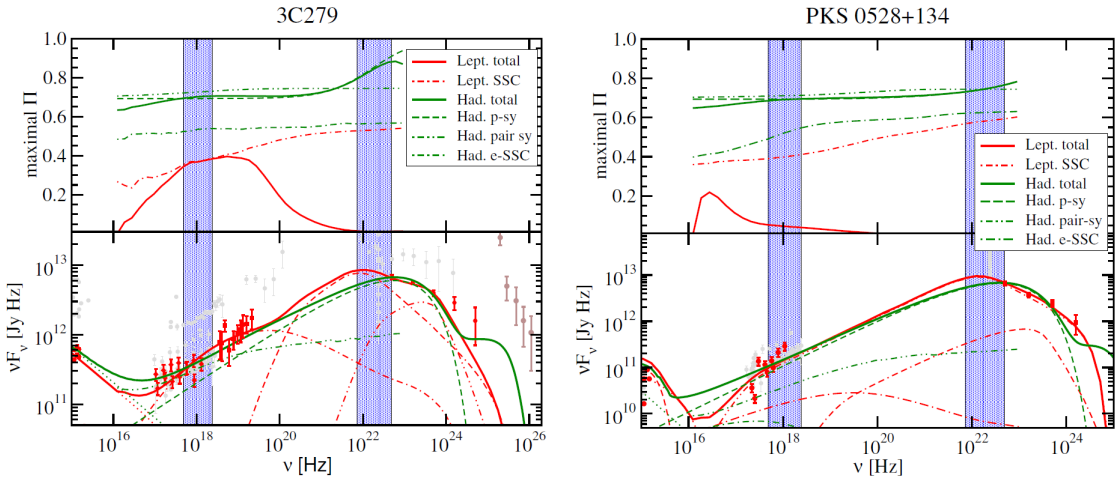

Figure 1.21: The high-frequency components produced by the Zhang and Böttcher (2013) code. Leptonic (red) and Hadronic models (green) and polarisation for the FSRQ: 3C279 (left) and PKS 0528+134 (right). These plots cover frequencies in the UV through gamma-ray bands. The contributing components are labelled in the legend. **Top panels:** The maximum degree of polarisation. **Bottom panels:** The SED.

1.3 Outline

A few selected previously conducted related work, the problem statement and the research goal will now be given towards the subject of this dissertation.

1.3.1 Previously Conducted Related Work

Smith et al. (1986) found through polarimetric (near-infrared and optical) and photometric monitoring of 4C345 that it always showed a higher degree of polarisation towards shorter optical frequencies. The source had a higher degree of polarisation in its flare state compared to its quiescent state. They used a model that consisted of a power law synchrotron component and black body component (for the optically thick thermal accretion disc) to show how the thermal component diluted the polarised light. Their black body component was found to be at temperatures of $13\,000 - 20\,000$ K and they concluded that it is not well constrained since it might have a higher temperature because they did not include wavelengths shorter than 2260 Å (in the rest frame).

Ghisellini et al. (2010) modelled the SEDs of blazars of known redshifts with a Leptonic model and implemented the SS accretion disc model (Ghisellini and Tavecchio, 2009; Shakura and Sunyaev, 1973). The dust torus component was also taken into account. Ghisellini et al. (2011) studied the SEDs of 19 blazars (FSRQs) that are at redshifts $z > 2$ and it was estimated that almost all blazars in their sample (including 4C+01.02) have BH masses $\sim 10^9$ M$\odot$. For the source 4C+01.02, their model obtained its BH mass as 5×10^9 $M_\odot$ (Ghisellini et al., 2010). In this dissertation this source will be modelled by not only taking its SED into account, but also its spectropolarimetry to estimate the mass of its BH. Most of the work on quasars are not taking the spectropolarimetry into account. Spectropolarimetry holds additional information that is important to our understanding of quasars.

Barres de Almeida et al. (2014) used optical polarisation observations to model the SEDs of blazars. Their method was able to simultaneously describe the SED and variability of the source PKS2155-304. A simultaneous fit of the multiwavelength spectrum, variability and polarisation was conducted by Zhang et al. (2015), for a flare of 3C279.

Constraining the BH mass will be an important result in this dissertation. Other techniques that I will briefly mention, include firstly, reverberation mapping that can estimate the size of the BLR and the mass of the BH. With this, Park et al. (2017) estimated the BH masses in the range $10^{6.5} - 10^{7.5}$ $M_\odot$ for six reverberation-mapped AGN at redshift $z = 0.005 - 0.028$. Secondly, Shen et al. (2011) compiled a catalogue of the properties of 105 783 quasars by using the emission lines Hα, Hβ, Mg II and C IV to produce continuum and emission line measurements to compile virial BH mass estimates.

1.3.2 Problem statement

When modelling the SED of an AGN there are uncertainties in its physical parameters, such as the characteristic energies γ_1, γ_b, and γ_c in the emission region, the spectral indices, the ordering of the magnetic field, the magnetic field strength, the BH mass and the size and

location of the emission region. This is due to the absence of polarisation data (for example in the UV and X-ray band) and variability data (observations of a source in a specific EM band over a period of time that will show variability). More observations and information need to be included that will enable these parameters to be better constrained.

The following questions will be explored in this dissertation: What are the electron distribution parameters? Does the degree of ordering of the magnetic field decrease from the flare to the quiescent state? How well are the flare and quiescent states fitted, by knowing that in both these states the BH mass should be the same? What is the disc luminosity in these two states and can they be interpreted as expected, that is the flare will have a higher disc luminosity than the quiescent state? How does this model compare to previous models?

1.3.3 Research Goal

In this dissertation we focus on producing a Python coded model to fit the radio through optical/UV SED and frequency-dependent degree of polarisation within the optical spectrum of a nonthermal FSRQ jet and its thermal accretion disc. The model will be fitted to the SED and spectropolarimety data of the FSRQ 4C+01.02. With this, the relationship between the SED and polarisation of AGN can be studied and the unpolarised accretion disc contribution can be constrained in the optical/UV spectrum. From the code the following parameters can be determined: the BH mass, disc luminosity, degree of ordering of the magnetic field, electron distribution energies and spectral indices.

The content of this dissertation follows as:
In **Chapter 2** the SED and polarisation model is presented. **Chapter 3** describes the observations and what processing has been done to obtain the data that is used to fit the model. The results are given in **Chapter 4** and they are discussed in **Chapter 5**. The summary and conclusions are given in **Chapter 6**. Future work is discussed in **Chapter 7**. Lastly, the contributors to this project are acknowledged.

Chapter 2

Spectral Energy Distribution and Polarisation Model

We present a code that simultaneously fits the low-frequency component of the SED and the optical degree of polarisation of FSRQs. The model calculates the synchrotron SED and polarisation components from a broken power-law, exponential cut-off electron distribution. The unpolarised SS accretion disc flux is then added to the SED along with the most prominent emission lines from the BLR. The model is fitted to the observations of the source 4C+01.02 ($z = 2.1$) for which the Lyα and C IV lines are most prominent. In the optical/UV band, the total degree of polarisation as a function of frequency can be calculated assuming that the accretion disc flux and BLR emission lines are unpolarised.

Within this chapter the input parameters are first defined and thereafter there is a section describing and testing the code for the SED components and the synchrotron polarisation without implementing a fit. Lastly, the main code is described.

2.1 Input Parameters

For our studied source, the FSRQ 4C+01.02, the values of the input parameters follow as:

- z — The redshift for 4C+01.02 is given by *NED results for object 4C +01.02* (2018) as $z = 2.1$.
- d_L — The luminosity distance to 4C+01.02 is $d_L = 4.952 \times 10^{28}$ cm.
- δ — The Doppler factor is taken as $\delta = 10$.
- R_{in} — The innermost stable orbit for a non-rotating BH is $R_{in} = 3R_s$ (Shakura and Sunyaev, 1973).
- R_{out} — The outer radius boundary of the accretion disc which is assumed to be $R_{out} = 10^3 R_s$. At a radius this far out from the BH, there is a negligible contribution to the optical/UV emission beyond this radius.
- ϵ — The efficiency of converting potential energy into radiation is assumed to be $\epsilon = 1/12$.

- B — The magnetic field is assumed as $B \sim 0.3$ G.

The electron distribution at the characteristic Lorentz factor energies $\gamma_{min},\ \gamma_b$ and γ_c in the emission frame where calculated from the observed characteristic synchrotron frequencies, by using the relationship $\nu_{obs}^{sy} = \nu_0 \gamma_{em}^2 \cdot \delta/(z+1)$, as was described in section 1.2. Log-spaced range interpolations are used throughout the code.

By only including the synchrotron component of the nonthermal radiation during the model fit, there are degeneracies in the electron distribution energies γ's and the magnetic field B. These parameters can be more accurately constrained by including the Compton scattering components in the fit.

2.2 Initialisation and Code tests of Electron Distribution, Flux Components and Synchrotron Polarisation

In this section the electron distribution, flux components and synchrotron polarisation are calculated, separately. Tests are done without taking cosmological redshift and Doppler boosting effects into account. They are taken into account in the main code.

The electron distribution is calculated as a broken power law with an exponential cut-off spectrum, as given by equation (1.1), and the result is shown in the upper left plot of Figure 2.1.

The accretion disc flux is calculated using equation (1.30) by implementing the midpoint-integration technique (see Appendix B) to integrate over the disc radius. This technique is also implemented for the integrations over the Lorentz factor energies γ for the synchrotron flux, given by equation (1.55) and the synchrotron polarisation, given by

$$\Pi_{\omega}^{sy} = F_B \frac{\int N_e(\gamma) x(\gamma) K_{2/3}(x(\gamma)) d\gamma}{\int N_e(\gamma) x(\gamma) \int_{x(\gamma)}^{\infty} K_{5/3}(x(\xi)) d\xi d\gamma}, \tag{2.1}$$

when equations (1.71) and (1.72) are substituted into equation (1.70). The resulting accretion disc and synchrotron radiation spectra are shown in the upper right and lower left plots of Figure 2.1, respectively. The plot of the synchrotron radiation spectrum is in agreement with equation (1.56) by following the relationships: $\nu F_\nu \propto \nu^{4/3}$ for $\nu < \nu_{min}$, $\nu F_\nu \propto \nu^{1/2}$ for $p = 2$, where $\nu_{min} < \nu < \nu_b$ and $\nu F_\nu \propto \nu^{0.05} \cdot e^{-\nu/\nu_c}$ for $p = 2.9,$ where $\nu_b < \nu < \nu_c$.

For the synchrotron polarisation described by equation (1.70), the polarisation is divided by the F_B factor and plotted as function of ν in the right lower plot of Figure 2.1. The Bessel functions $K_{2/3}$ and $K_{5/3}$ are calculated using the inbuilt python Bessel function *mpmath.besselk()*, where *mpmath* is the python package. The upper limit of the Bessel function $\int_x^\infty K_{5/3}(\xi) d\xi$ requires an integration to infinity. In the program this was achieved using the midpoint integration technique, and a DO LOOP stepping through logarithmically increasing values until the term $\int_x^\infty K_{5/3}(\xi) d\xi$ gives insignificantly small values and then the loop is exited. In Figure 2.1 (lower right) it can be seen that $\Pi_{max}^{sy}(p_1 = 2)/F_B = 0.69$ and

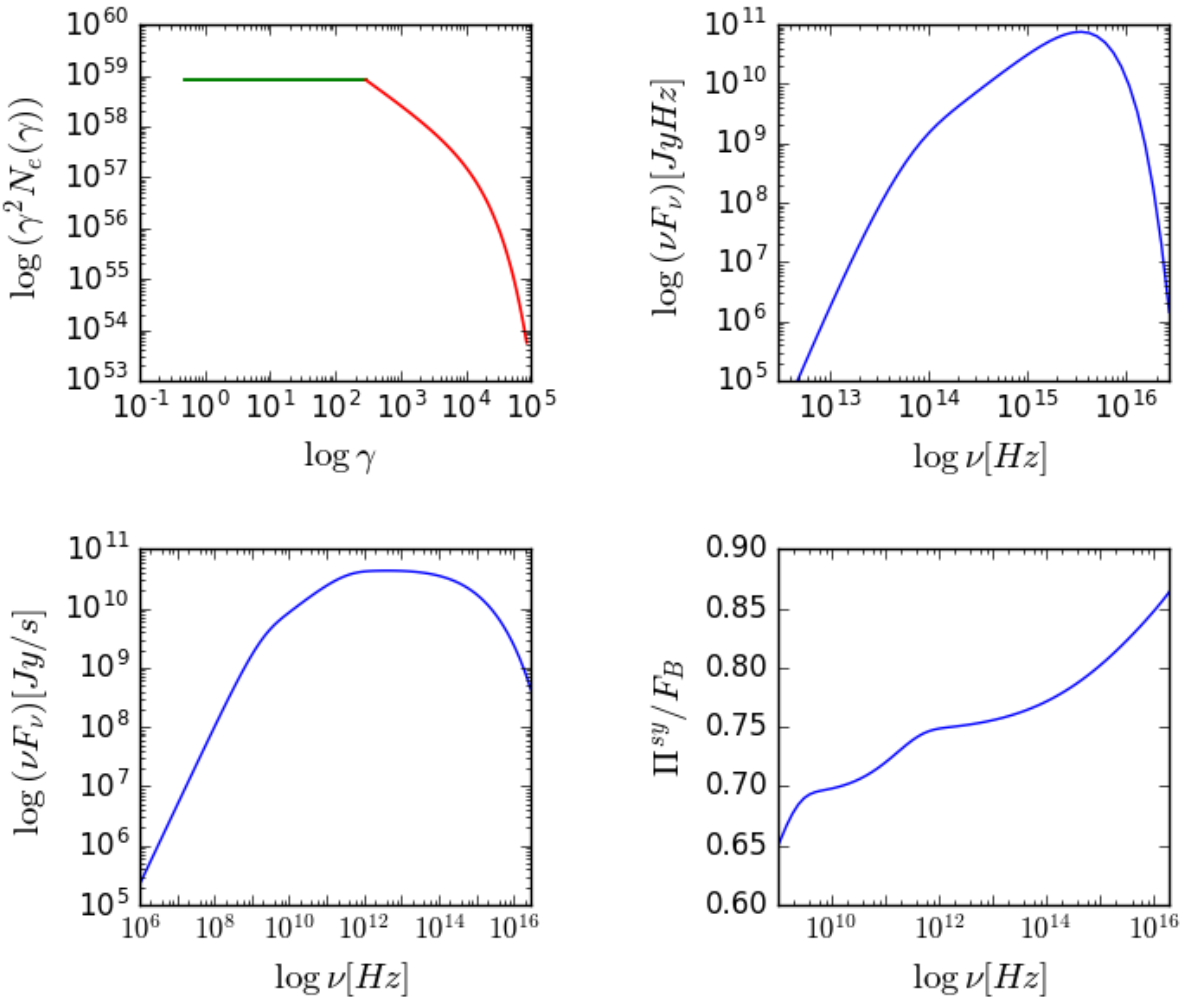

Figure 2.1: Model components. An electron distribution (**upper left**) of $n_0 = 1 \times 10^{54}$ electrons is defined by a broken power law energy distribution with spectral indices $p_1 = 2$ and $p_2 = 2.9$, and Lorentz factors $\gamma_b = 2.899 \times 10^2$ and $\gamma_c = 1.242 \times 10^4$ that are calculated from the synchrotron flux cut-off frequencies with the $\nu = \nu_0\gamma^2$ relation, yielding the break frequency $\nu_b = 6.48 \times 10^{11}$ Hz and the cut-off frequency $\nu_c = 8.19 \times 10^{14}$ Hz. The accretion disc flux (**upper right**) for the mass of a BH $M_{BH} = 10^9$ $M_\odot$, disc luminosity $L_d = 10^{46}$ erg $\cdot$ s^{-1} and the distance to the source $d = 4.952 \times 10^{28}$ cm. The synchrotron flux (**lower left**) and synchrotron polarisation (**lower right**) from this given electron distribution, with the ordering of the magnetic field $F_B = 1$.

$\Pi^{sy}_{max}(p_2 = 2.9)/F_B = 0.75$ correspond to the zero slopes of the plot, in agreement with equation (1.73).

2.3 Main Code: The Simultaneous SED and Polarisation Fit

In this section the main code will be described. Two fits are simultaneously conducted: (1) the total flux function is fitted to the low-frequency SED data, and (2) the total polarisation degree function is fitted to the optical degree of polarisation data. The fit is done by using the fit function `curve_fit()` from the python scipy.optimize package, to find the parameters agreeing with both the SED and degree of polarisation observations. Our model is dependent on the following components: the synchrotron flux `nuF_sy()`, the accretion disc flux `nuF_d()`, the synchrotron polarisation `SyPolDeg()` and the flux of the lines `Fnu_line()`. The contribution of the most prominent emission lines Lyα and C IV is calculated by using the Gaussian (equation 1.31). The free parameters h_1 and h_2, are used to determine the heights of the emission lines. The flux of the emission lines is not included in the total flux function, since it is negligible during the total flux fit. The first argument in the functions is the frequency `nu`, with the other entries the free parameters. The free parameters are: the number of electrons n_0, the characteristic energies γ_{min}, γ_b and γ_c, the spectral indices p_1 and p_2, the ordering of the magnetic field F_B, the BH mass M_{BH}, the accretion disc luminosity L_d and the emission line parameters h_1 and h_2. In the code they are written as `n0, gamma_1, gamma_b, gamma_c, p1, p2, F_B, Mbh, Ld, h1` and `h2`, respectively.

```
def nuF_total(nu, n0, p1, p2, gamma_1, gamma_b, gamma_c, Mbh, Ld):
    return nuF_sy(nu, n0, p1, p2, gamma_1, gamma_b, gamma_c) + nuF_d(nu, Mbh,
   Ld)
```

Code Excerpt 2.1: Python Code – The total flux `nuF_total()` is defined as a function of frequency `nu` and free parameters. It is calculated as the sum of the synchrotron flux function `nuF_sy()` and accretion disc flux function `nuF_d()`.

```
def TOTAL_POL_DEGREE(nu, n0, p1, p2, gamma_1, gamma_b, gamma_c, F_B,
  Mbh, Ld, h1, h2):
    return SyPolDeg(nu, p1, p2, gamma_1, gamma_b, gamma_c, F_B)*nuF_sy(nu, n0,
    p1, p2, gamma_1, gamma_b, gamma_c)/(nuF_sy(nu, n0, p1, p2, gamma_1, gamma_b
    , gamma_c) + nuF_d(nu,Mbh,Ld)+nuF_line(nu, n0, p1, p2, gamma_1, gamma_b,
    gamma_c, h1, h2))
```

Code Excerpt 2.2: Python Code – The total optical degree of polarisation `TOTAL_POL_DEGREE()` (equation 1.74) is a function of the synchrotron polarisation degree `SyPolDeg()`, the synchrotron flux `nuF_sy()`, the accretion disc flux `nuF_d()` and the flux of the lines `nuF_line()`.

Since the data obtained are in the observer's frame, the accretion disc flux and emission lines flux are redshifted to the observer's frame using equation (1.3). The synchrotron flux and polarisation are redshifted and Doppler-shifted using equation (1.4) to the observer's frame. The redshift and Doppler-shift (in the case of calculating the synchrotron flux) are coded into the flux component functions: `nuF_d()`, `nuF_line()` and `nuF_sy()`.

The following code excerpt 2.3 shows the code that does the simultaneous fit, adapted from *Simultaneous data fitting in python with leastsq* (2014):

```
1  def simul_fit(curvefit_xdata, n0, p1, p2, gamma_1, gamma_b, gamma_c, F_B, Mbh,
       Ld, h1, h2):
2      x1 = curvefit_xdata[0]
3      x2 = curvefit_xdata[1]
4      fit1 = nuF_total(x1, n0, p1, p2, gamma_1, gamma_b, gamma_c, Mbh, Ld)
5      fit2 = TOTAL_POL_DEGREE(x2, n0, p1, p2, gamma_1, gamma_b, gamma_c, F_B, Mbh
       , Ld, h1, h2)
6      return numpy.concatenate((fit1, fit2))
7  curvefit_xdata = numpy.concatenate([[x1,x2]])
8  curvefit_ydata = numpy.concatenate([y1,y2])
9  popt = curve_fit(simul_fit,curvefit_xdata, curvefit_ydata, p0,
10 bounds = ([n0_lower, ps_lower, ps_lower, gamma1_lower, gammab_lower,
       gammac_lower, FB_lower, Mbh_lower, Ld_lower, h1_lower, h2_lower],
11 [n0_upper, ps_upper, ps_upper, gamma1_upper, gammab_upper, gammac_upper,
       FB_upper, Mbh_upper, Ld_upper, h1_upper, h2_upper]))
```

Code Excerpt 2.3: Python Code – Simultaneous Fit.

In the function `simul_fit()` the model functions (Code Excerpts 2.1 and 2.2) are assigned, which will be used to calculate the residual between the model and the data in the `curve_fit()` function. (`x1`, `y1`) contains the archival and photometry flux data. (`x2`, `y2`) contains the optical degree of polarisation data from the SALT spectropolarimetry observations. These observations will be described in Chapter 3. Since we desire the `curve_fit()` function to calculate the parameters of both of these functions simultaneously, the two functions `fit1` and `fit2` are concatenated together. This means that the output array of the first function is followed by the output array of the second function. The `curve_fit()` function also has one input for x-data and one for y-data. The `x1` and `x2` arrays are therefore concatenated together as `curvefit_xdata`, inserted as the x-data and split again within the `simul_fit` function. The same procedure is followed for `y1` and `y2`.

The `curve_fit()` built-in scipy fitting function is called in line 9. The input arguments for this function follow as our defined `simul_fit()` function, the arguments that are the SED and degree of polarisation data, the initial array of estimate parameters that guides the fit that is given by a `p0` array and `bounds` that contains two arrays, one for the lower boundaries of the parameters and the second for the upper boundaries. The returned output `popt` holds the obtained parameters. When the free parameters are constrained, the maximum disc temperature can be calculated with equation (1.18).

Chapter 3

Observations

Studying the physics of AGN has rapidly developed in the past few years due to better observational instruments. By observing blazars, their structure, continuum spectrum, and polarisation variations can be studied.

A general introduction is given about the multiwavelength observations. We then focus in on the observatories that contributed to collecting the data of our studied source. The main analysis procedures are given for data contributed by collaborators within this project.

3.1 Multiwavelength Observations

Figure 3.1 shows an illustration of observatories at the different regimes in the EM spectrum. A wave illustrates the EM spectrum with increasing wavelength from the gamma-ray band to the radio band. Some detectors must be placed in orbit above Earth since the atmosphere is only transparent to optical and radio wavelengths.

Observations within this project are conducted in collaboration with the Southern African Large Telescope (SALT) Large Program (PI: David Buckley, from the South African Astronomical Observatory (SAAO)) (Böttcher et al., 2017). This program entails Target of Opportunity (ToO) spectroscopy and spectropolarimetry observations of transient objects such as X-ray binaries, cataclysmic variables, tidal disruption events, gamma-ray bursts, novae, microlensing events and blazars. Table 3.1 lists the blazars for which spectropolarimetry observations have been obtained. The programme continues and more observations have been obtained. The preliminary polarisation degrees are shown within the last column of this table. When the Fermi Large Area Telescope (Fermi-LAT) detects a flare, SALT Large Program ToO observations are triggered. When possible, optical photometry data from Las Cumbres Observatory (LCO) and X-ray data from Neil Gehrels Swift Observatory (Swift) are obtained for the same flare. The observations discussed below are for the FSRQ 4C+01.02 (also known as PKS B0106+013). Additional archival data for radio-, microwave-, visible- and UV band observations are taken from *NED results for object 4C +01.02* (2018).

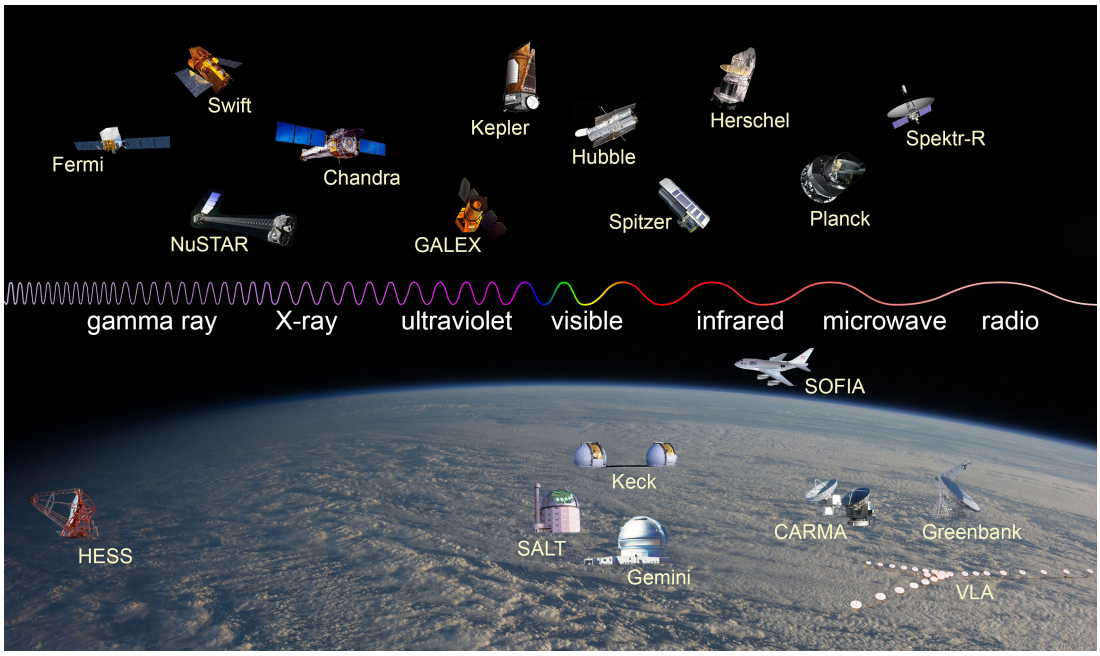

Figure 3.1: Spacecraft and telescopes (operational in February 2013) observing at different wavelengths across the EM spectrum. This illustration is not complete in showing all the existing observatories. Illustration credit: Observatory images from NASA, ESA (Herschel and Planck), Lavochkin Association (Specktr-R), HESS Collaboration (HESS), Salt Foundation (SALT), Rick Peterson/WMKO (Keck), Germini Observatory/AURA (Gemini), CARMA team (CARMA), and NRAO/AUI (Greenbank and VLA); background image from NASA.

3.1.1 SALT – Spectropolarimetry

SALT is one of the largest optical telescopes in the world with a hexagonal primary mirror array with a diameter of 11 metres, consisting of ninety-one 1 m hexagonal mirrors (Crawford et al., 2012). It is located at the SAAO field station, near Sutherland in South Africa.

One of the main instruments of the telescope - the Robert Stobie Spectrograph (RSS) - can perform spectroscopy (the study of spectra) in the wavelength range 3200Å−9000Å (Kobulnicky et al., 2003). The RSS has spectropolarimetry capabilities which allows for polarimetry measurements of near-infrared and optical waves. Figure 3.2 shows the spectropolarimetry observations for five observation windows, that is for 9 July 2016; 27, 28 and 29 November 2016 and 25 July 2017. A flare is observed on 9 July 2016 and a low polarisation state is observed on 25 July 2017. Our model will interpret and distinguish these two (high and low) states from one another. The top panel shows the RSS count spectra for the different observations. The first dominant peak (from the left) is the Lyα line and the second dominant peak is the C IV line. The fifth dashed line is a telluric absorption line. The second panel shows the degree of polarisation where there is a decrease in polarisation towards lower wavelengths/higher frequencies. This indicates that there should be an unpolarised component, that is, the accretion disc. The bottom panel shows the equatorial polarisation angle. Our model is not dependent on the polarisation angle. The spectropolarimetry was taken with the RSS in “LINEAR”-mode (Crawford et al., 2012). These observations were

Blazar	Type	Redshift	Obs. dates	Grating	Waveplate pattern	Exposure	% polarisation
PKS 2023-07	FSRQ	z = 1.4	15 Apr 2016	PG 300	LINEAR-HI	2400 s	25–27
PKS 1510-089	FSRQ	z = 0.36	01 Jun 2016	PG 300	LINEAR-HI	2400 s	1–2
4C +01.02	FSRQ	z = 2.10	08 Jul 2016	PG 300	LINEAR	2400 s	9–11
			27 Nov 2016	PG 300	LINEAR	2400 s	∼6
			28 Nov 2016	PG 300	LINEAR	2400 s	8–10
			29 Nov 2016	PG 300	LINEAR	2400 s	8–10
PKS 0524-485	FSRQ	z = 1.3	23 Oct 2016	PG 900	only spectrum	800 s	NA
PKS 0907-023	FSRQ	z = 0.96	19 Jan 2017	PG 300	LINEAR	2400 s	0–4
PKS 0426-380	BLL	z = 1.11	21 Jan 2017	PG 300	LINEAR	2400 s	10–11
			20 Feb 2017	PG 300	LINEAR	2400 s	11–12
PKS 0447-439	BLL	z = 0.10	21 Feb 2017	PG 900	LINEAR	480 s	5–6
3C 279	FSRQ	z = 0.54	28 Mar 2017	PG 900	LINEAR	480 s	12–14
			31 Mar 2017	PG 900	LINEAR	480 s	8–10
			17 May 2017	PG 300/900	LINEAR	720 s/720 s	∼21/-
			21 May 2017	PG 300	LINEAR	1200 s	20–22
3C 273	FSRQ	z = 0.17	13 Jun 2017	PG 300	LINEAR-HI	160 s	<1
			14 Jun 2017	PG 300	LINEAR-HI	160 s	<1
NVSS J141922-083830	FSRQ	z = 0.903	02 Jun 2017	PG 300	only spectrum	2400 s	NA
4C +01.02	FSRQ	z = 2.10	24 Jul 2017	PG 300	LINEAR	2400 s	0.5–3
TXS 0506+056	BLL	z = 0.34	28 Sep 2017	HRS	Low Res	2500 s	NA
(IC-EHE)			14 Oct 2017	PG 900	LINEAR	2400 s	-
			20 Oct 2017	PG 900	LINEAR	2400 s	-
PKS 0131-522	FSRQ	z = 0.92	19 Nov 2017	PG 300	LINEAR	3200 s	7–10
			22 Nov 2017	PG 300	LINEAR	3188 s	5–8
PKS 0346-279	FSRQ	z = 0.99	09 Feb 2018	PG 300	LINEAR	2000 s	18–19
PKS 0903-57	BCU	z = 0.70	16 May 2018	PG 300	LINEAR	3200 s	6–15
3C 279	FSRQ	z = 0.54	05 Jun 2018	PG 300	LINEAR	1600 s	17–19
PKS 0035-252	FSRQ	z = 0.50	20 Jul 2018	PG 300	LINEAR	2500 s	∼7
PKS 2023-07	FSRQ	z = 1.4	04 Oct 2018	PG 300	LINEAR-HI	2400 s	∼9
TXS 0646-176	FSRQ	z = 1.23	07 Nov 2018	PG 300	LINEAR	2400 s	∼18
PKS 0035-252	FSRQ	z = 0.50	11 Nov 2018	PG 300	LINEAR	2500 s	∼5

Table 3.1: SALT Large Program ToO spectropolarimetry observations for flaring blazars. Last modified: 13 November 2018.

conducted with an exposure time of 600 s for each of the orientations of the half wave plates ($0°, 45°, 22.5°$ and $67.5°$) (Böttcher et al., 2017). Data was reduced with the POLSALT reduction pipeline (*Polarimetric reductions for SALT*, 2019).

3.1.2 LCO – Optical Photometry

In the optical spectrum the brightness of the source can be measured in different bands by using different filters. Measuring the brightness of a source is called *photometry*. The brightness of a source is measured in *magnitudes*. *Differential photometry* is the process in which the magnitude of a target source is evaluated by comparing its photon count rates to those of a source that is non-variable and (preferably) of the same spectral type as the target. Differential photometry corrects for atmospheric effects and the change in magnitude of the target source to be determined. The magnitude of the target source can also be found when there is a source with a calibrated magnitude in its field of view, that is, when the two sources are observed through the same changing atmosphere.

The Las Cumbres Observatory (LCO) is a global network of telescopes which contributes to continuous observations over several days. SAAO, near Sutherland, is part of the LCO

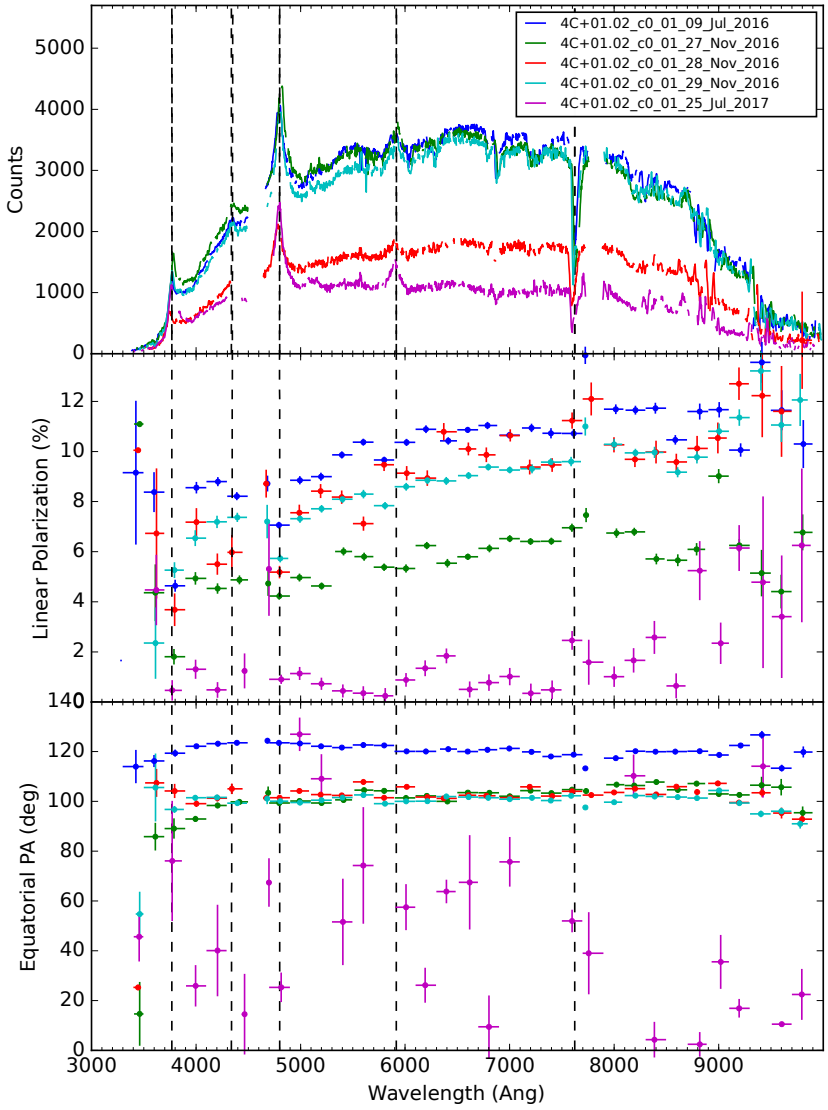

Figure 3.2: SALT observations of 4C+01.02 for five observation windows: the flare state in 9 July 2016 is shown in dark blue, 27 November 2016 is shown in green, 28 November 2016 is shown in red, 29 November 2016 is shown in cyan blue and the quiescent state in 25 July 2017 is shown in purple. Dashed lines indicate the following emission lines in the emission frame from left to right: Lyα 1216Å, Si IV 1400Å, C IV 1549 Å, C III 1909 Å (in this plot, they are plotted in the observed frame). The last line is a telluric absorption line. **Top panel:** The SALT-RSS count spectra. **Middle panel:** The linear polarisation percentage at different wavelengths. **Bottom panel:** The Equatorial polarisation angle for these different wavelenghts. These are produced by Brian van Soelen and Richard J. Britto (UFS, SALT)

network and collaborators from the UFS contributed to the photometry data within our project. So far, the LCO has a network of eighteen telescopes but, after its construction is complete there will be two 2 m Faulkes telescopes, seventeen 1 m telescopes and twenty-three 40 cm telescopes world wide (Brown et al., 2013). This observatory can perform observations in the near-infrared and optical bands.

Photometric observations were conducted with the 1m class telescope along with the Santa Barbara Instrument Group (SBIG) CCD. Data reduction was performed using the IRAF/NOAO packages (Böttcher et al., 2017). The magnitudes of four comparison stars were used to perform differential photometry. These magnitudes were taken from the NOMAD catalog. For the flare state of the source in 2016, contemporaneous photometric data points were observed on 2 August 2016 and reduced by Johannes P. Marais and for the quiescent state in 2017 the contemporaneous photometry magnitudes were observed on 27 October 2017 and reduced by Brian van Soelen.

3.1.2.1 Converting Photometric Magnitudes to Fluxes

A python code was programmed to do a magnitude to νF_ν flux conversion. This conversion is explained by applying the following procedure on the photometric observations for the quiescent state of 4C+01.02 on 27 Oct 2017:

The apparent Johnson photometry magnitudes in the B-, V- and R filters in the optical band and the I filter in the near-infrared band, their magnitude errors, the extinction coefficient and the zero-point flux normalisation for each filter are listed in Table 3.2.

Filter	**Frequency** ν $[\times 10^{14}$ Hz]	F_0 [Jy]	A_λ	**Magnitude**	**Magnitude Error**
B	6.849	4063	0.088	18.489	0.109
V	5.505	3636	0.066	18.375	0.062
R	4.680	3064	0.053	18.145	0.092
I	3.759	2416	0.036	17.457	0.122

Table 3.2: Input values for converting photometry magnitudes to fluxes. The third column gives the zero-point flux (Bessell et al., 1998) and the forth the extinction coefficient (*NED results for object 4C +01.02*, 2018). The last two columns give the B-, V-, R- and I-magnitudes and their errors obtained with LCO for 4C+01.02 on 27 Oct 2017 (produced by Brian van Soelen).

The flux νF_ν in units of $[10^{-23} \cdot \mathrm{erg} \cdot \mathrm{cm}^{-2} \cdot \mathrm{s}^{-1} \cdot \mathrm{Hz}^{-1}]$ is calculated as

$$\nu F_\nu = \nu F_0 \times 10^{(A_\lambda - m)/2.5} \tag{3.1}$$

where m is the magnitude, F_ν is the flux at frequency ν, A_λ is the interstellar extinction coefficient and F_0 is the zero-point flux normalisation (zero point of the magnitude scale). The magnitude error is added and subtracted from the magnitude value to calculate the upper limit and lower limit magnitude for each filter, respectively. By substituting the resulting

magnitudes in equation (3.1) the νF_ν upper and lower limits are obtained. The results are shown in Table 3.3.

Filter	**Frequency** ν $[\times 10^{14}$ Hz]	**Flux** νF_ν $[\times 10^{10}$ Jy $\cdot$ Hz]	**Flux Error** νF_ν^{err} $[\times 10^{10}$ Jy $\cdot$ Hz]
B	6.849	12.139	1.277
V	5.505	9.500	0.553
R	4.680	8.311	0.738
I	3.759	9.769	1.163

Table 3.3: Photometry points to flux conversion results: νF_ν versus ν.

3.1.3 Swift – X-rays

The X-ray spectrum was observed by Swift, which is a spacecraft that carries three instruments: an X-ray Telescope (XRT) (covering an energy range of $0.2-10$ keV) which obtained our data, but it also has an UV/Optical Telescope (UVOT) (covering a wavelength range of $170-600$ nm) and a Burst Alert Telescope (BAT) which is an all-sky monitor for the primary purpose of detecting gamma-ray bursts and other soft gamma-ray transients (covering an energy range of $15-160$ keV) (Barthelmy et al., 2005; Burrows et al., 2005; Roming et al., 2005).

The X-ray spectrum for the flare state used in our model is the archival data from the summed observations from 2007 to 2008 (Ghisellini et al., 2011), since these correspond to the flare/elevated gamma-ray flux state (Böttcher et al., 2017). Abe Falcone and Amanpreet Kaur performed the data reduction for the quiescent state that was observed on 2 August 2017. A χ^2-analysis was performed to obtain the corresponding spectral index for a fixed column density N_H. Their results are given in Table 3.4.

3.1.3.1 Converting XRT-data from Spectral Index and Unabsorbed Flux

In this section the analysis to obtain the X-ray SED fluxes for the quiescent state of 4C+01.02 is described using the information from Table 3.4 and the results are shown in Figure 3.3. The physical meaning of these results will be described.

X-rays propagate through a column of gas from the source to the observer. In the analysis the density was fixed to the Galactic hydrogen density. An X-ray photon will interact with an electron in the atom of this gas to remove the electron from its shell, with the incident X-ray photon being completely absorbed. This is called the *photoelectric effect* and can take place when the photon has an energy equal to or higher than the binding energy of the electron in its shell. The spectrum we receive is therefore going to be different than the intrinsic spectrum before absorption.

	Value
Unabsorbed flux $F_{0.45\text{ keV}-6\text{ keV}}$	1.19×10^{-12} $\left[\frac{\text{erg}}{\text{cm}^2 \cdot \text{s}}\right]$
ϵ_0	0.45
ϵ_1	6
Spectral index Γ	1.43
Spectral index error Γ_{err}	0.23

Table 3.4: Swift observations for 4C+01.02 on 2 August 2017 for fixed $N_H = 2.42 \cdot 10^{20}$ cm^{-2}, produced by Abe Falcone and Amanpreet Kaur.

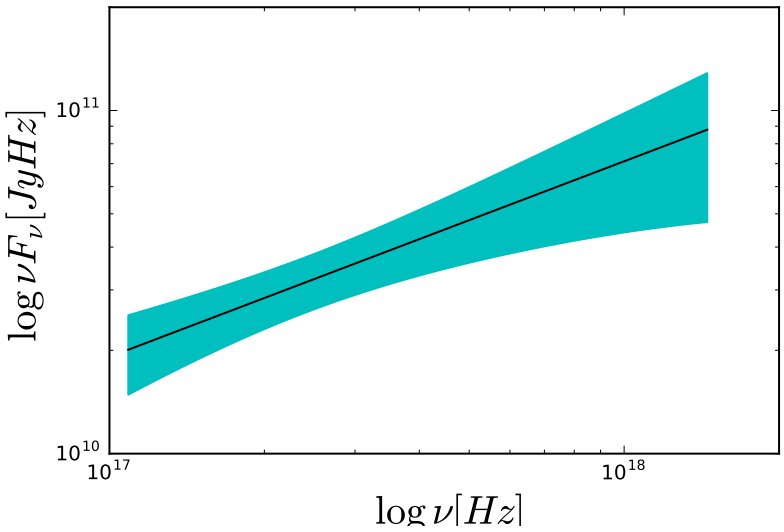

Figure 3.3: Results of the XRT-data analysis python code by interpolating the range of energies into 100 points. The black line indicates the νF_ν fluxes and the cyan filled in area gives the uncertainty area of these fluxes.

The total unabsorbed photon flux F (that is the flux the source emitted and that was corrected for the absorption) will be equal to the integration of the flux F_E as a function of photon energy E, integrated over the entire energy range (E_0, E_1), that is

$$F = \int_{E_0}^{E_1} F_E dE. \tag{3.2}$$

The flux at a specific energy is given by

$$F_E = \phi_E E \tag{3.3}$$

where ϕ_E is the photon number flux

$$\phi_E = \phi_1 \epsilon^{-\Gamma} \left[\frac{\text{ph}}{\text{cm}^2 \cdot \text{s} \cdot \text{keV}}\right] \tag{3.4}$$

with ϕ_1 being the normalisation parameter, ϵ the energy per 1 keV and Γ the spectral index. The units are indicated in the square brackets. Substituting equation (3.4) into equation (3.3)

and then substituting this result into equation (3.2) yields

$$F = \int_{E_0}^{E_1} \phi_1 E \epsilon^{-\Gamma} dE. \tag{3.5}$$

Solving for F with the energy of a photon $E = \epsilon \cdot (1 \text{ keV})$ and $dE = d\epsilon \cdot (1 \text{ keV})$, gives

$$\begin{aligned} F &= \phi_1 \int_{E_0}^{E_1} (\epsilon \cdot 1 \text{ keV}) \epsilon^{-\Gamma} (d\epsilon \cdot 1 \text{ keV}) \left[\frac{1}{\text{cm}^2 \cdot \text{s} \cdot \text{keV}}\right] \\ &= \phi_1 \int_{\epsilon_0}^{\epsilon_1} \epsilon^{1-\Gamma} d\epsilon \left[\frac{\text{keV}^2}{\text{cm}^2 \cdot \text{s} \cdot \text{keV}}\right] \\ &= \frac{\phi_1}{2-\Gamma} [\epsilon^{2-\Gamma}]_{\epsilon_0}^{\epsilon_1} \left[\frac{\text{keV}}{\text{cm}^2 \cdot \text{s}}\right]. \end{aligned} \tag{3.6}$$

Rewriting the result in terms of ϕ_1 yields

$$\phi_1 = \frac{(2-\Gamma) F (\text{keV})^{-2}}{(\epsilon_1^{2-\Gamma} - \epsilon_0^{2-\Gamma})} \ . \tag{3.7}$$

The frequency times the flux can then be calculated as

$$\nu F_\nu = \phi_1 \epsilon^{2-\Gamma} \ . \tag{3.8}$$

To write ϵ in terms of frequency, thereby converting keV to Hz:

$$\begin{aligned} 1 \text{ keV} &= 1.602 \times 10^{-9} \text{ erg} \\ \text{Planck's constant } h &= 6.626 \times 10^{-27} \text{ erg} \cdot \text{s} \\ => \frac{1 \text{ keV}}{h} \left[\frac{\text{keV}}{\text{erg} \cdot \text{s}}\right] &= 2.418 \times 10^{17} \text{ Hz} \end{aligned} \tag{3.9}$$

so that

$$\epsilon = \frac{E}{1 \text{ keV}} = \frac{h\nu}{1 \text{ keV}} = \frac{\nu}{2.418 \times 10^{17} \text{ Hz}} \tag{3.10}$$

$$\nu = \epsilon \, (2.418 \times 10^{17} \text{ Hz}) \, . \tag{3.11}$$

This implies that

$$\nu F_\nu = \phi_1 \left(\frac{\nu}{2.418 \times 10^{17} \text{ Hz}}\right)^{2-\Gamma} (\text{keV})^2 \tag{3.12}$$

with

$$\phi_1 = (2-\Gamma) \text{F} \left[\left(\frac{\nu_1}{2.418 \times 10^{17} \text{ Hz}}\right)^{2-\Gamma} - \left(\frac{\nu_0}{2.418 \times 10^{17} \text{ Hz}}\right)^{2-\Gamma}\right]^{-1} (\text{keV})^{-2}. \tag{3.13}$$

The analysis then follows as:

1. The frequency range can be calculated with equation (3.11) and the lower and upper limits of ϵ that are given in the table. Calculate the upper and lower limits of Γ by adding and subtracting the error from the Γ-value, that is

$$\Gamma_{min} = \Gamma - \Gamma_{err} \tag{3.14}$$

$$\Gamma_{max} = \Gamma + \Gamma_{err}. \tag{3.15}$$

2. Calculate the normalisation parameter as given by equation (3.13). Also calculate its lower and upper $\phi_{1,\,min}$ and $\phi_{1,\,max}$ with the lower and upper values of the spectral index given by equation (3.14) and equation (3.15), respectively. The error of the normalisation parameter can be calculated as

$$\phi_{1,\,err} = \frac{|\phi_{1,\,max} - \phi_{1,\,min}|}{2}. \tag{3.16}$$

3. Calculate the flux νF_ν at a frequency ν by using equation (3.12). To find the error of the flux, note that $\nu F_{\nu,\,err}$ is dependent on $\phi_{1,\,err}$ and Γ_{err}, where Γ_{err} is an exponent. By setting $f_\Gamma = (\frac{\nu}{2.418\times10^{17}\ \mathrm{Hz}})^{2-\Gamma}$ and evaluating its error

$$f_{min} = \left(\frac{\nu}{2.418\times10^{17}\ \mathrm{Hz}}\right)^{2-\Gamma_{min}} \tag{3.17}$$

$$f_{max} = \left(\frac{\nu}{2.418\times10^{17}\ \mathrm{Hz}}\right)^{2-\Gamma_{max}} \tag{3.18}$$

$$f_{\Gamma,\,err} = \frac{|f_{max} - f_{min}|}{2} \tag{3.19}$$

the flux error can be calculated as

$$\nu F_{\nu,\,err} = \phi_1 \cdot f_\Gamma \sqrt{\left(\frac{\phi_{1,\,err}}{\phi_1}\right)^2 + \left(\frac{f_{\Gamma,\,err}}{f_\Gamma}\right)^2}\,(\mathrm{keV})^2, \tag{3.20}$$

where $\nu F_\nu = \phi_1 \cdot f_\Gamma$.

The results fall within the expected X-ray frequency region within the SED as shown in Figure 3.3.

3.1.4 Fermi-LAT – Gamma-Rays

The Large Area Telescope (LAT) is a scientific instrument on board the Fermi spacecraft, covering an energy range below 20 MeV to > 300 GeV (Atwood et al., 2009). Within the first month of its operation the number of known gamma-ray emitting blazars was doubled, since Fermi has an increased sensitivity by more than a magnitude compared to its predecessor the Energetic Gamma-Ray Experiment Telescope (EGRET) (Abdo et al., 2009; Ghisellini et al., 2010).

The Fermi data for the flare and quiescent states were obtained by Richard J. Britto using Pass 8 Fermi-LAT data (Atwood et al., 2013) in the 100 MeV − 300 GeV range and analysis with the Fermi Science Tools version v10r0p5 (Böttcher et al., 2017). A Region of Interest (ROI)= 50°, source region = ROI +10°, SOURCE class, front and back type event, zenith angle < 90°, DATA_QUAL=1, LAT_CONFIG=1, diffuse emission: gll_iem_v06.fits (Galactic) and ISO_P8R2_SOURCE_V6_v06.txt (extragalactic) templates, were used in the analysis. Lightcurve processing was performed with the unbinned likelihood gtlike/pyLikelihood tool where the source was modelled with a power law spectrum. The SED was processed with the binned likelihood analysis from the *Enrico* Python package.

The lightcurve for 4C+01.02 during its flare state is shown from 11 May to 15 August 2016 in the top panel in Figure 3.4. The large gamma-ray flare can be seen in the 2-20 July period where the flux peaks. This is also the highest observed flux yet detected by Fermi-LAT for this source (Böttcher et al., 2017). For the quiescent state, gamma-ray observations were obtained during the period 3 July-2 August, 2017.

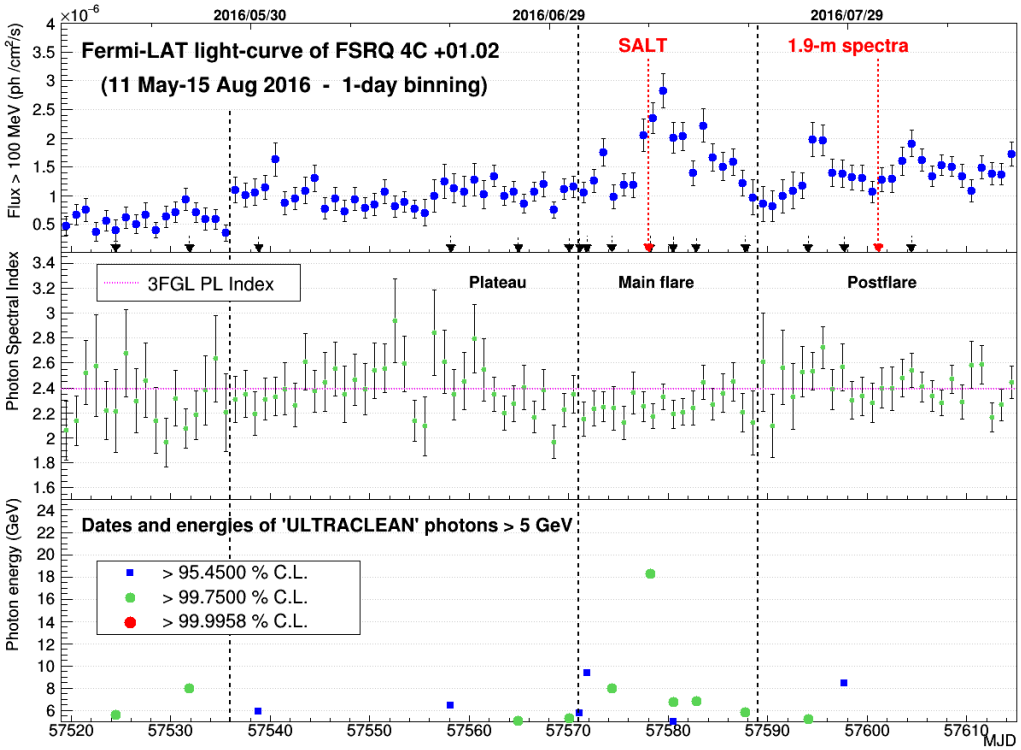

Figure 3.4: **Top panel:** Fermi-LAT lightcurve for 4C+01.02. A plateau, main flare and postflare are indicated between the vertical dashed lines. The main and post flare are also observed by SALT and the South African Astronomical Observatory (SAAO) 1.9m Telescope, respectively. **Middle panel:** The photon spectral index for a single power law is indicated as a function of the Modified Julian Date (MJD), showing a fluctuation around the average spectral index of 2.4 (indicated by the red dotted line). **Bottom panel:** Photon Energy (GeV). Every point indicates one photon received with an energy > 5 GeV. Very few photons are received with such high energies. The different colours indicate the confidence levels that these photons are from the source. This figure is contributed by Richard J. Britto.

Chapter 4

Results

This chapter gives the results of the simultaneous SED and optical degree of polarisation model fitted to the FSRQ 4C+01.02 ($z = 2.1$), in its flare state of 2016 and quiescent state of 2017. The broad-band SED was calculated by applying the parameters found from this model code in the Böttcher et al. (2013) code. To compare the results of the model to previous work that has been done, the BH mass obtained by Ghisellini et al. (2011) was tested.

4.1 Simultaneous Fit Results

The simultaneous fit results obtained by the model are plotted in Figures 4.1 and 4.2.

The SED model components of the flare and quiescent state are shown in the left plots in Figure 4.1. In each of these plots, the synchrotron flux component and accretion disc flux component are fitted to the optical flux and the archival data. The photon spectral indices for the synchrotron spectrum are calculated with $\alpha = (p-1)/2$ (equation 1.2).

On the right side in Figure 4.1 the SED components and degree of polarisation components are plotted in the frequency range 2×10^{14} to 10^{15} Hz to show the optical/UV regime. Prominent emission lines: C IV and Lyα are at 6.6×10^{14} Hz and 7.93×10^{14} Hz, respectively. For the flare, the low total degree of polarisation data point at $\sim 5 \times 10^{14}$ Hz could indicate the non-prominent C III emission line. The line heights h_1 and h_2 values obtained during the flare fit are used in the quiescent state fit, since the BLR does not change significantly from one state to another.

4.2 Broad-band SED

In Figure 4.3 the X-ray and gamma-ray components (EC and SSC components) of the Leptonic model are produced with the Böttcher et al. (2013) code that implements the parameters obtained by the model (Tabel 4.1), that is the radiating electron distribution from the emission region and the magnetic field ordering. The high-frequency component is the sum of the SSC, External Inverse Compton (BLR) (EIC), External Compton (Disc) (ECD) and Extragalactic Background Light Absorption (EBL Abs.). The parameters used in their code

are shown in Table 4.2. The distance from the BH to the emission region is defined by z_0. The observation angle is the angle between our LOS and the jet. The BLR radiation field is approximately a black body. $L_B(jet)$ is the magnetic field luminosity, that is the energy that the magnetic field carries out along the jet. $L_B/L_e = U_B/U_e$ is the equipartition factor, where U_B is the energy density of the magnetic field and U_e is the energy density of the relativistic electrons.

4.3 Comparison to Previous Work: Model Results Using the BH mass obtained by Ghisellini et al. (2011)

For 4C+01.02, the BH mass 5×10^9 $M_\odot$ obtained by Ghisellini et al. (2011) was taken and used in the SED and total degree of polarisation model. This BH mass was tested in two ways: firstly, a sufficiently high enough synchrotron flux component compared to the accretion disc flux component is required to reproduce high enough total degree of polarisation when the unpolarised accretion disc emission dilutes the polarised synchrotron emission from the jet. These results are plotted in Figures 4.4 and 4.6 and obtained parameters with the fit and calculated values are given in Table 4.3. Note that for the quiescent state, the accretion disc peak could not be fitted to right of the optical photometry points, because this requires that the Eddington disc luminosity be exceeded. In the second way the disc luminosity is increased to shift the accretion disc component to the appropriate frequencies at which a decrease in the total degree of polarisation is expected. This required an accretion disc dominated spectrum (similar to how Ghisellini et al. (2011) have modelled their spectrum). These results are shown in Figures 4.5 and 4.7 and Table 4.4. The comparison between the results obtained where the BH mass is 4.0×10^8 $M_\odot$ and 5×10^9 $M_\odot$ is discussed in the next section.

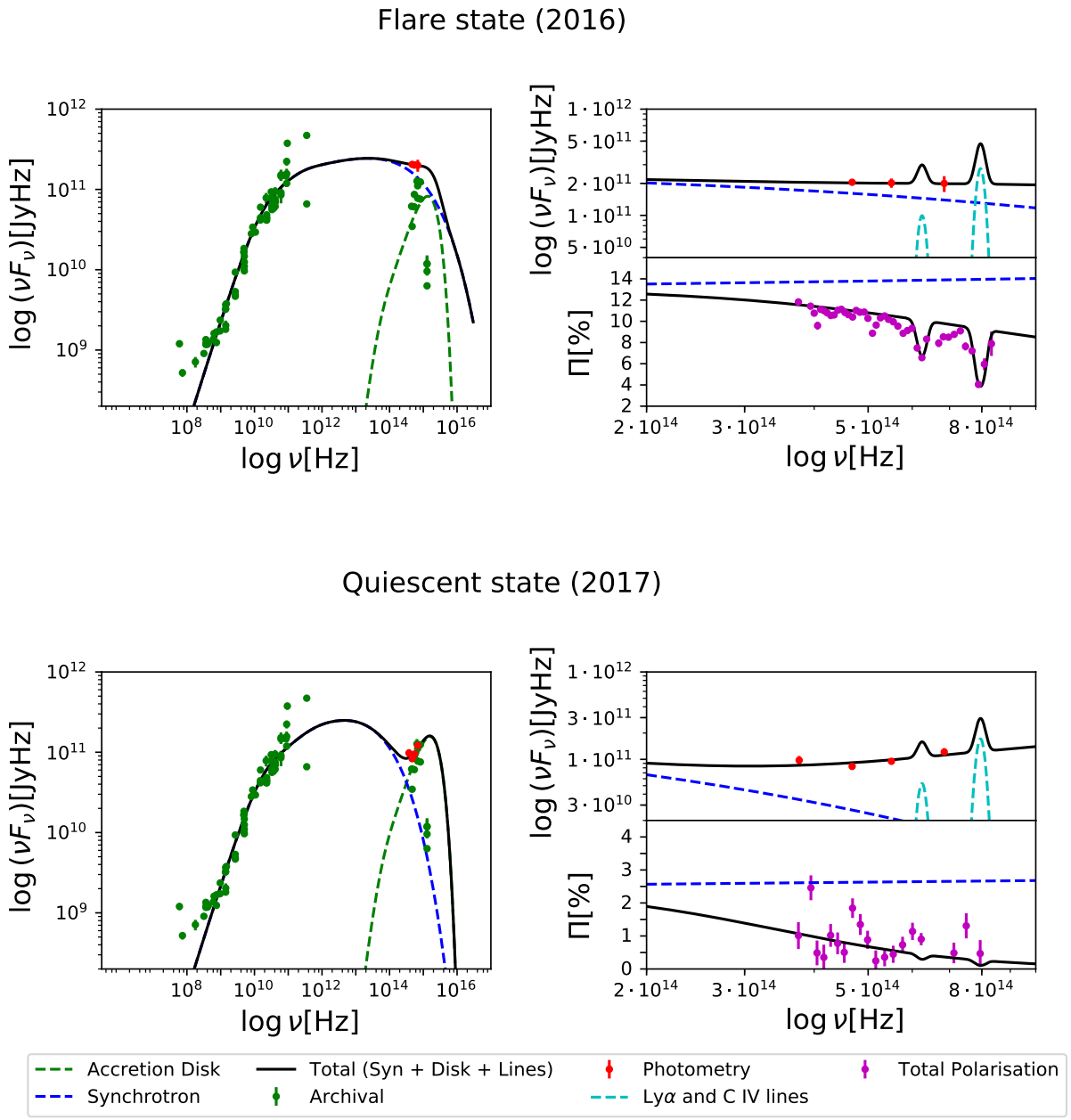

Figure 4.1: The simultaneous SED and polarisation model (lines) fitted to the observations (points) of 4C+01.02 in its flare (**upper plot**) and quiescent state (**lower plot**). The different model components and data are shown within the legend, where the archival data for the radio-, microwave-, visible- and UV spectra are taken from *NED results for object 4C +01.02* (2018), and the LCO photometry points for the flare are from 2 August 2016, produced by Johannes P. Marais and for the quiescent state are from 27 October 2017, produced by Brian van Soelen. The plots are shown as the low-frequency component SED (**left**), SED in the optical/UV frequency range (**upper right**) and the model prediction of the total degree of polarisation with the degree of synchrotron polarisation and SALT (RSS) degree of polarisation data (**lower right**). The total degree of polarisation data for the flare is from 9 July 2016 and for the quiescent state from 25 July 2017, which are produced by Brian van Soelen and Richard J. Britto.

Parameter	**Flare**	**Quiescent State**
Parameters Obtained with Fit		
Number of electrons n_0	6.4×10^{51}	2.0×10^{51}
Minimum gamma γ_{min}	27	27
Gamma break γ_b	1.2×10^2	1.9×10^2
Critical gamma γ_c	6.1×10^3	2.3×10^3
Minimum frequency ν_{min} [Hz]	1.0×10^{10}	1.0×10^{10}
Break frequency ν_b [Hz]	1.8×10^{11}	4.8×10^{11}
Critical frequency ν_c[Hz]	5.0×10^{14}	2.2×10^{13}
Electron spectral index p_1	2.0	2.2
Electron spectral index p_2	2.7	2.5
Ordering of magnetic field F_B	0.17	0.03
Disc luminosity L_d [erg $\cdot$ s^{-1}]	2.0×10^{46}	3.8×10^{46}
BH mass [$M_\odot$]	4.0×10^8	
C IV line height $h1$	0.5	
Lyα line height $h2$	1.4	
Calculated Values		
Photon spectral index α_1	0.5	0.6
Photon spectral index α_2	0.9	0.8
Maximum synchrotron polarisation $\Pi^{sy}_{max}(p_1)/F_B$ [%]	69	71
Maximum synchrotron polarisation $\Pi^{sy}_{max}(p_2)/F_B$ [%]	74	72
Maximum disc temperature T_{max} [K]	7.8×10^4	9.2×10^4
Accretion disc peak at ν_{in} [Hz]	1.5×10^{15}	1.7×10^{15}

Table 4.1: Parameters and values obtained with the model fit for 4C+01.02 in its flare, 2016 (column two) and quiescent state, 2017 (column three). The obtained Lorentz factors (energies) γ's are in the emission frame and the characteristic synchrotron frequencies ν are in the observer's frame.

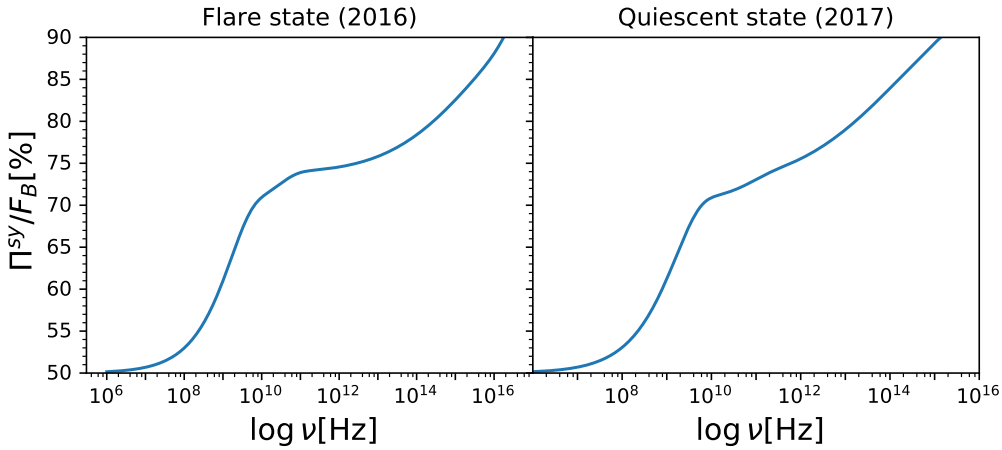

Figure 4.2: Degree of synchrotron polarisation divided by F_B, in units of percentage. This result, together with the results of Figure 4.1 and Table 4.1, obtains a BH mass of 4.0×10^8 $M_\odot$.

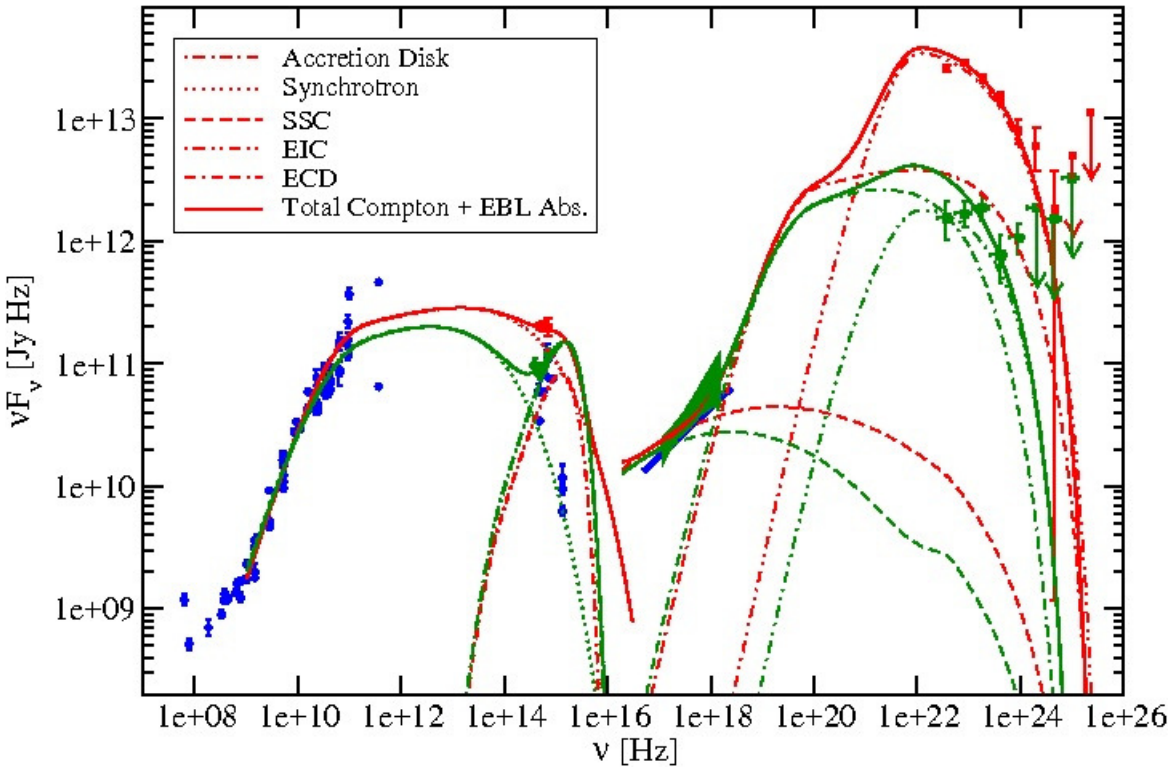

Figure 4.3: Broad-band SED for 4C+01.02 in its flare state of 2016 (red) and quiescent state of 2017 (green). The Leptonic model's X-ray and gamma-ray components are added to the model with the Böttcher et al. (2013) code. The model components are described by the legend. The X-ray data in the flare state is archival data from the summed observations of 2007-2008, since these correspond to the gamma-ray flux state and the quiescent state (2 August 2017) data is provided by Abe Falcone and Amanpreet Kaur. Gamma-ray data in the flare state (2-20 July 2016) and quiescent state (3 July-2 August, 2017) are produced by Richard J. Britto. This figure was produced by Markus Böttcher. Note that these fits are based on a preliminary version of the results.

Parameter	**Flare**	**Quiescent State**
Magnetic field [G]	0.3	
Emission region height z_0 [pc]	0.2	
Emission region radius R_e [cm]	9.5×10^{17}	7.5×10^{17}
Observing angle $\theta_{obs} = 1/\Gamma$ [rad]	5.7	
External radiation field energy density u [erg $\cdot$ cm^{-3}]	5.5×10^{-3}	4.0×10^{-4}
External radiation field black body temperature [K]	5.0×10^4	
$L_e(jet)$ [erg $\cdot$ s^{-1}]	8.0×10^{45}	
$L_B(jet)$ [erg $\cdot$ s^{-1}]	3.3×10^{46}	2.0×10^{46}
L_B/L_e	4.1	2.5
$dt_{var,\,min}$	9.8×10^6 s	7.7×10^6 s
	$= 2.7 \times 10^3$ h	$= 2.2 \times 10^3$ h

Table 4.2: 4C+01.02 Leptonic model parameters used in the Böttcher et al. (2013) code.

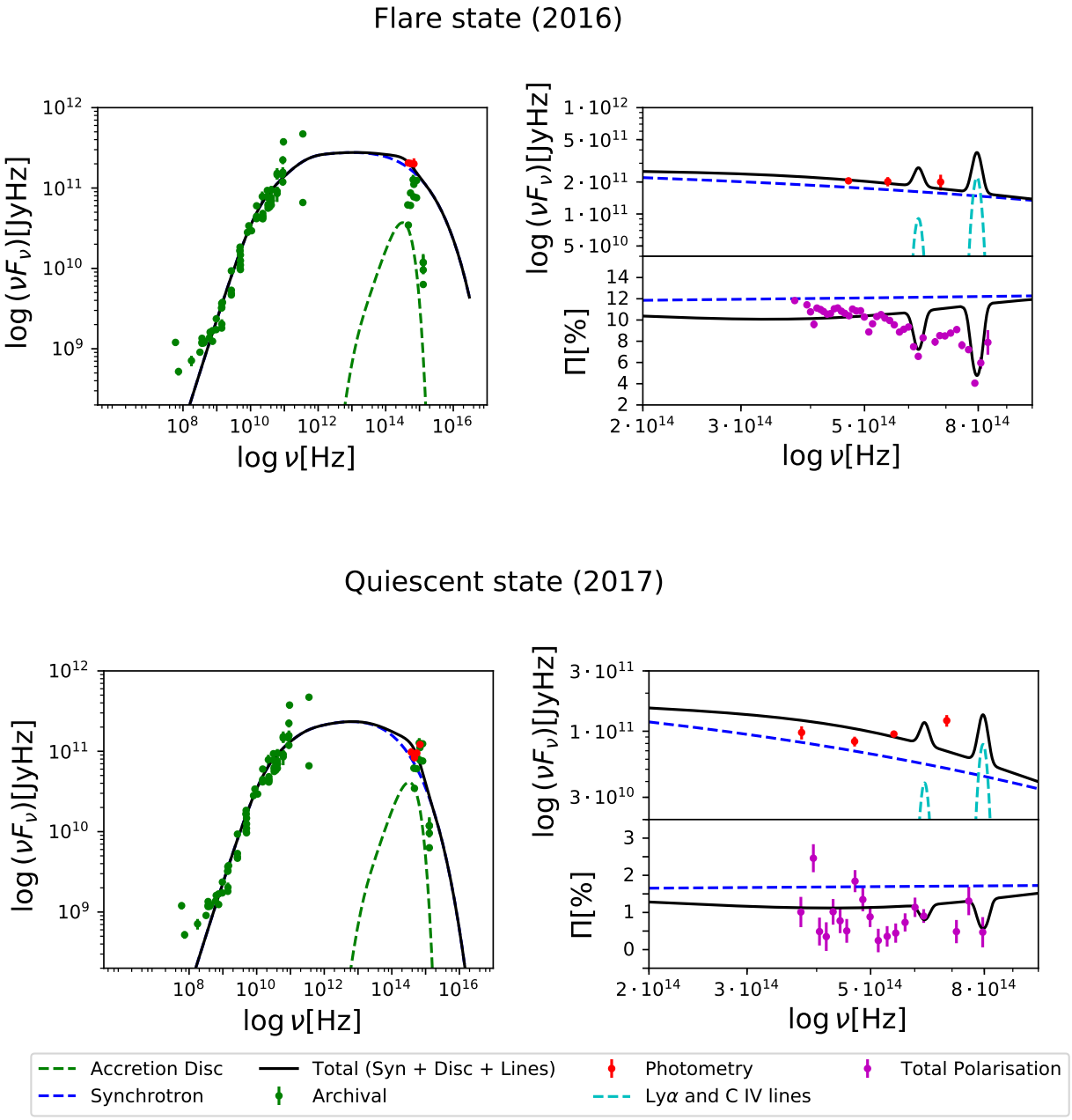

Figure 4.4: The SED (**left**) and degree of polarisation (**right**) of 4C+01.02 in its flare state of 2016 (**upper plot**) and quiescent state of 2017 (**lower plot**) as calculated by the model by implementing the BH mass of 5×10^9 $M_\odot$ obtained by Ghisellini et al. (2011). The figure data is as in Figure 4.1. Parameters obtained with the fit and calculated values are given in Table 4.3.

Parameter	**Flare**	**Quiescent State**
Parameters Obtained with Fit		
Number of electrons n_0	3.0×10^{51}	6.4×10^{51}
Minimum gamma γ_{min}	27	27
Gamma break γ_b	1.7×10^2	1.2×10^2
Critical gamma γ_c	7.7×10^3	2.6×10^3
Minimum frequency ν_{min} [Hz]	1.0×10^{10}	1.0×10^{10}
Break frequency ν_b [Hz]	3.9×10^{11}	1.9×10^{11}
Critical frequency ν_c[Hz]	8.0×10^{14}	9.0×10^{13}
Electron spectral index p_1	2.0	2.0
Electron spectral index p_2	2.9	2.7
Ordering of magnetic field F_B	0.15	0.02
Disc luminosity L_d [erg $\cdot$ s^{-1}]	9.0×10^{45}	1.0×10^{46}
C IV line height $h1$	0.5	
Lyα line height $h2$	1.4	
Calculated Values		
Photon spectral index α_1	0.5	0.5
Photon spectral index α_2	0.1	0.9
Maximum synchrotron polarisation $\Pi^{sy}_{max}(p_1)/F_B$ [%]	69	69
Maximum synchrotron polarisation $\Pi^{sy}_{max}(p_2)/F_B$ [%]	75	74
Maximum disc temperature T_{max} [K]	1.8×10^4	1.9×10^4
Accretion disc peak at ν_{in} [Hz]	3.3×10^{14}	3.6×10^{14}

Table 4.3: Parameters and values obtained for 4C+01.02 in its flare, 2016 (column two) and quiescent state, 2017 (column three) by implementing the BH mass 5×10^9 M$_\odot$ obtained by Ghisellini et al. (2011). These results correspond with Figures 4.4 and 4.6.

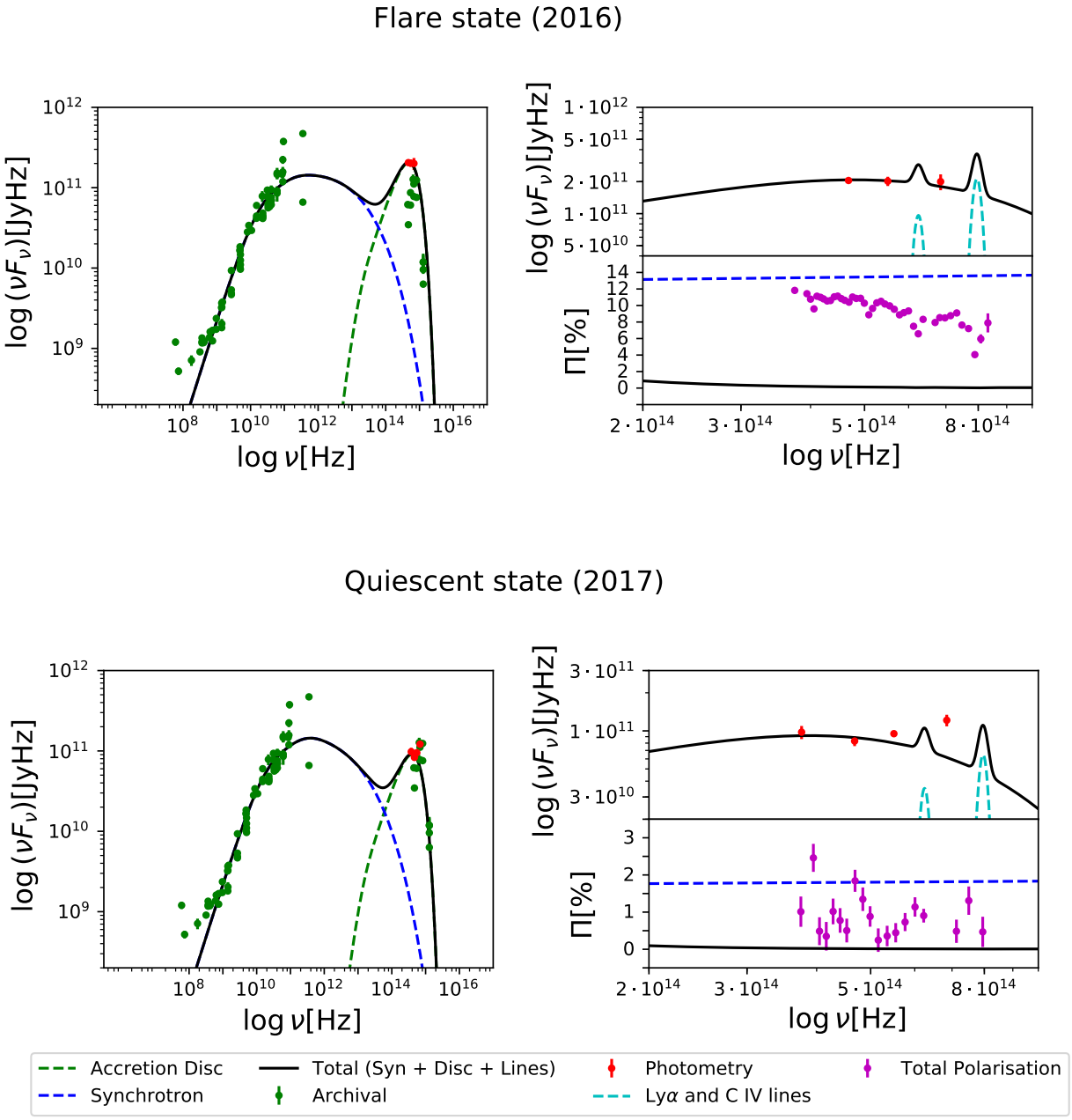

Figure 4.5: Accretion disc dominated SED (**left**) and degree of polarisation (**right**) of 4C+01.02 in its flare state of 2016 (**upper plot**) and quiescent state of 2017 (**lower plot**) as calculated by the model by implementing the BH mass of 5×10^9 $M_\odot$ obtained by Ghisellini et al. (2011). The figure data is as in Figure 4.1. Parameters obtained with the fit and calculated values are given in Table 4.4.

Parameter	**Flare**	**Quiescent State**
Parameters Obtained with Fit		
Number of electrons n_0	9.0×10^{51}	6.4×10^{51}
Minimum gamma γ_{min}	27	27
Gamma break γ_b	1.0×10^2	1.2×10^2
Critical gamma γ_c	8.6×10^2	7.7×10^2
Minimum frequency ν_{min} [Hz]	1.0×10^{10}	1.0×10^{10}
Break frequency ν_b [Hz]	1.4×10^{11}	2.0×10^{11}
Critical frequency ν_c[Hz]	1.0×10^{13}	8.0×10^{12}
Electron spectral index p_1	2.0	2.0
Electron spectral index p_2	2.8	3.0
Ordering of magnetic field F_B	0.99	0.02
Disc luminosity L_d [erg $\cdot$ s^{-1}]	5.0×10^{46}	2.2×10^{46}
C IV line height $h1$	0.5	
Lyα line height $h2$	1.4	
Calculated Values		
Photon spectral index α_1	0.5	-0.5
Photon spectral index α_2	0.9	0.8
Maximum synchrotron polarisation $\Pi^{sy}_{max}(p_1)/F_B$ [%]	69	44
Maximum synchrotron polarisation $\Pi^{sy}_{max}(p_2)/F_B$ [%]	74	73
Maximum disc temperature T_{max} [K]	2.8×10^4	2.3×10^4
Accretion disc peak at ν_{in} [Hz]	5.3×10^{14}	1.7×10^{15}

Table 4.4: Parameters and values obtained for an accretion disc dominated fit for 4C+01.02 in its flare, 2016 (column two) and quiescent state, 2017 (column three) by implementing the BH mass 5×10^9 M$_\odot$ obtained by Ghisellini et al. (2011). These results correspond with Figures 4.5 and 4.7.

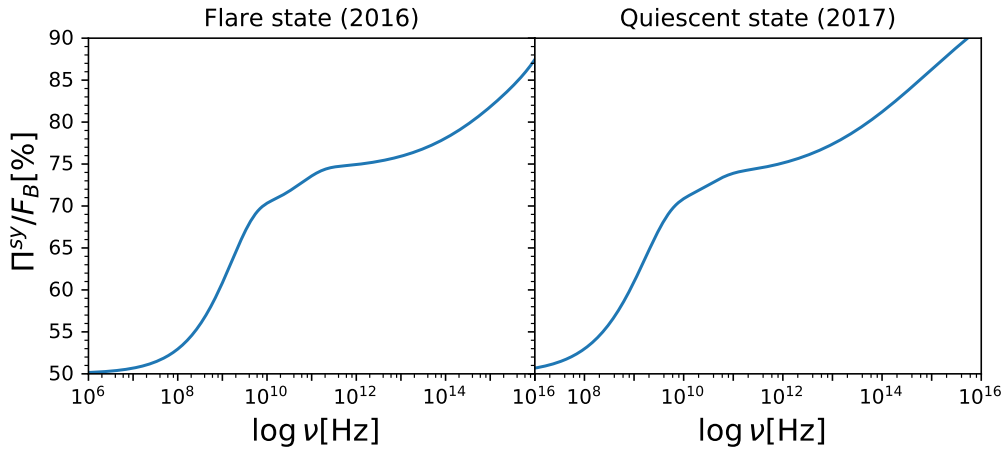

Figure 4.6: Degree of synchrotron polarisation divided by F_B, in units of percentage. This result, together with the results of Figure 4.4 and Table 4.3, implements the BH mass 5×10^9 $M_\odot$ obtained by Ghisellini et al. (2011).

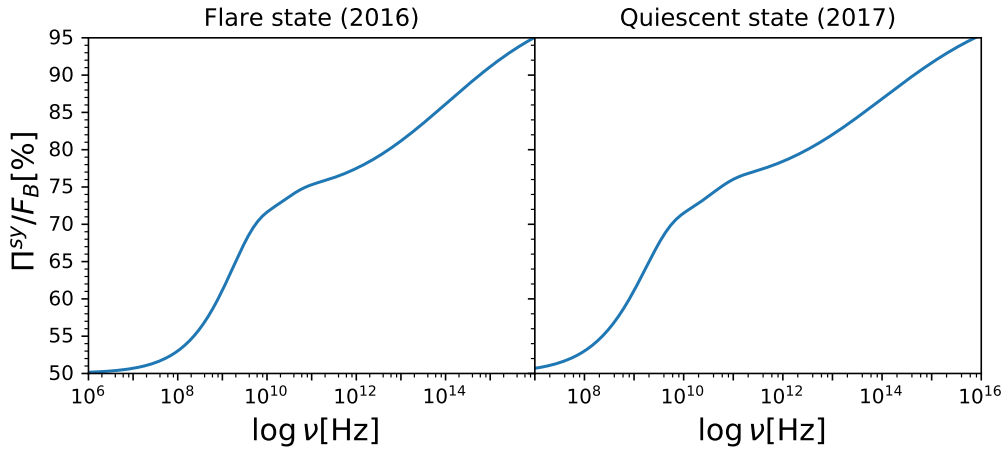

Figure 4.7: Degree of synchrotron polarisation divided by F_B, in units of percentage. This result, together with the results of Figure 4.5 and Table 4.4, implements the BH mass 5×10^9 $M_\odot$ obtained by Ghisellini et al. (2011).

Chapter 5

Discussion

The results were presented in Chapter 4. The model results are plotted in Figures 4.1 and 4.2. The obtained parameter values from the fit are given in Tabel 4.1. The broad-band SED is plotted in Figure 4.3 and the high-frequency component parameter values are given in Tabel 4.2. The results of implementing the obtained BH mass of Ghisellini et al. (2011) is shown in Figures 4.4, 4.6, 4.5 and 4.7 and Tables 4.3 and 4.4. The parameter values that are given in this chapter corresponding to the flare and quiescent state will be indicated by the superscripts f and q, respectively. Our model results will be indicated with superscript m. The parameters obtained by implementing the BH mass of Ghisellini et al. (2011) will be indicated with superscript G and G, PS for the results where the accretion disc peak has shifted and G, AD for the results with a dominating accretion disc component.

5.1 Simultaneous Fit Results

The general model results are described, where-after the results of the flare and quiescent state are compared to one another.

In the left plots of Figure 4.1 the synchrotron and accretion disc flux components are disentangled to determine the decrease in polarisation attributed by the accretion disc to the total polarisation.

In the right, lower plots of Figure 4.1 the total degree of polarisation shows a decrease towards the higher frequencies. This supports the main expected result: the accretion disc dilutes the synchrotron polarisation degree. The total polarisation degree decreases towards higher frequencies due to the unpolarised accretion disc. Thereby, the model constrains the disc component with the use of SALT spectropolarimetry observations.

Comparing the degree of synchrotron polarisation of the lower right plots of Figure 4.1, $\Pi^{sy}/F_B(\nu)$, to $\Pi^{sy}(\nu)$ Figure 4.2, the fit clearly necessitates a choice of $F_B < 1$, i.e., an only partially ordered magnetic field. The maximum degree of synchrotron polarisation in the first part of the broken power law spectrum $\Pi^{sy}_{max}(p^f_1)/F^f_B = 69$ and $\Pi^{sy}_{max}(p^q_1)/F^q_B = 71$, can be seen at the zero slopes of these plots, with $p^f_1 = 2.0$ and $p^q_1 = 2.2$. In the second part of the broken power law spectrum, $\Pi^{sy}_{max}(p^f_2)/F^f_B = 74$ and $\Pi^{sy}_{max}(p^q_2)/F^q_B = 72$, which can be seen at the zero slopes of these plots, with $p^f_2 = 2.7$ and $p^q_2 = 2.5$. These obtained spectral indices fall into the expected range of $2 < p < 3$.

In the right plots of Figure 4.1, the total flux peaks at the Lyα and C IV emission line frequencies. In the lower plot the total polarisation percentage decreases at the locations of the unpolarised emission lines.

Comparing the Flare and Quiescent State

Examining the right plots of Figure 4.1, the percentage of polarisation is higher for the flare, being observable in the range $\sim 4 - 12.1$ %, compared to that of the quiescent state $\sim 0.1 - 1.9$ %. The higher degree of polarisation corresponds to the higher ordering of the magnetic field for the flare state $F_B^f = 0.17$, compared to the lower degree of polarisation corresponding to $F_B^q = 0.03$ in the quiescent state. This is a known relationship where a higher degree of polarisation is found for a higher ordering of the magnetic field (Smith et al., 1986; Zhang and Böttcher, 2013). The higher synchrotron radiation level is due to a higher n_0 and higher γ_c. The degree of polarisation of the flare data is over a greater degree of polarisation region than the quiescent state's, resulting in the error bars of the flare data to be less visible in the plots than those of the quiescent state.

The maximum disc temperature during the flare, $T_{max}^f = 7.8 \times 10^4$ K, increased to $T_{max}^q = 9.2 \times 10^4$ K during the quiescent state. The maximum temperature is dependent on the accretion rate, since $T_{max} \propto l^{1/4} M_{BH}^{-1/4}$ for $l = \dot{M_{BH}}/\dot{M}_{Edd}$ (from Chapter 1). The accretion rate is dependent on the disc luminosity, since $\dot{M_{BH}} = L_d/\epsilon c^2$, thereby a higher accretion rate will mean that there is a higher disc luminosity in the quiescent state, which the results agree with having a direct dependence between the disc temperature and disc luminosity with ($L_d^q = 3.8 \times 10^{46}$ erg.s^{-1}) > ($\mathrm{L_d^f} = 2.0 \times 10^{46}$ erg.s^{-1}).

5.2 Physical Interpretation of the Broad-band SED

The lower ECD radiation from the higher accretion disc radiation in the quiescent state, could be due to a higher mass accretion rate suppressing the jet formation during this state. Furthermore, the lower external radiation field in the quiescent state $u^q = 4.0 \times 10^{-4}$ erg$\cdot$cm^{-3} compared to the flare's $u^f = 5.5 \times 10^{-3}$ erg$\cdot$cm^{-3}, suggests that the emission region is further away from the disc during the quiescent state to produce a lower ECD component than the flare's.

The EIC component is dominant in the contribution to the total high-frequency component of the flare. Since, the EIC emission is due to scattering of photons from the BLR, this could indicate that the whole emission region is radiating inside the BLR (where the energy density could be isotropic) during the flare and is outside the BLR (where the emission region only has clouds on one side giving anisotropic energy density) suppressing EIC radiation, during the quiescent state.

The higher ordered magnetic field in the flare state suggests the presence of shocks (Fermi acceleration) which compress, enhance and order the magnetic fields. This agrees in obtaining higher jet components (synchrotron, SSC, EIC andECD). Magnetic reconnection destroys magnetic fields and leads to lower degree of polarisation. In the quiescent state, the

lower ordering of the magnetic field implies that there are different magnetic field orientations that can cancel each other out. The synchrotron radiation producing photons to produce SSC radiation, also behaves as expected with higher/lower synchrotron radiation producing higher/lower SSC radiation for the flare/quiescent state.

5.3 Comparison to Previous Work

Ghisellini et al. (2011) obtained disc luminosities $10^{-2} < L_d/L_{Edd} < 1$ for FSRQs, $z > 2$, with BH masses in the range $\sim 10^8$ $M_\odot$ to 10^{11} $M_\odot$. The disc luminosities of our model are $L_d^f = 2.0 \times 10^{46}$ erg $\cdot$ s^{-1} and $L_d^q = 3.8 \times 10^{46}$ erg $\cdot$ s^{-1}, so that $L_d^f/L_{Edd} = 0.40$ and $L_d^q/L_{Edd} = 0.76$, with $L_{Edd} = 5.0 \times 10^{46}$ erg $\cdot$ s^{-1}. The BH mass obtained by the model $M_{BH}^m = 4.0 \times 10^8$ $M_\odot$ and the disc luminosities fall within the range of Eddington ratios found by Ghisellini et al. (2011).

The acquired BH mass $M_{BH}^m = 4.0 \times 10^8$ $M_\odot$ from the model is lower than the prediction of Ghisellini et al. (2011) who obtained $M_{BH}^G = 5 \times 10^9$ $M_\odot$. The comparison results with M_{BH}^G and $10^{-2} < L_d/L_{Edd} < 1$ are given in Figures 4.4, 4.6, 4.5 and 4.7 and Tables 4.3 and 4.4. By implementing M_{BH}^G in the model, it is demonstrated how BH mass influences the accretion disc flux component and thereby the total degree of polarisation fit:

For BH mass M_{BH}^m, the peak of the accretion disc flux component frequency at the inner disc radius is at $\nu_{in}^{m,\,f} = 1.5 \times 10^{15}$ Hz for the flare and $\nu_{in}^{m,\,q} = 1.7 \times 10^{15}$ Hz for the quiescent state. For the higher BH mass M_{BH}^G, these accretion disc flux peaks are at $\nu_{in}^{G,\,PS,\,f} = 3.3 \times 10^{14}$ Hz for the flare and $\nu_{in}^{G,\,PS,\,q} = 3.6 \times 10^{14}$ Hz for the quiescent state. Therefore, higher BH mass M_{BH}^G shifts the peaks to lower frequencies, as expected from the relation $\nu_{max}^{in} \propto M_{BH}^{-1/4}$. This causes the polarisation to decrease at lower frequencies (Figure 4.4, lower right). This demonstrates how the total degree of polarisation curve profile moves to lower frequencies for higher BH mass. With increased disc luminosities, dominating accretion disc flux components can fit the optical photometry data points in the SEDs for which the accretion disc peaks are at $\nu_{in}^{G,\,AD,\,f} = 5.3 \times 10^{14}$ Hz for the flare and $\nu_{in}^{G,\,AD,\,q} = 1.7 \times 10^{15}$ Hz for the quiescent state. Although the disc component is at the expected frequency region, these dominating accretion disc SEDs result in total degree of polarisation of about zero due to the high emission of the unpolarised accretion disc diluting the low emission of the polarised synchrotron radiation from the jet (Figures 4.4 and 4.5). Note that increasing F_B increases the synchrotron polarisation, but the ratio between the accretion disc and synchrotron emission will stay the same (equation (1.74)). Our best-fit value of 4.0×10^8 $M_\odot$ is favoured by the combined SED and spectropolarimetry fitting.

Chapter 6

Summary and Conclusions

With the use of archival, optical, X-ray and gamma-ray flux data, and the spectropolarimetry observations from the Large SALT Program (Chapter 3), 4C+01.02 ($z = 2.1$) was successfully modelled with a simultaneous SED and spectropolarimetry fit (Chapter 2). This source is modelled in its flare and quiescent state with its BH mass obtained as $4.0 \times 10^8\ M_\odot$ (Chapter 4). The fit is based on synchrotron, accretion disc and emission lines components contributing to the SED and optical/UV polarisation. The decrease in the total degree of polarisation is due to the unpolarised disc that is diluting the synchrotron polarisation. The SED and optical polarisation model constrained the accretion disc to the blue end of the optical spectrum, thereby disentangling the disc and synchrotron components.

The flare/quiescent state was characterized by a lower/higher accretion rate (and, thus, accretion disc luminosity), but more/less intense particle acceleration in the jet, and, hence, higher/lower non-thermal emissions from the jet. In the quiescent state, a high accretion rate could be suppressing the jet formation, a process that is also present in Galactic BH X-ray binary systems. The higher jet components during the flare suggest the presence of a shock accelerating particles more efficiently and in turn producing the higher degree of total polarisation. A higher external radiation field energy density in the flare state produces higher ECD radiation compared to the quiescent state, implying that the emission region in the quiescent state could be further away from the disc. The high/low EIC radiation during the flare/quiescent state suggest that the emission region is inside/outside the BLR.

The acquired BH mass $4.0 \times 10^8\ M_\odot$, from the model was compared to the prediction of Ghisellini et al. (2011) who obtained a BH mass of 5×10^9 $M_\odot$. The position of the accretion disc peak and the correct ratio of synchrotron to accretion disc flux, are essential ingredients to fitting the total degree of polarisation. A higher BH mass shifts the accretion disc flux component peak to lower frequencies in the EM spectrum and shifts the decrease in the total degree of polarisation towards lower frequencies. A dominating accretion disc flux component in the SED has the result of about zero total degree of polarisation. The BH mass obtained by Ghisellini et al. (2011) gave an accretion disc peak at too low frequencies or a dominating accretion disc component in the EM spectrum. The model discussed in this dissertation constrains the accretion disc component and BH mass by fitting the total degree of polarisation data.

The results are preliminary, since the degeneracy in electron energies and the magnetic field, in this study, was only done posteriorly and not used as independent constraints on the electron energy distribution. By only including synchrotron radiation, the emission region radius is not taken into account. When Compton scattering radiation is also included in the model fit, this radius can be constrained, which gives the density of the particles in the emission region. For future fitting of sources the dust torus and host galaxy can also be considered.

Chapter 7

Outlook

My studies will be continued by further developing this code with my supervisor, Professor Markus Böttcher. The Leptonic model will be used to extend our model to include the SSC radiation and EC radiation. The SSC polarisation can be modelled similarly to Zhang and Böttcher (2013) and with the future Imaging X-ray Polarimetry Explorer (IXPE), X-ray polarisation observations will test the polarisation predictions in the X-ray spectrum.

In this dissertation we studied one source, the FSRQ 4C+01.02. The SALT Large Program ToO program is continuing and with co-ordinated multi-wavelength observations data more sources will be available to fit spectropolarimetry and SEDs with our model.

ACKNOWLEDGEMENTS

First off, I would like acknowledge my supervisor, Professor Markus Böttcher of the North-West University, to whom this project is mainly accredited to. I would like to thank Prof. Böttcher for his patient guidance, encouragement, useful critiques and keeping my progress on schedule. In need of help he was always reachable and would give me a clear view on how to proceed. Prof. Böttcher is an inspiring mentor and I am looking forward on continuing this project with him.

Furthermore, I would like to acknowledge and thank the following collaborators who contributed in collecting and coordinating the multiwavelength observations: Dr. Brian van Soelen and Mr. Johannes P. Marais from the UFS, for producing the LCO photometry data. Dr. Van Soelen and Dr. Richard Britto from the UFS, for producing the SALT spectropolarimetry data. Dr. David A.H. Buckley from the SAAO for leading the SALT Large Program ToO spectropolarimetry observations. Prof. Abe Falcone and Dr. Amanpreet Kaur from the Pennsylvania State University, for the Swift XRT-data reductions. Dr. Richard J. Britto for contributing the Fermi-LAT data and for his valuable comments on my conference presentations.

I would like to acknowledge and thank Dr. Zorawar Wadiasingh that did the language editing of this dissertation.

I would like to thank Dr. Sunil Chandra for his advice on the python fit function and valuable critiques on presenting the results.

For financial assistance in my studies I would like to thank the following bursars: the Centre for Space Research (CSR), the North-West University (NWU), the National Research Foundation (NRF) and Prof. Böttcher.

Appendix A

Finding the Maximum Accretion disc Temperature

Differentiate equation (1.14) and set the result equal to zero to find the radius at which the maximum disc temperature occurs:

$$\frac{\partial T(R)}{\partial R} = 0 \tag{A.1}$$

$$= \frac{\partial}{\partial R}\left[T_0\left(\frac{R_{in}}{R}\right)^{3/4}\left(1-\sqrt{\frac{R_{in}}{R}}\right)^{1/4}\right] \tag{A.2}$$

Knowing that $T_0 \propto R^{-3/4}$:

$$\frac{\partial T(R)}{\partial R} = \frac{\partial}{\partial R}\left[R_{in}^{-3/4}\left(\frac{R_{in}}{R}\right)^{3/4}\left(1-\sqrt{\frac{R_{in}}{R}}\right)^{1/4}\right] \tag{A.3}$$

$$= -\frac{3}{4}R^{-7/4}\left(1-R_{in}^{1/2}R^{-1/2}\right)^{1/4} + \frac{1}{8}R^{-9/2}R_{in}^{1/2}\left(1-R_{in}^{1/2}R^{-1/2}\right)^{-3/4} \tag{A.4}$$

With this equal to zero it can be easily solved:

$$\frac{3}{4}R^{-7/4}\left(1-R_{in}^{1/2}R^{-1/2}\right)^{1/4} = \frac{1}{8}R_{in}^{1/2}R^{-9/2}\left(1-R_{in}^{1/2}r^{-1/2}\right)^{-3/4} \tag{A.5}$$

$$\frac{R^{-7/4}\left(1-R_{in}^{1/2}R^{-1/2}\right)^{1/4}}{R^{-9/4}\left(1-R_{in}^{1/2}R^{-1/2}\right)^{-3/4}} = \frac{1}{8}\left(\frac{3}{4}\right)^{-1}R_{in}^{1/2} \tag{A.6}$$

$$R^{1/2}\left(1-R_{in}^{1/2}R^{-1/2}\right) = \frac{1}{6}R_{in}^{1/2} \tag{A.7}$$

$$(R^{1/2})^2 = \left(\frac{7}{6}R_{in}^{1/2}\right)^2 \tag{A.8}$$

$$R = \frac{49}{36}R_{in}. \tag{A.9}$$

The maximum disc temperature is at this radius and therefore by substituting equation (A.9) into equation (1.14) it can be easily found:

$$T_{max} = \left(\frac{36}{49}\right)^{3/4} \left(1 - \sqrt{\frac{36}{49}}\right)^{1/4} T_0 \tag{A.10}$$

$$= \left(\frac{36}{49}\right)^{3/4} \left(\frac{1}{7}\right)^{1/4} T_0 \tag{A.11}$$

$$= \left(\frac{1}{7}\right)^{3/2} 6^{3/2} \left(\frac{1}{7}\right)^{1/4} T_0 \tag{A.12}$$

$$= \frac{6\sqrt{6}}{7^{7/4}} T_0. \tag{A.13}$$

Appendix B

Numerical Calculations: Midpoint Integration Technique

The numerical midpoint integration technique is used in the model code to calculate the synchrotron flux, accretion disc flux and synchrotron polarisation. The integration of a function $f(x)$ is approximated as

$$\int_a^b f(x)dx \approx h_1 f\left(\frac{x_0 + x_1}{2}\right) + h_2 f\left(\frac{x_1 + x_2}{2}\right) + ... + h_n f\left(\frac{x_{n-1} + x_n}{2}\right), \qquad \text{(B.1)}$$

where the increment length $h_1 = x_1 - x_0$, $h_2 = x_2 - x_1$, ..., $h_n = x_n - x_{n-1}$, with x_i increasing logarithmically for every $i = 0, 1, 3, ..., n$.

Bibliography

Abdo, A. A., Ackermann, M., Ajello, M., Atwood, W. B., Axelsson, M., Baldini, L., ... and Ziegler, M. (2009), 'Bright Active Galactic Nuclei Source List from the First Three Months of the Fermi Large Area Telescope All-Sky Survey', *Astrophysical Journal* **700**, 597–622.

A Black Hole Overflows From Galaxy Centaurus A (2009), `https://www.nasa.gov/multimedia/imagegallery/image_feature_1276.html` Date of access: 12 Feb. 2019.

Arav, N., de Kool, M., Korista, K. T., Crenshaw, D. M., van Breugel, W., Brotherton, M., ... and Murray, N. (2001), 'HST STIS Observations of PG 0946+301: The Highest Quality UV Spectrum of a BALQSO', *Astrophysical Journal* **561**, 118–130.

Atwood, W., Albert, A., Baldini, L., Tinivella, M., Bregeon, J., Pesce-Rollins, M., ... and S. Zimmer for the Fermi-LAT Collaboration (2013), 'Pass 8: Toward the Full Realization of the Fermi-LAT Scientific Potential', *ArXiv e-prints* .

Atwood, W. B., Abdo, A. A., Ackermann, M., Althouse, W., Anderson, B., Axelsson, M., ... and Ziegler, M. (2009), 'The Large Area Telescope on the Fermi Gamma-Ray Space Telescope Mission', **697**, 1071–1102.

Barres de Almeida, U., Tavecchio, F. and Mankuzhiyil, N. (2014), 'Polarimetric tomography of blazar jets', *Monthly Notices of the Royal Astronomical Society* **441**, 2885–2890.

Barthelmy, S. D., Barbier, L. M., Cummings, J. R., Fenimore, E. E., Gehrels, N., Hullinger, D., ... and Tueller, J. (2005), 'The Burst Alert Telescope (BAT) on the SWIFT Midex Mission', **120**, 143–164.

Beckmann, V. and Shrader, C. R. (2012), *Active Galactic Nuclei*, Wiley-VCH.

Bessell, M. S., Castelli, F. and Plez, B. (1998), 'Model atmospheres broad-band colors, bolometric corrections and temperature calibrations for O - M stars', *Astronomy & Astrophysics* **333**, 231–250.

Böttcher, M. (2007), 'Modeling the emission processes in blazars', *Astrophysics and Space Science* **309**, 95–104.

Böttcher, M. (2010), Models for the Spectral Energy Distributions and Variability of Blazars, *in* T. Savolainan, E. Ros, R. W. Porcas and J. A. Zensus, eds, 'Proc. Fermi Meets Jansky', MPIfR, Bonn, Germany.

Böttcher, M., Harris, D. E. and Krawczynski, H. (2012), *Relativistic Jets from Active Galactic Nuclei*, Berlin: Wiley.

Böttcher, M., Reimer, A., Sweeney, K. and Prakash, A. (2013), 'Leptonic and Hadronic Modeling of Fermi-detected Blazars', *Astrophysical Journal* **768**, 54.

Böttcher, M., van Soelen, B., Britto, R., Buckley, D., Marais, J. and Schutte, H. (2017), 'SALT Spectropolarimetry and Self-Consistent SED and Polarization Modeling of Blazars', *Galaxies* **5**, 52.

Brandt, W. N. and Alexander, D. M. (2015), 'Cosmic X-ray surveys of distant active galaxies. The demographics, physics, and ecology of growing supermassive black holes', *Astronomy & Astrophysics Review* **23**, 1.

Brown, T. M., Baliber, N., Bianco, F. B., Bowman, M., Burleson, B., Conway, P., ... and Willis, M. (2013), 'Las Cumbres Observatory Global Telescope Network', *Publications of the Astronomical Society of the Pacific* **125**, 1031.

Burke-Spolaor, S., Gultekin, K., Postman, M., Lauer, T. R., Taylor, J. M., Lazio, T. J. W. and Moustakas, L. A. (2017), 'A radio relic and a search for the central black hole in the abell 2261 brightest cluster galaxy', *Astrophysical Journal* **849**.

Burrows, D. N., Hill, J. E., Nousek, J. A., Kennea, J. A., Wells, A., Osborne, J. P., ... and Hartner, G. D. (2005), 'The Swift X-Ray Telescope', **120**, 165–195.

Cao, X. (2018), 'The power of the jets accelerated by the coronal magnetic field', *Monthly Notices of the Royal Astronomical Society* **473**, 4268–4271.

Carilli, C. L. and Barthel, P. D. (1996), 'Cygnus A', *Astronomy & Astrophysics Review* **7**, 1–54.

Carroll, B. W. and Ostlie, D. A. (2014), *An Introduction to Modern Astrophysics*, 2 edn, Pearson.

Cerruti, M., Zech, A., Emery, G. and Guarin, D. (2017), Hadronic modeling of TeV AGN: Gammas and neutrinos, *in* '6th International Symposium on High Energy Gamma-Ray Astronomy', Vol. 1792 of *American Institute of Physics Conference Series*, p. 050027.

Cosmology - Galaxies (2004-2013), `http://astronomyonline.org/Cosmology/Galaxies.asp` Date of access: 12 Feb. 2019.

Crawford, S. M., Still, M., Schellart, P., Balona, L., Buckley, D. A. H., Gulbis, A. A. S., ... and Zietsman, E. (2012), 'PySALT: SALT science pipeline', Astrophysics Source Code Library.

Crenshaw, D. M., Kraemer, S. B., Boggess, A., Maran, S. P., Mushotzky, R. F. and Wu, C.-C. (1999), 'Intrinsic Absorption Lines in Seyfert 1 Galaxies. I. Ultraviolet Spectra from the Hubble Space Telescope', **516**, 750–768.

Crusius, A. and Schlickeiser, R. (1986), 'Synchrotron radiation in random magnetic fields', *Astronomy & Astrophysics Review* **164**, L16–L18.

Eberhardt, W. (2015), 'Synchrotron radiation: A continuing revolution in X-ray science—Diffraction limited storage rings and beyond.', *Journal of Electron Spectroscopy and Related Phenomena* pp. 31–39.

Fossati, G., Maraschi, L., Celotti, A., Comastri, A. and Ghisellini, G. (1998), 'A unifying view of the spectral energy distributions of blazars', *Monthly Notices of the Royal Astronomical Society* **299**, 433–448.

Franceschini, A., Hasinger, G., Miyaji, T. and Malquori, D. (1999), 'On the relationship between galaxy formation and quasar evolution', *Monthly Notices of the Royal Astronomical Society* **310**, L5–L9.

Frank, J., King, A. and Raine, D. J. (2002), *Accretion Power in Astrophysics*, 3 edn, Cambridge University Press.

Ghisellini, G., Tagliaferri, G., Foschini, L., Ghirlanda, G., Tavecchio, F., Della Ceca, R., ... and Gehrels, N. (2011), 'High-redshift Fermi blazars', *Monthly Notices of the Royal Astronomical Society* **411**, 901–914.

Ghisellini, G. and Tavecchio, F. (2009), 'Canonical high-power blazars', *Monthly Notices of the Royal Astronomical Society* **397**, 985–1002.

Ghisellini, G., Tavecchio, F., Foschini, L., Ghirlanda, G., Maraschi, L. and Celotti, A. (2010), 'General physical properties of bright Fermi blazars', *Monthly Notices of the Royal Astronomical Society* **402**, 497–518.

Gómez, J. L., Lobanov, A. P., Bruni, G., Kovalev, Y. Y., Marscher, A. P., Jorstad, S. G., ... and Lisakov, M. M. (2016), 'Probing the Innermost Regions of AGN Jets and Their Magnetic Fields with RadioAstron. I. Imaging BL Lacertae at 21 Microarcsecond Resolution', *Astrophysical Journal* **817**, 96.

Griffiths, D. J. (2013), *Introduction to electrodynamics; 4th ed.*, Boston, MA: Pearson.

Hartle, J. B. (2003), *Gravity : an introduction to Einstein's general relativity*, San Francisco, CA, USA: Addison Wesley.

Katz, U. F. and Spiering, C. (2012), 'High-energy neutrino astrophysics: Status and perspectives', *Progress in Particle and Nuclear Physics* **67**, 651–704.

Kobulnicky, H. A., Nordsieck, K. H., Burgh, E. B., Smith, M. P., Percival, J. W., Williams, T. B. and O'Donoghue, D. (2003), The prime focus imaging spectrograph for the Southern African Large Telescope- Operational modes., pp. 4841, 1634–1644.

Liu, X. (2009), On the Difference of Quasars and BL Lac Objects, *in* Y. Hagiwara, E. Fomalont, M. Tsuboi and M. Yasuhiro, eds, 'Approaching Micro-Arcsecond Resolution with VSOP-2: Astrophysics and Technologies', Vol. 402 of *Astronomical Society of the Pacific Conference Series*, p. 307.

Longair, M. S. (2011), *High Energy Astrophysics*, Cambridge University Press.

Marconi, A., Risaliti, G., Gilli, R., Hunt, L. K., Maiolino, R. and Salvati, M. (2004), 'Local supermassive black holes, relics of active galactic nuclei and the X-ray background', *Monthly Notices of the Royal Astronomical Society* **351**, 169–185.

Marscher, A. (2006), Relativistic Jets in AGN and their Relationship to the Central Engine, *in* 'VI Microquasar Workshop: Microquasars and Beyond', p. 25.1.

Mastichiadis, A. (1996), 'The Hadronic Model of Active Galactic Nuclei', *Space Science Reviews* **75**, 317–329.

Mueller, C., Kadler, M., Ojha, R., Wilms, J., Boeck, M., Edwards, P., ... and Katz, U. (2011), 'Dual-frequency VLBI study of Centaurus A on sub-parsec scales The highest-resolution view of an extragalactic jet.', *Astronomy & Astrophysics* **530**, 4.

Nave, R. (n.d.), 'Classification of Polarization', `http://hyperphysics.phy-astr.gsu.edu/hbase/phyopt/polclas.html` Date of access: 12 Feb. 2019.

NED results for object 4C +01.02 (2018), `http://ned.ipac.caltech.edu/cgi-bin/objsearch?objname=4C%2B01.02&extend=no&hconst=73&omegam=0.27&omegav=0.73&corr_z=1&out_csys=Equatorial&out_equinox=J2000.0&obj_sort=RA+or+Longitude&of=pre_text&zv_breaker=30000.0&list_limit=5&img_stamp=YES` Date of access: 12 Feb. 2019.

Netzer, H. (2013), *The Physics and Evolution of Active Galactic Nuclei*, Tel Aviv University: Cambridge University Press.

Park, D., Barth, A. J., Woo, J.-H., Malkan, M. A., Treu, T., Bennert, V. N., ... and Pancoast, A. (2017), 'Extending the Calibration of C IV-based Single-epoch Black Hole Mass Estimators for Active Galactic Nuclei', *Astrophysical Journal* **839**, 93.

Polarimetric reductions for SALT (2019), `https://github.com/saltastro/polsalt/` Date of access: 12 Feb. 2019.

Radiative Processes in High Energy Astrophysics (2013), *in* G. Ghisellini, ed., 'Lecture Notes in Physics, Berlin Springer Verlag', Vol. 873 of *Lecture Notes in Physics, Berlin Springer Verlag*.

Roming, P. W. A., Kennedy, T. E., Mason, K. O., Nousek, J. A., Ahr, L., Bingham, R. E., ... and Stock, J. (2005), 'The Swift Ultra-Violet/Optical Telescope', **120**, 95–142.

Rybicki, G. B. and Lightman, A. P. (1979), *Radiative processes in astrophysics*, New York: Wiley-Interscience.

Shakura, N. I. and Sunyaev, R. A. (1973), 'Black holes in binary systems. Observational appearance.', *Astronomy & Astrophysics* **24**, 337–355.

Shen, Y., Richards, G. T., Strauss, M. A., Hall, P. B., Schneider, D. P., Snedden, S., ... and Simmons, A. (2011), 'A Catalog of Quasar Properties from Sloan Digital Sky Survey Data Release 7', *Astrophysical Journal Supplements* **194**, 45.

Simultaneous data fitting in python with leastsq (2014), https://stackoverflow.com/questions/24820715/simultaneous-data-fitting-in-python-with-leastsq Date of access: 12 Feb. 2019.

Smith, P. S., Balonek, T. J., Heckert, P. A. and Elston, R. (1986), 'The optical and near-infrared polarization properties of the OVV quasar 3C 345', *Astrophysical Journal* **305**, 484–495.

Spectral Properties of Synchrotron Radiation (2010), http://uspas.fnal.gov/materials/10UCSC/Lecture_2a_Synch_Radiation.pdf Date of access: 12 Feb. 2019.

Supermassive Black Holes: What Quasars really are (n.d.), https://phys.libretexts.org/TextMaps/Astronomy_and_Cosmology_TextMaps/Map%3A_Astronomy_(OpenStax)/27%3A_Active_Galaxies%2C_Quasars%2C_and_Supermassive_Black_Holes/27.2%3A_Supermassive_Black_Holes%3A_What_Quasars_really_are Date of access: 12 Feb. 2019.

Türler, M., Paltani, S., Courvoisier, T. J. L., Aller, M. F., Aller, H. D., Blecha, A., ... and Wright, M. C. H. (1999), '30 years of multi-wavelength observations of 3C 273', *Astronomy & Astrophysics Supplements* **134**, 89–101.

Urry, C. M. and Padovani, P. (1995), 'Unified Schemes for Radio-Loud Active Galactic Nuclei', *Publications of the Astronomical Society of the Pacific* **107**, 803.

Vanden Berk, D. E., Richards, G. T., Bauer, A., Strauss, M. A., Schneider, D. P., Heckman, T. M., ... and Zheng, W. (2001), 'Composite Quasar Spectra from the Sloan Digital Sky Survey', *Astronomical Journal* **122**, 549–564.

Witt, H. J., Czerny, B. and Zycki, P. T. (1997), 'Accretion discs with accreting coronae in active galactic nuclei - II. The nuclear wind', *Monthly Notices of the Royal Astronomical Society* **286**, 848–864.

Zhang, H. and Böttcher, M. (2013), 'X-Ray and Gamma-Ray Polarization in Leptonic and Hadronic Jet Models of Blazars', *Astrophysical Journal* **774**, 18.

Zhang, H., Chen, X., Böttcher, M., Guo, F. and Li, H. (2015), 'Polarization Swings Reveal Magnetic Energy Dissipation in Blazars', *Astrophysical Journal* **804**, 58.